



**UNIVERSITÀ
DEGLI STUDI
DI TRIESTE**

UNIVERSITÀ DEGLI STUDI DI TRIESTE

XXXIV CICLO DEL DOTTORATO DI RICERCA IN

SCIENZE DELLA RIPRODUZIONE E DELLO SVILUPPO

Preclinical development of targeted-nanoparticles for the treatment of pediatric B-cell malignancies

Acute Lymphoblastic Leukemia and Burkitt Lymphoma

Settore scientifico-disciplinare: MED/04

DOTTORANDA

Sara Bozzer

COORDINATORE

Prof. Paolo Gasparini

SUPERVISORE DI TESI

Prof. Paolo Macor

TUTOR DI TESI

Prof. Alberto Tommasini

ANNO ACCADEMICO 2020/2021



**UNIVERSITÀ
DEGLI STUDI
DI TRIESTE**

UNIVERSITÀ DEGLI STUDI DI TRIESTE

XXXIV CICLO DEL DOTTORATO DI RICERCA IN

SCIENZE DELLA RIPRODUZIONE E DELLO SVILUPPO

Preclinical development of targeted-nanoparticles for the treatment of pediatric B-cell malignancies

Acute Lymphoblastic Leukemia and Burkitt Lymphoma

Settore scientifico-disciplinare: MED/04

DOTTORANDA

Sara Bozzer

COORDINATORE

Prof. Paolo Gasparini

SUPERVISORE DI TESI

Prof. Paolo Macor

TUTOR DI TESI

Prof. Alberto Tommasini

ANNO ACCADEMICO 2020/2021

To my parents

I. Riassunto

I tumori delle cellule B sono un gruppo eterogeneo di patologie per le quali le opzioni terapeutiche includono chemioterapia e immunoterapia. Nonostante il recente sviluppo di nuove strategie terapeutiche, la maggior parte dei pazienti, tuttavia, sviluppa resistenze o non risponde alle terapie.

L'obiettivo di questo progetto di dottorato è, pertanto, lo sviluppo preclinico di un nuovo strumento terapeutico per il trattamento delle neoplasie pediatriche a cellule B. In primo luogo sono state caratterizzate le nanobolle di chitosano (NBs) caricate con AntagomiR-17, sui è stato legato un anticorpo anti-CD20 (rituximab). AntagomiR-17 è in grado di legarsi e sconfiiggere il miRNA-17, che è una molecola iperespressa in diverse neoplasie delle cellule B, incluso BL, ed è associata allo sviluppo di meccanismi di resistenza ai farmaci. Rituximab è stato impiegato per indirizzare specificamente le NB alle cellule B che esprimono l'antigene CD20 *in vivo*. Le NB in chitosano risultano efficaci *in vitro* e *in vivo* nella riduzione del tumore nei topi portatori di tumore BL ma, la loro carica positiva ha dimostrato alcune limitazioni nella biodistribuzione. Inoltre, il meccanismo di targeting scelto non copre altre patologie pediatriche, come l'ALL che origina da blasti che non possiedono già l'antigene CD20 sulla loro superficie.

Per superare queste limitazioni sono state prodotte e caratterizzate nanoparticelle (NPs) PLGA-PVA. In primis, queste NP sono state confrontate con le loro controparti rivestite con HSA, aggiunta per nascondere le NP dall'IS. Una volta dimostrata l'efficacia del rivestimento *in vitro* e *in vivo* in uno zebrafish sano, è stato prodotto il meccanismo di targeting anti-CD19. L'efficacia del meccanismo di targeting è stata testata *in vitro* e, una volta impostato il modello di zebrafish portatore di tumore, anche *in vivo*. Infine, diversi farmaci sono stati testati sui linfociti B e la doxorubicina è stata scelta come candidata per riempire le NP PLGA-PVA. Le NP caricate con il farmaco sono state nuovamente testate *in vitro* e *in vivo* in un modello diffuso di ALL in zebrafish, dimostrando di ridurre significativamente la crescita del tumore e aumentando parallelamente la sopravvivenza degli animali trattati.

Tutti questi risultati insieme, evidenziano che le NP PLGA-PVA mirate con anticorpi anti-CD19 e riempite con doxorubicina rappresentano un approccio promettente per il trattamento dei tumori delle cellule B, ma anche per altre patologie. Queste nanostrutture, infatti, possono essere immaginate come una nano-piattaforma in cui i

singoli componenti, come il farmaco o il meccanismo di targeting, possono essere sostituiti per raggiungere diversi obiettivi.

II. Abstract

B-cell malignancies are a heterogeneous group of diseases, for whom treatment options include chemotherapeutics and immunotherapy. Despite the recent development of new therapeutic strategies, most patients develop resistance or do not respond to therapies.

The aim of this PhD project was the preclinical development of a new therapeutic tool for the treatment of pediatric B-cell malignancies.

Firstly, chitosan-nanobubbles (NBs) loaded with AntagomiR-17 and joined with an anti-CD20 antibody (rituximab) were characterized. AntagomiR-17 is capable of pairing and defeating miRNA-17, which is a molecule upregulated in several B-cells malignancies, including BL, and it is associated with the development of drug resistance mechanisms. Rituximab was employed to specifically target NBs to B-cells expressing the antigen CD20 *in vivo*.

Chitosan-NBs result effective *in vitro* and *in vivo* in the reduction of the tumor burden in BL-tumor-bearing mice, however, their positive charge demonstrated some limitation in the biodistribution. Moreover, the targeting mechanism chosen does not cover other pediatric pathologies, such as ALL that originates from blasts that do not already possess the CD20 antigen on their surface.

To overcome these limitations PLGA-PVA Nanoparticles (NPs) were produced and characterized. In primis, these NPs were compared to their counterparts coated with HSA, which was added to conceal NPs from the IS. Once demonstrated the efficacy of the coating *in vitro* and *in vivo* in healthy zebrafish, the targeting mechanism anti-CD19 was produced. The efficacy of the targeting mechanism was tested *in vitro* and, once the tumor-bearing zebrafish model was set, also *in vivo*.

Finally, different drugs were tested on B-cells and the doxorubicin was chosen as a candidate to fill PLGA-PVA NPs. Drug-loaded NPs were tested again *in vitro* and *in vivo* in a diffused zebrafish model of ALL, significantly reducing the tumor growth and parallelly augmenting the survival of treated animals.

All these results together, already highlighted that PLGA-PVA NPs targeted with anti-CD19 antibodies and filled with doxorubicin represent a promising approach for the treatment of B-cell malignancies, but also for other pathologies. In fact, these nanostructures can be imagined as a nano-platform in which the single components,

such as the payload or the targeting mechanism, can be replaced to achieve different goals.

III. Table of contents

| | |
|---|----|
| I. Riassunto | 1 |
| II. Abstract | 3 |
| III. Table of contents | 5 |
| IV. List of figures | 9 |
| V. List of abbreviations | 12 |
| 1. Introduction | 15 |
| 1.1 B-cell malignancies | 16 |
| 1.1.1 B-cell hematopoiesis | 17 |
| 1.1.2 Pediatric B-cell malignancies | 19 |
| 1.1.2.1 Acute Lymphoblastic Leukemia | 20 |
| 1.1.2.2 Burkitt lymphoma | 20 |
| 1.1.3 B-cell surface markers | 22 |
| 1.1.3.1 CD20 antigen | 22 |
| 1.1.3.2 CD19 antigen | 23 |
| 1.2 Nanomedicine: a revolution in progress | 25 |
| 1.2.1 Nano-carriers as delivery platforms | 27 |
| 1.2.2 Composition of nano-systems | 28 |
| 1.2.2.1 Biodegradable polymers | 32 |
| 1.2.2.1.1 Chitosan polymers | 33 |
| 1.2.2.1.2 Poly(lactide-co-glycolide) and poly(vinyl alcohol) polymers | 34 |
| 1.2.3 Biological limits to nano-devices delivery | 35 |
| 1.2.3.1 Protein corona | 37 |
| 1.2.3.2 The impact of targeting tumor cells | 40 |
| 1.2.3.2.1 Passive targeting in the tumor microenvironment | 40 |
| 1.2.3.2.2 Active targeting in the tumor microenvironment | 41 |
| 1.3 Therapeutic approaches to B-cell malignancies | 43 |
| 1.3.1 miRNA-17~92 | 44 |
| 1.3.2 Anthracyclines | 46 |
| 2. Aim of the project | 50 |
| 3. Materials and methods | 51 |
| 3.1 Cells culture and count | 54 |

| | |
|--|----|
| 3.2 Production of the targeting mechanism | 54 |
| 3.3 Production of PLGA-PVA nanoparticles | 55 |
| 3.4 Characterization of nanodevices | 55 |
| 3.4.1 Dynamic Light Scattering (DLS) | 55 |
| 3.4.2 Transmission Electron Microscopy (TEM) | 56 |
| 3.4.3 Enzyme-linked immunosorbent assay (ELISA) | 56 |
| 3.4.4 Western Blot of NPs | 56 |
| 3.4.5 SDS-PAGE and Western Blot of scFv-Fc anti-CD19 | 57 |
| 3.4.6 Red blood cells lysis | 57 |
| 3.4.7 Clotting test | 58 |
| 3.4.8 CH50 screening assay | 58 |
| 3.5 MTT viability assay | 58 |
| 3.6 Flow cytometric analysis | 59 |
| 3.6.1 Binding of anti-CD19 scFv-Fc on Bjab or Nalm-6 cells | 59 |
| 3.6.2 Binding and internalization of nano-devices in cells | 59 |
| 3.7 Immunofluorescence analysis | 59 |
| 3.7.1 Binding of anti-CD19 scFv-Fc on Bjab or Nalm-6 cells | 59 |
| 3.7.2 Binding and internalization of nano-devices in cells | 60 |
| 3.7.3 Ex vivo immunofluorescence on organs slices | 60 |
| 3.8 In vivo experiments on zebrafish embryos | 61 |
| 3.8.1 NPs biodistribution studies | 61 |
| 3.8.2 Xenograft models | 62 |
| 3.9 In vivo experiments on mice | 62 |
| 3.9.1 Evaluation of the amount of cyanine5.5 bound to NBs | 62 |
| 3.9.2 Assessment of a localized B-cell malignancy | 63 |
| 3.9.3 NBs biodistribution studies | 63 |
| 3.9.4 Evaluation of the NBs therapeutic effect | 63 |
| 4. Results and discussion | 65 |
| 4.1 Burkitt Lymphoma and chitosan nanobubbles | 65 |
| 4.1.1 Nanobubbles | 66 |
| 4.1.1.1 Types of nanobubbles | 66 |
| 4.1.1.2 Shell and structure of nanobubbles | 67 |

| | |
|--|-----|
| 4.1.2 In vitro characterization of nanobubbles | 68 |
| 4.1.2.1 Interaction of nanobubbles with blood components | 69 |
| 4.1.2.2 Binding and internalization of chitosan-NBs inside malignant B-cells | 70 |
| 4.1.2.3 In vitro effect on miRNA-17 levels | 71 |
| 4.1.3 In vivo characterization of chitosan nanobubbles | 72 |
| 4.1.3.1 Biodistribution studies | 74 |
| 4.1.3.2 Therapeutic efficacy | 76 |
| 4.2 Acute Lymphoblastic Leukemia | 79 |
| 4.2.1 Nanoparticles | 79 |
| 4.2.1.1 Types of nanoparticles | 80 |
| 4.2.2 Developing the structure of nanoparticles | 81 |
| 4.2.2.1 In vitro characterization of nanoparticles | 82 |
| 4.2.2.1.1 Shell and structure of nanoparticles | 82 |
| 4.2.2.1.2 Analysis of the Protein Corona on the NPs' surface | 83 |
| 4.2.2.1.3 Interaction of nanoparticles with blood components | 87 |
| 4.2.2.1.4 Binding and internalization of NPs inside malignant B-cells | 88 |
| 4.2.2.2 In vivo studies | 91 |
| 4.2.2.2.1 Biodistribution studies in healthy zebrafish larvae | 91 |
| 4.2.3 Targeting mechanism: the specific delivery of nanoparticles | 95 |
| 4.2.3.1 Production and characterization of the targeting mechanism | 95 |
| 4.2.3.2 Targeted nano-devices: in vitro characterization | 97 |
| 4.2.3.2.1 Analysis of the Protein Corona on the NPs' surface | 98 |
| 4.2.3.2.2 Interaction of nanoparticles with blood components | 101 |
| 4.2.3.2.3 Binding and internalization of NPs inside malignant B-cells | 102 |
| 4.2.3.2.4 Evaluation of NPs toxicity | 106 |
| 4.2.3.3 In vivo studies | 107 |
| 4.2.3.3.1 Elimination studies in healthy zebrafish larvae | 107 |
| 4.2.3.3.2 Creation of the tumor-bearing zebrafish model | 107 |
| 4.2.3.3.3 Biodistribution studies in tumor-bearing zebrafish larvae | 109 |
| 4.2.4 Developing the nanoparticles' core | 111 |
| 4.2.4.1 In vitro evaluation of the most effective drug-NP couple | 111 |
| 4.2.4.2 Evaluation of the therapeutic effect of loaded-NPs | 113 |

| | |
|--------------------------------------|-----|
| 4.2.4.2.1 Xenograft zebrafish models | 114 |
| 4.2.4.2.2 In vivo NPs efficacy | 116 |
| 5. Conclusions | 118 |
| 6. Bibliography | 124 |

IV. List of figures

- Figure 1.1 Estimated total incident cancer cases in 2015 by the top 15 specified diagnoses and regions.
- Figure 1.2 Simplified schematic representation of B-cell differentiation.
- Figure 1.3 Expression of CD19 and CD20 in B-cell lineage.
- Figure 1.4 Nano-devices in imaging and therapies.
- Figure 1.5 Schematic representation of nano-carriers for cancer therapy.
- Figure 1.6 Biodegradable polymers.
- Figure 1.7 Opsonization process.
- Figure 1.8 The duality of the protein corona.
- Figure 1.9 Passive targeting.
- Figure 1.10 Active targeting.
- Figure 1.11 The pleiotropic functions of miRNA-17~92 achieved by repressing specific targets.
- Figure 1.12 Chemical structures of clinically approved anthracyclines.
- Figure 3.1 Capillary glasses.
- Figure 4.1 miRNA-17 expression in different cell lines.
- Figure 4.2 Nanobubbles (NBs) used for *in vitro* and *in vivo* studies.
- Figure 4.3 Nanobubbles characterization.
- Figure 4.4 *In vitro* test of clotting formation and activation of classical pathway of the Complement.
- Figure 4.5 NBs bind and internalize in tumor B cells.
- Figure 4.6 AntagomiR-17-loaded NBs reduce miRNA-17 levels in tumor B cells.
- Figure 4.7 Analysis of NBs biodistribution in mice.
- Figure 4.8 Targeted and untargeted NBs localized in the tumor mass.
- Figure 4.9 Local treatment with NB3 reduce miRNA-17 levels in tumor B-cells and inhibit tumor growth.
- Figure 4.10 Anti-CD20 NB3 treatment decrease tumor mass neutralizing miRNA-17 activity.
- Figure 4.11 Anti-CD20 NB3 treatment in a low miRNA-17 expressing model.
- Figure 4.12 Nanoparticles (NPs) used for *in vitro* and *in vivo* studies.
- Figure 4.13 Nanoparticles characterization.

- Figure 4.14 Coating with Human Serum Albumin.
- Figure 4.15 Data analysis from mass spectrometry.
- Figure 4.16 Differentially adsorbed opsonins and dysopsonins on NPs' surface.
- Figure 4.17 *In vitro* test of clotting formation and activation of classical pathway of the Complement.
- Figure 4.18 Binding/internalization of NPs in malignant B cells.
- Figure 4.19 Binding/internalization of NPs in macrophages.
- Figure 4.20 Binding/internalization of NPs in macrophages isolated from donor's blood.
- Figure 4.21 Zebrafish as animal model for *in vivo* studies.
- Figure 4.22 Different accumulation of NPs in the tail of zebrafish.
- Figure 4.23 Timeline of macrophages' development in the transgenic line Tg(mpeg1:mCherry).
- Figure 4.24 Co-localization between macrophages and NPs.
- Figure 4.25 Design and production of the targeting mechanism.
- Figure 4.26 Binding of the targeting molecule to CD19-expressing cells.
- Figure 4.27 Characterization of targeted-NPs.
- Figure 4.28 Data analysis from mass spectrometry.
- Figure 4.29 Differentially adsorbed opsonins and dysopsonins on NPs' surface.
- Figure 4.30 *In vitro* test of clotting formation and activation of classical pathway of the Complement.
- Figure 4.31 Binding/internalization of NPs in malignant B cells.
- Figure 4.32 Localization of NP inside cells.
- Figure 4.33 Binding/internalization of NPs in macrophages.
- Figure 4.34 Localization of NP inside cells.
- Figure 4.35 Binding/internalization of NPs in macrophages isolated from donor's blood.
- Figure 4.36 Toxicity evaluation of NP on malignant B-cells.
- Figure 4.37 Co-localization between macrophages and NPs.
- Figure 4.38 Setting up of the animal model.
- Figure 4.39 Experimental timeline.
- Figure 4.40 Co-localization analysis.
- Figure 4.41 Biodistribution studies in tumor-bearing zebrafish.
- Figure 4.42 Viability assay after incubation with free drugs.

- Figure 4.43 Viability assays after incubation with loaded-NPs.
- Figure 4.44 Characterization of targeted-NPs.
- Figure 4.45 Viability assays after incubation with loaded-NPs.
- Figure 4.46 Localized xenograft zebrafish model.
- Figure 4.47 Setting up of a localized model of B-cell malignancies.
- Figure 4.48 Setting up of a diffused model of B-cell malignancies.
- Figure 4.49 Therapeutic effect of NP5 in a diffused model of B-cell malignancy.

V. List of abbreviations

| | |
|-------|--|
| ADC | Antibody Drug Conjugate |
| ADCC | Antibody Dependent Cellular Cytotoxicity |
| ADCP | Antibody Dependent Cellular Phagocytosis |
| AID | Activation-Induced cytidine Deaminase |
| ALL | Acute Lymphoblastic Leukemia |
| APC | Antigen-Presenting Cells |
| APS | Ammonium Persulfate |
| BCIP | 5-Bromo-4-Chloro-3-Indolyl-phosphate |
| BCR | B-Cell Receptor |
| BL | Burkitt Lymphoma |
| BM | Bone Marrow |
| BSA | Bovine Serum Albumin |
| C | Constant domain |
| CAR | Chimeric Antigen Receptor |
| CD | Cluster of Differentiation |
| CDC | Complement Dependent Cytotoxicity |
| CHO | Chines Hamster Ovary |
| CNS | Central Nervous System |
| CS | Complement System |
| CTRL | Control |
| D | Diversity |
| DLBCL | Diffuse Large B-Cell Lymphoma |
| DLS | Dynamic Light Scattering |
| EBV | Epstein-Barr Virus |
| EC | European Commission |
| EDTA | Ethylene Diamine Tetra acetic Acid |
| ELISA | Enzyme-Linked Immunosorbent Assay |
| EMA | European Medicines Agency |
| EPR | Enhanced Permeability Retention |

| | |
|----------|---|
| ESF | European Science Foundation |
| Fab | Antigen binding fragment |
| FBS | Fetal Bovine Serum |
| Fc | Fragment crystallisable |
| FDA | Food and Drug Administration |
| FITC | Fluorescein Isothiocyanate |
| H | Heavy chain |
| HL | Hodgking Lymphoma |
| HIV | Human Immunodeficiency Viruses |
| HRP | Horseradish Peroxidase |
| HSA | Human Serum Albumin |
| i.p | intra peritoneal |
| i.v | intra venous |
| ICIs | Immune Checkpoint Inihbitors |
| Ig | Immunoglobulin |
| IS | IS |
| J | Joining |
| JAK-STAT | Janus kinase/signal transducer and activator of transcription |
| Koff | Kinetics konstant association |
| Kon | Kinetics konstant association |
| L | Light chain |
| mAb | monoclonal Antibody |
| miRNAs | microRNA |
| MPS | Mononuclear Phagocyte System |
| MRI | Magnetic Resonance Imaging |
| MTT | 1-(4,5-Dimethylthiazol-2-yl)-3,5-diphenylformazan |
| MW | Molecular Weight |
| NBs | Nanobubbles |
| NBT | Nitro Blue Tetrazolium |
| NHL | Non-Hodgking Lymphoma |
| NPs | Nanoparticles |

| | |
|----------|--|
| OD | Optical Density |
| OS | Overall Survival |
| PBS | Phosphate Buffered Saline |
| PC | Protein Corona |
| PDI | Polydispersity Index |
| PET | Positron Emission Tomography |
| PFA | Paraformaldehyde |
| PGA | Polyglycolic acid |
| PLA | Poly(lactic-acid) |
| PLC | Poly(ϵ -caprolactone) |
| PLGA | Poly(lactide-co-glycolide) copolymers |
| PMMA | Poly(methyl methacrylate) |
| PPAR | Peroxisome Proliferator-Activated Receptor |
| PVA | Poly Vinyl Alcohol |
| RES | Reticuloendothelial System |
| ROS | Reactive Oxygen Species |
| scFv | single chain Fragment variable |
| SDS-PAGE | Sodium Dodecyl Sulphate - PolyAcrylamide Gel Electrophoresis |
| SEM | Scanning Electron Microscope |
| SWCNT | Single-Walled Carbon Nanotube |
| TEM | Transmission Electron Microscopy |
| TEMED | N,N,N',N'tetrametiletilendiamina |
| TMB | 3,3',5,5'-Tetramethylbenzidine |
| TRITC | Tetramethylrhodamine |
| V | Variable domain |
| WHO | World health Organization |

1. Introduction

The major public health problem worldwide is represented by cancer and it is still the second leading cause of death in the United States, even if in 2020 the diagnosis and treatment of cancer were hampered by the coronavirus disease 2019 (COVID-19) pandemic [1]. Childhood and juvenile cancer, which affects individuals between 0 and 19 years old, consists of a set of diseases that have their characteristics concerning to histological type and clinical behavior of the disease. According to the WHO, “Cancer is a leading cause of death for children and adolescents” (World Health Organization 2021). In particular, in the States, cancer is the second most common cause of death among children, surpassed only by accidents [1]. Moreover, in most populations, childhood, and juvenile cancer accounts for 1% to 4% of all malignant tumors, hence in developing countries, where the child population reaches 50%, this proportion of childhood cancer accounts for 3% to 10% of all cancers [2]. Among them, leukemia is the most common childhood cancer, accounting for 28% of cases, followed by brain and other nervous system tumors (27%), more than one-quarter of which are benign/borderline malignant [1]. Globally, Acute Lymphoblastic Leukemia (ALL) is the most common childhood cancer and is estimated to account for 19% of total childhood cancer incidence, followed by non-Hodgkin lymphoma (NHL, 5%), nephroblastoma (5%), Burkitt Lymphoma (BL, 5%), and retinoblastoma (5%) (Figure 1.1). Moreover, summing productive years lost due to the mortality or disability per pathology, over a third of them are caused by leukemia [3]. As predictable, the most common cancer differs by region; for example, the incidence of ALL is significantly lower in sub-Saharan Africa than in other regions in contrast to statistics of BL which are inverted, if compared. Because it is generally not possible to prevent malignancies in children, the most effective strategy to reduce the burden of cancer in this part of the population and improve outcomes is to focus on a prompt, correct diagnosis followed by effective, evidence-based therapy with tailored supportive care [4].

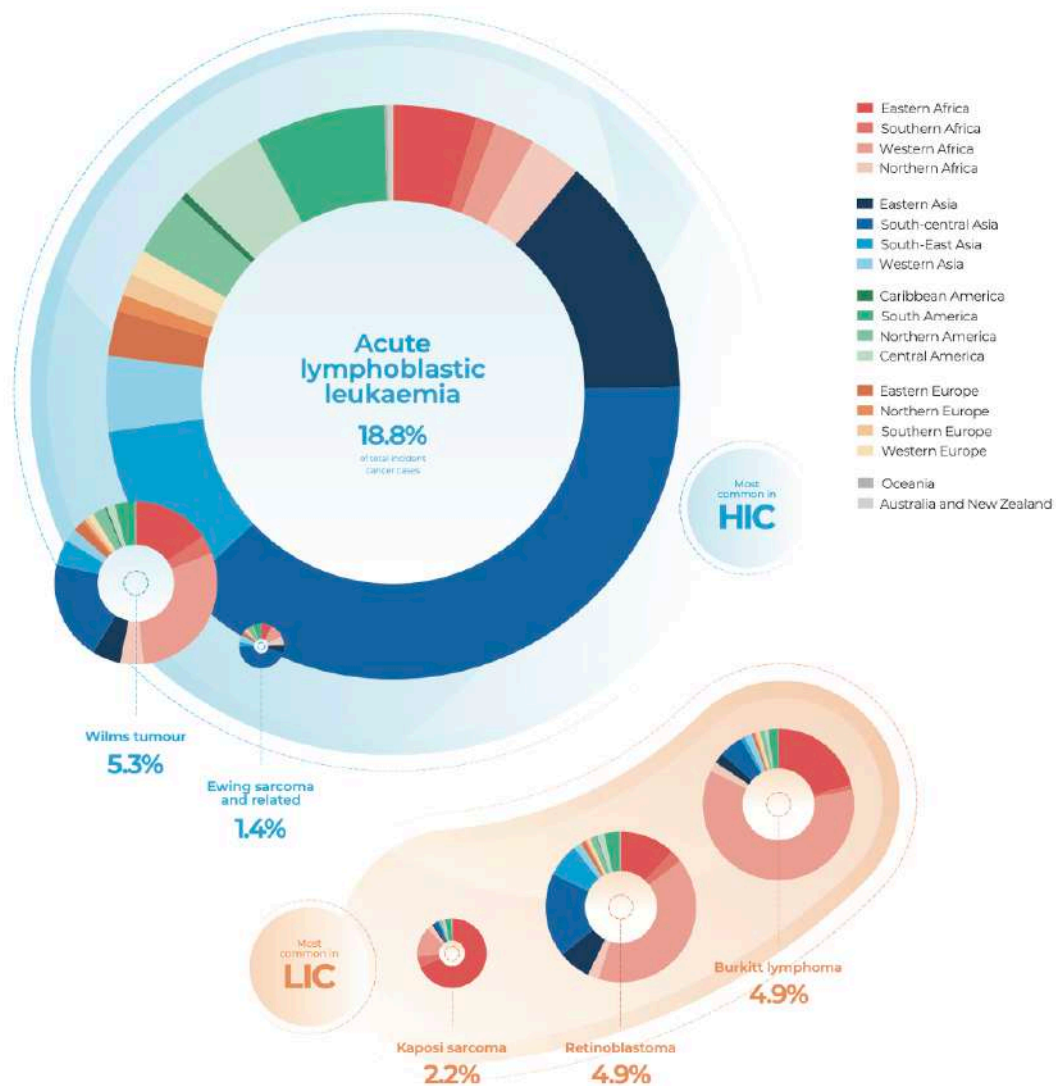


Figure 1.1: Estimated total incident cancer cases in 2015 by the top 15 specified diagnoses and regions. HIC: High-Income Countries; LIC: Low-Income Countries (World Health Organization, 2021).

1.1 B-cell malignancies

B-cells are a subtype of white blood cells (lymphocytes) that are part of the Immune System (IS) and play an important role in fighting infection in the body. Usually, the body makes new lymphocytes only when they are needed to replace old cells that have died. In B-cell malignancies, these cells are malfunctioning and become malignant. This means they grow when the body doesn't need them and reproduce at an abnormal rate. Since B-cell malignancies develop from different stages of development these constitute a heterogeneous group of pathologies [5].

1.1.1 B-cell hematopoiesis

B-cells, also known as B lymphocytes, are part of the humoral arm of the adaptive IS aiming to eliminate bacteria, prevent viral infections, neutralize bacterial toxins, and play an important role in certain allergic reactions. In a simple definition, they are reported as a population of cells that express clonally diverse cell surface immunoglobulin (Ig) receptors, able to recognize specific antigenic epitopes. Their origin can be traced to the evolution of adaptive immunity in jawed vertebrates beginning more than 500 million years ago [6]. The discovery and characterization of B-cells occurred in the second half of the last century when Max Cooper demonstrated that antibody production was completely abrogated in irradiated chickens after surgical removal of the “Bursa of Fabricius”, the primary site of B-cell development in birds. The notation “B”-cells originates nothing other than from this organ. Several distinct B-cell subsets have been defined that possess discrete functions in both adaptive and innate humoral immune responses [7]. B lymphocytes arise from multipotent hematopoietic stem cells that successively populate the embryonic paraaortic splanchnopleure, the fetal liver, and after birth are located in the bone marrow (BM) [8, 9]. Their development is typically viewed as a linear, stepwise process, defined by the regulated expression of specific sets of transcription factors, Ig, and cell-surface molecules, that takes 2-3 days in humans. The development begins in the BM as pluripotent stem cells and encompasses subsequent maturation stages ending in the spleen and giving rise to pro-B-cells, pre-B-cells, immature B-cells, and finally mature B-cells (Figure 1.2) [9, 10]. Phenotypically, these

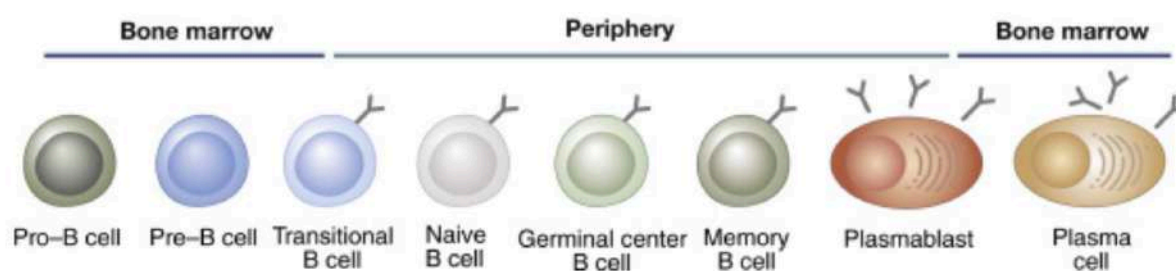


Figure 1.2: Simplified schematic representation of B-cell differentiation. In the bone marrow, cells develop through the interaction with specific antigens that induce their activation, proliferation, and differentiation. Pluripotent stem cells mature into pro-B-cells, followed by pre-B-cells, then, in the periphery, transitional B-cells differentiate in naïve B-cells and then in germinal center B-cells. In the end, they become plasmablast and plasma cells (Crickx et al 2019, modified).

development stages are characterized by the expression of surface antigens, called

clusters of differentiation (CD), such as CD10, CD19, CD20, CD21, CD24, CD34, and CD38. Consequently, this description has facilitated the definition of both early and late stages of development, especially in those cases where Ig cannot be used to distinguish between cell types [9, 11]. However, B-cell development is a more complex process than the simple, linear pathways hereby described.

Lymphocyte development requires the cooperative action of a network of cytokines and transcription factors that positively and negatively regulate gene expression in a hierarchical way [8]. The maturation process is defined by the successive rearrangements of the Ig in a nearly random fashion rearranges of variable (V), joining (J), and for heavy chains, diversity (D) gene segments, via an error-prone process. In this way, a B-cell repertoire can be generated, expressing antibodies able to recognize and bind more than 5×10^{13} different antigens [8, 9, 12]. The maturation of a pro-B-cell to a pre-B-cell occurs with the expression of the pre-B-Cell Receptor (BCR) and signal-transducing components. The expression of a complete pre-BCR leads to the massive proliferation of pre-B-cells; this process occurs independently of the ligand and carries out an important control point in the maturation itself. This proliferation is fundamental to increasing the number of cells that have successfully recombined heavy chain genes. The proper rearrangement of the pre-BCR inhibits the recombination of other heavy chain *loci* by a feedback loop inducing the recombination of the light chain genes to continue the differentiation of B-cells. Immature B lymphocytes do not proliferate but are subjected to selection based on their affinity towards antigens: if they are self-reactive, they die, if they are weakly self-reactive, they leave the BM and go to secondary lymphoid tissues such as the spleen and lymph nodes where they complete their maturation into the marginal zone or follicular B-cells. Marginal zone B-cells are in the region of the spleen positioned at the interface between the circulation and the IS providing the efficient immune surveillance of the circulatory system. Marginal zone B-cells express a poly-reactive BCR able to bind multiple microbial molecular patterns and constitute the first line of defense against pathogens. In fact, after antigenic presentation mediated by antigen-presenting cells (APC), marginal zone B-cells initiate the immune response rapidly developing, thanks to extra-follicular plasma cells and secreting low-affinity IgM (short-lived plasma cells). On the other hand, stimulated follicular B-cells produced high-affinity mono-reactive antibodies after the interaction with T lymphocytes presenting the antigen. This process also triggers proliferation and differentiation of B-

cells which mutate their antibody genes through somatic hypermutation and switch the class of their antibody (from IgM to IgG, IgA, or IgE) in sites known as germinal centers [13]. A germinal center is divided into two compartments termed the dark and the light zone. The dark zone is localized proximal to T-cell areas and contains proliferating B-cells that undergo isotype switching and, after several rounds of cellular division, acquire high rates of mutation in their Ig variable region genes increasing BCR affinity and specificity [13, 14]. B-cell clones expressing variants with higher binding to the antigen are selectively expanded whereas changes that result in impaired antigen-binding induce cell death. Once these B-cells have stopped proliferating, they migrate to the light zone where they are subjected to selection by lymphocytes T [8, 15, 16]. Therefore, while B-cells rearrange their DNA to produce high-affinity antibodies, they are potentially susceptible to dangerous processes. In fact, many of the oncogenic events that occur in lymphoma and leukemia disrupt the molecular pathways that regulate B-cell differentiation, proliferation, and apoptosis. Molecular alterations (e.g., double-stranded DNA breaks, chromosomal translocation, and inappropriate gene expression) are the basis of aberrant BCR signaling enabling the uncontrolled growth and development of B-cell malignancies. Interesting is that malignant B-cells are trapped at a particular evolution stage reflecting the level at which the alteration occurred, blocking cell development. The result is a progressive expansion of the altered cells, which due to signaling variations, will proliferate faster and invade different body sites [13, 17]. For all the above-mentioned reasons, “*normal lymphocyte differentiation is, in some sense, a disaster waiting to happen*” [17, 18]. Fortunately, based on the maturation lock point and the cell type involved, different subtypes of B-cell malignancies are identifiable at the clinical level, seeing as B-cell development can be monitored by examining the pattern of expression of characteristic surface proteins [9].

1.1.2 Pediatric B-cell malignancies

A cancer diagnosis is upsetting at any age, but especially so when the patient is a child. The treatment of pediatric cancers has been a success story, with current overall survival (OS) of ~80% in the United States. Nonetheless, this success has occurred at a significant price, as the prevalence of severe chronic disorders among long-term pediatric survivors of cancer is 3-fold higher than in matched controls. In addition, there are several tumors for which long-term survival remains poor [19].

There are still close to 17,000 children and adolescents aged 19 years or younger who have been diagnosed with cancer in the United States in 2020, and close to 2,000 will die of the disease. In those aged 14 or younger, NHL accounts for 5% of cancers, whereas in adolescents aged 15 to 19 years, NHL accounts for 7% and the most common NHL types include BL and diffuse large B-cell lymphoma (DLBCL) [20].

1.1.2.1 Acute Lymphoblastic Leukemia

ALL is the most common childhood malignancy, arising from the clonal expansion of transformed B-cell precursors [2, 21, 22]. ALL accounts for almost a quarter of all cancers in patients under the age of 20 and while most cases happen in younger people, adult ALL patients are more challenging to treat and show worse prognosis. ALL develop from the unregulated growth of clonal lymphoid cells, most commonly pre-B-cells (80%-85%) and less commonly T (10%-15%) and mature B-cells (< 5%) [12, 21, 22]. Early-onset B-ALL can be divided into infant-ALL presenting at age <12 months or childhood-ALL presenting at age >12 months. Interestingly, recent studies demonstrated that significantly all infant leukemia and much of childhood-ALL originate before birth [12]. Clinical presentation can be nonspecific and span a spectrum of symptoms and signs. Most patients present with fever, pallor, and bruising as early signs of bone marrow suppression or hematologic abnormalities, whereas over 60% can demonstrate splenomegaly or hepatomegaly. Moreover, a significant number of patients showed recurrent infections, fatigue, lymphadenopathy, and skin rashes. Fortunately, the 5-year survival rate has increased from under 50% in the second half of 1900 to nearly 85% in the 21st century [21].

1.1.2.2 Burkitt lymphoma

BL is a rare, aggressive NHL that accounts for 1-2% of all cases of NHL in the general population. In the 1980s, Guy de Thé described BL as “the Rosetta stone of cancer” [23]. In fact, BL has had an important role in the understanding of tumorigenesis being reported as the first human tumor associated with a virus, one of the first tumors presenting a chromosomal translocation able to activate an oncogene, and the first lymphoma associated with HIV infection. In fact, the three main types of BL are endemic, sporadic, and immunodeficiency-related (eg, associated with HIV) [24]. BL is characterized by the constitutive overexpression of *c-myc* in germinal center B-cells that causes a rapid cell division with a cell doubling time of 24-48h [25, 26]. In

particular, endemic BL is the most common in children (4-7 years) in poor countries [25]. It is closely associated with the Epstein-Barr virus (EBV), which acts as an oncogenic driver of BL. Malaria, which is a very common disease in poor countries, has been associated with EBV, causing its persistence. Moreover, malaria increases the risk of developing BL by increasing the number of infected B-cells through viral reactivation and reseeding of the latent pool, causing loss of immune control of those infected B-cells. Moreover, malaria induces *c-myc* translocation through a mechanism mediated by activation-induced cytidine deaminase (AID) [25] which was demonstrated to lead to tumorigenesis when is out of control because AID creates mutations in DNA by deamination of cytosine base, which turns it into uracil. During germinal center development of B lymphocytes, AID also generates other types of mutations that produce antibody diversity, but also lead to B cell malignancies. The main sites of appearance of this subgroup of tumors are the jaw, viscera, intestine, breast, and ovaries [26, 27]. Prepubertal and pubertal children tumors appear in the gonads and in teenagers with long bones [25, 27]. Differently, sporadic BL is more common in 30-40 years old male adults in rich countries. It is characterized by bulky abdominal masses (60-80%), with abdominal pain and distension, nausea, vomiting, and gastrointestinal bleeding [25]; localized lymphadenopathy, extranodal disease, and in rare cases involvement of the central nervous system (CNS) (40%) and BM (70%), skin, testes, breasts, and thyroid gland [25, 26]. The next most common sites are the head and neck. The development is very fast, with symptoms such as weight loss, night sweats, and unexplained fever [25]. The third subtype of BL is immunodeficiency-associated BL. The HIV virus affects B-cells by dysregulating AICD and causing chronic B-cell activation [25]. This kind of BL is clinically aggressive because it is associated with combined antiretroviral therapy. There is BM involvement and male predominance [26]. The therapy for BL consists of multi-agent combination cytotoxic chemotherapy with aggressive tumor lysis management, however, the prophylaxis and the anticipation of infectious and disease-related complications remain fundamental [26].

ALL and BL therapeutic options suffer from the limitations of the conventional chemotherapeutic approach. In fact, the chemotherapy intensity has been raised to the limit of tolerance, therefore there is a need for novel therapeutic approaches able to further improvement in outcomes and reduction of adverse effects [28].

1.1.3 B-cell surface markers

Each B-cell malignancy is associated with a specific developmental stage and surface antigens expression. Surface molecules have particular importance to identify the degree of maturation for diagnosis, prognosis, and best treatment options; besides, they can be used as targets for specific clinical interventions [29, 30]. Ideal tumor antigens should be abundant, accessible, and express homogeneously, consistently, and exclusively on the surface of target cells; moreover, antigen secretion should be minimal. All these features guarantee the working of immunotherapy because of the antibody's specificity and the minimal side effects. In fact, immunotherapy is a type of cancer treatment that helps host IS fight cancer, thanks to the fact that the modified immunotherapy antibodies bind to the tumor antigens marking and identifying the cancer cells for the IS to inhibit or kill [31].

For what concerns B-cell malignancies, surface antigens such as CD19, CD20, CD22, CD30, CD38, and CD52 are currently the main targets for immunotherapy. In detail, CD19 and CD20 are markers specific for cancer B-cells while CD30, CD38, and CD52 are generally expressed on the surface of mature B and T lymphocytes but also on malignant lymphocytes. For instance, CD22 is a regulatory component of the BCR complex, expressed exclusively in pre-B and mature B-cells. Since CD22 endocytosis can be triggered efficiently, antibodies and antibody-based immunotoxins against CD22 have been developed to treat B-cell lymphomas and leukemias [32]. Other under-investigation tumor-associated antigens are represented by the CD30 and CD52. The first one is a specific marker of Hodgkin Lymphoma (HL) and anaplastic large cell lymphoma, but its expression is also detectable in B-cell lymphomas, including DLBCL and primary mediastinal large B-cell lymphoma [32]. On the other hand, the presence of CD52 has been demonstrated in many cells, such as B and T lymphocytes, where it is strongly expressed, and monocytes and macrophages, which include the lower levels of CD52. Moreover, a high expression of CD52 was demonstrated on most malignant lymphoid cells [33]. Nevertheless, historically, the attention was focused on other most promising antigens.

1.1.3.1 CD20 antigen

Among B-cells-related antigens, CD20 was the first molecule against whom monoclonal antibodies (mAb) were developed [34-37]. The human CD20 gene is encoded by eight exons located on chromosome 11, and the mouse gene is found in

an evolutionarily conserved region of chromosome 19 (showing 73% homology). The pattern of expression of CD20 (Figure 1.3), present on mature B-cells through plasma blasts but not on early stem cells or on plasma cells, is fundamental for the B-cell ablative therapy [38].

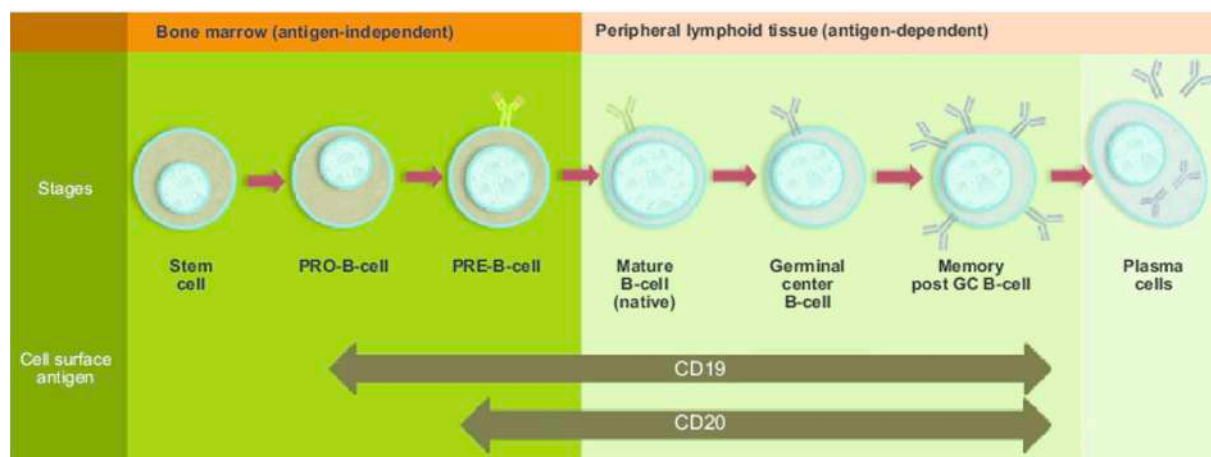


Figure 1.3: Expression of CD19 and CD20 in B-cell lineage. Illustrative representation of B-cell differentiation and maturation. CD19 antigen is expressed from pro-B-cells to plasma cells, hence CD20 from pre-B-cells to plasma cells (Raufi et al, 2013, modified).

This type of therapy allows to eliminate of all cancer cells and, at the same time, saves early stem cells. In this way, it is possible to restore the B-cells population after the treatment. Therefore, the first mAb to receive approval by the Food and Drug Administration (FDA) for use in cancer treatment was rituximab (Rituxan®) an anti-CD20 chimeric mAb. Since its approval for relapsed/refractory NHL in 1997, rituximab has been licensed for use in the treatment of numerous other B-cell malignancies, as well as autoimmune conditions, including rheumatoid arthritis [38]. Therefore, for nearly 20 years, rituximab-based therapies demonstrate their dominance in this field; but on the other hand, if a patient experiences relapsed or refractory disease after rituximab-based treatment, there are limited options for a complete rescue [32]. For this reason, other antigens are under investigation, and nevertheless, the focus of immunotherapy development for over 30 years was set on CD19.

1.1.3.2 CD19 antigen

CD19 is a 95-kDa member of the Ig superfamily and is expressed nearly exclusively on B lymphocytes, together with other cell surface regulatory molecules. CD19 is expressed by almost all B-cell developmental stages, and it is a critical co-receptor for B-cell signaling, which acts in signaling, cell activity, and proliferation [39]. In

particular, CD19 is a cell-surface glycoprotein, and it exists in a complex with CD21 and CD81. With the help of CD21, CD19 can bind the complement C3 cleavage product C3d enabling CD19 and the BCR to interact and thereby providing a link between innate and adaptive immunity. These interactions permit the reduction of the number of antigen receptors that need to be stimulated to activate the cell, reducing the threshold required for B-cell proliferation in response to a given antigen [40]. Given the above-mentioned important roles of CD19 in BCR signaling, and its overall expression pattern from pro-B-cells until the terminal differentiation to plasma cells (Figure1.3), it is not surprising that abnormal CD19 expression on B-cells is associated with autoimmune diseases and B-cell malignancies development [39, 41]. For these reasons, CD19 represents a more exploitable antigen than CD20.

Pharmaceutical companies are actively pursuing anti-CD19 strategies as they have the promise of directly targeting early B-cell differentiation stages not currently targeted by anti-CD20 therapies (i.e., ALL) or B-cell malignancies resistant to anti-CD20 approaches. Although CD19 has been a focus of immunotherapy development for many years, it is only recently that durable therapeutic responses have been achieved with CD19-directed approaches, even if with some limitations. Anti-CD19 therapies currently in clinical trials include mAb, antibody-targeted cytotoxic drug conjugates (ADC), bispecific antibodies, and chimeric antigen receptor (CAR) T-cells [41, 42]. For instance, given the substantial improvement in OS by the mAb anti-CD20 rituximab in ALL-patients with significant CD20 expression ($\geq 20\%$), the implementation of CD19 mAb, potentially reaching a broader spectrum of patients, is a reasonable strategy [40]. Although therapeutic antibodies ensure the specific effect and improve survival, compared to chemotherapy alone, an assessment of the disadvantages is however necessary, due to the frequency of incomplete response and resistance phenomena [43].

For all these reasons, over the years, research focuses on the identification of “next-generation” approaches benefiting from both chemotherapy regimens and immunotherapy. Results in this research field provide a rationale for investigating further targeting antigens in the treatment of B-cell disorders, remembering that the ideal one would be a broad-spectrum antigen in order to expand the target pathologies.

Since the purpose is to guarantee the therapeutic effect given by the chemotherapeutic payload and simultaneously avoid side effects “next-generation” approaches can be represented by nanodevice equipped with an active targeting mechanism. In agreement with this, recent studies on this kind of nanomedicine proved to be useful to affect only neoplastic cells, preserving the viability of the healthy ones [44].

1.2 Nanomedicine: a revolution in progress

The eradication of diseases remains an elusive clinical goal, largely due to the heterogeneous and idiosyncratic nature of individual cancers, and the inability to target therapeutics to neoplastic areas without damaging normal tissues. Therefore, the ideal drug is easy to administer, binds univocally to its specific target with high specificity and affinity, does not modulate off-target functions, and persists in the body only the time necessary to have a therapeutic effect. The complex nature of cancer presents multiple challenges to its therapeutic treatment. Although the administration of free chemotherapeutic drugs remains the gold standard for cancer treatment, this therapeutic strategy still presents inherent challenges. Among them, the most important is the lack of specificity and poor drug accumulation in the tumors. Hence, undesired side effects in healthy tissues occur, especially in the heart, BM, gastrointestinal tract, and nervous system [45, 46].

Over the last years, nanomedicine has become an inescapable part of modern everyday life and most of the limits of traditional drugs are bypassed by nanomedicine, which uniquely focuses on medically related, patient-centric nanotechnologies [47] (Figure 1.4).

Indeed, the European Science Foundation (ESF) has defined nanomedicine as a tool that uses a nano-sized device for the diagnosis, prevention, and treatment of diseases. So, the focus of nanomedicine is to improve the quality of life of patients, encompassing the three main nanotechnology areas, which are developed for healthcare applications, such as diagnostics, imaging agents, and drug delivery through innovative technologies and biomaterials. In this sense, the European Commission (EC) published the “Recommendation on the definition of nano-materials” that defines whether a material can be considered a nano-material or not in terms of legislation and policy in the European Union [48]. According to the EC recommendation: *“Nano-material” means a natural, incidental, or manufactured*

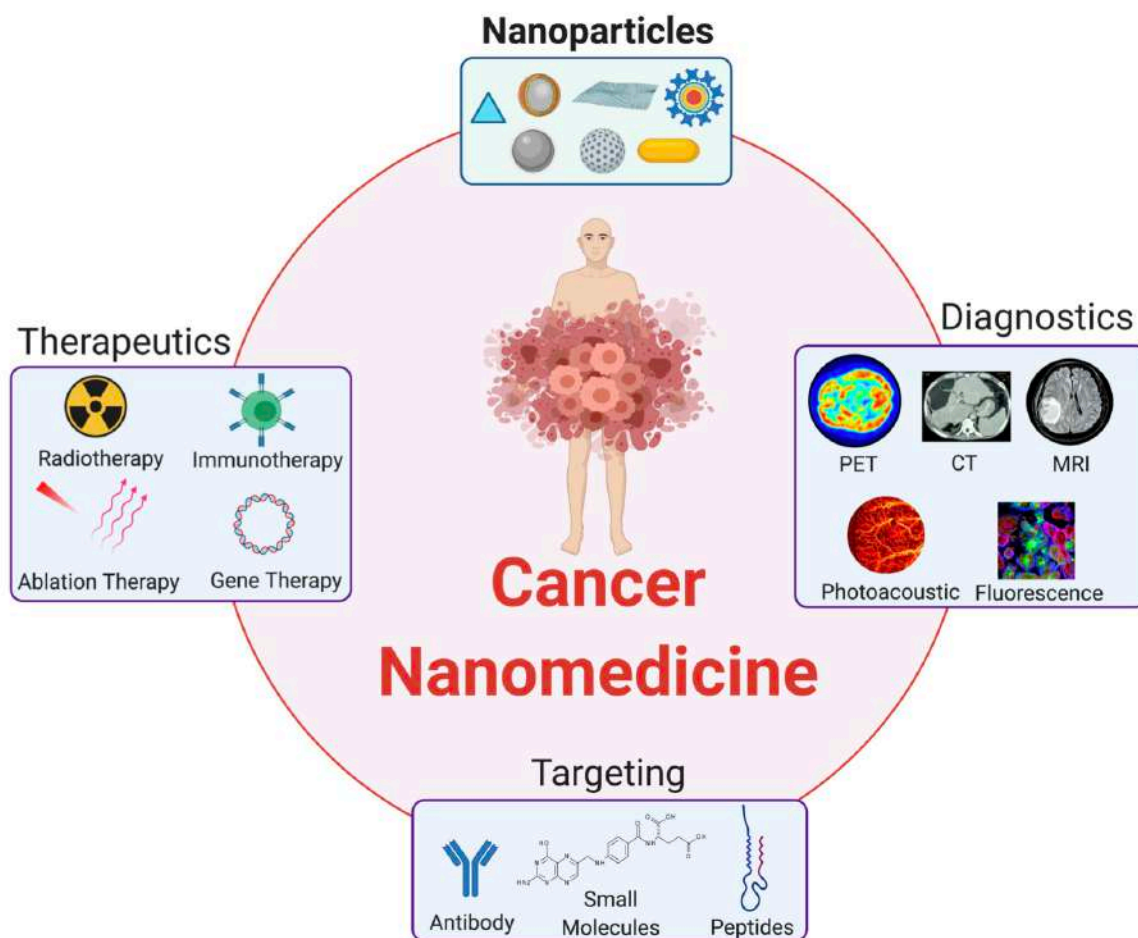


Figure 1.4: Nano-devices in imaging and therapies. The compatibility between nanoparticle size and the biological systems, coupled with the ability to tailor their physicochemical properties enhances a personalized approach to disease management and therapies could considerably improve the diagnostics and therapeutics of various cancers (Damasco et al, 2020).

material containing particles, in an unbound state or as an aggregate or as an agglomerate and where, for 50% or more of the particles in the number size distribution, one or more external dimensions is in the size range 1 nm–100 nm. However, nanoparticles (NPs) for medical applications are defined as particles with a size between 1 and 1000 nm [49-51], and they can be engineered to have different sizes, shapes, chemical compositions, surface chemical characteristics, and hollow or solid structures leading them suitable for the treatment of several diseases [52]. Moreover, nano-materials, in contrast to atoms and macroscopic materials, have a high ratio of surface area to volume as well as tunable optical, electronic, magnetic, and biological properties indeed, all these features allow the development of personalized and safe drugs. Conceivably, considerable technological success has been achieved in this field, but the main obstacles to the application of nanomedicine

becoming a new paradigm in cancer therapy derive from the complexities and heterogeneity of tumor biology and an incomplete understanding of nano-bio-interactions [53]. With the progression of nano-devices, the idea is to include the optimal dose of a drug in a nano-system that actively reaches its target and here releases its content, improving efficacy. At the same time, the specificity for tumor cells prevents the interactions of NPs with healthy tissues, thus reducing side effects. In addition, these systems are able to protect themselves from degradation *in vivo*, prolonging their circulation time [45]. Thus, the choice of an appropriate nano-carrier is based on the more suitable application.

1.2.1 Nano-carriers as delivery platforms

Delivering drugs loaded inside NPs to cancer cells is an extremely complicated process. Perhaps the right attitude could be to embrace the benefits of nanotechnologies but acknowledge their limitations [45]. Indeed, it is necessary that NPs evade immune surveillance by avoiding adsorption of serum opsonin proteins, and selectively extravasate at the tumor site [54-56]. Among the essential NPs' features to achieve homogeneous distribution throughout a tumor, there is the ability to overcome thick tumor stroma, uptake by macrophages, high interstitial fluid pressure, and slow diffusion [57]. Luckily, in the research landscape, there are plenty of different nano delivery systems which increase the possibility of better investigating cancer and choosing the more suitable vector for therapy. A vast choice of materials, differing from natural to synthetic and to hybrid polymers, has been developed in the form of delivery vesicles for anti-cancer treatment. Various biomaterials were investigated for constructing therapeutic delivery carriers through the customization of their chemical and physical properties to meet specific needs in different clinical applications. In fact, nano-carriers, owing to their high surface-area-to-volume ratio, make it possible to achieve high ligand density on the surface for targeting purposes [58]. Furthermore, changing the basic properties of NPs, e.g., diameter, shape, and surface charge, are useful to modulate immunotherapy. For instance, the NPs with a diameter of over 500 nm can target macrophages and are internalized via phagocytosis; moreover, the smaller NPs (<50 nm) have an enhanced ability to elicit the immune activities over larger NPs (>100 nm) because the smaller ones tend to traffic to lymph nodes, whereas the larger ones are difficult to move once accumulate at the diseased site [59]. These systems can also be used to increase local drug

concentration by carrying the drug within tumor cells and inducing the controlled release of the payload after binding to and internalization into the target cells [60]. So, NPs-based drug delivery systems for systemic (i.e., intravenous) applications have significant advantages over their free drug counterparts. Considering this, nanomedicine and nanotechnologies are not to be deemed as a futuristic revolution, but as something already in act. Indeed, in the last twenty-five years, the FDA has approved different types of NPs for cancer treatment, and, at present, many NPs are under study [45, 46, 61, 62].

Since the early 1970s, when Gregoriadis et al. established the concept that liposomes could be used as drug carriers, just like “*putting old drugs into new clothing*”[63], several different kinds of nano-carriers have been produced, characterized, and finally used for many different purposes: liposomes, micelles, dendrimer, carbon nano-material, inorganic NPs and polymeric NPs (Figure 1.5) [59].

1.2.2 Composition of nano-systems

Liposomes (Figure 1.5 **A**) are artificial vesicles composed of phospholipids and described as unilamellar or multilamellar, depending on the number of phospholipid bilayers; they can incorporate hydrophilic compounds in their aqueous compartment(s) and hydrophobic compounds in their lipid bilayer(s). Liposomes are biodegradable and easily modifiable to render them more biocompatible or facilitate specific cell targeting. Moreover, their surface can be modified to prolong their circulation and prevent their elimination from the circulatory system with the aid of natural or biocompatible polymer to shield them from opsonins, which are proteins able to bind foreign substances or cells inducing their phagocytosis. The liposome dimension is comprised of between 30nm and 50µm. They are spherical vesicles essentially made of phospholipids, which, due to their amphiphilic nature, are able to self-assemble in an aqueous solution. The polar shell is made of a lipid bilayer capable to hold lipophilic molecules. By contrast, the aqueous core can be loaded with hydrophilic molecules [64]. The surface of these structures can be functionalized with different molecules in order to target specific cells or tissues. Despite the success of liposome-based nano-carriers as drug delivery systems, their use is still limited by some technical reasons. Indeed, liposomes are characterized by low stability in long-term storage and a limited amount of loadable materials [65].

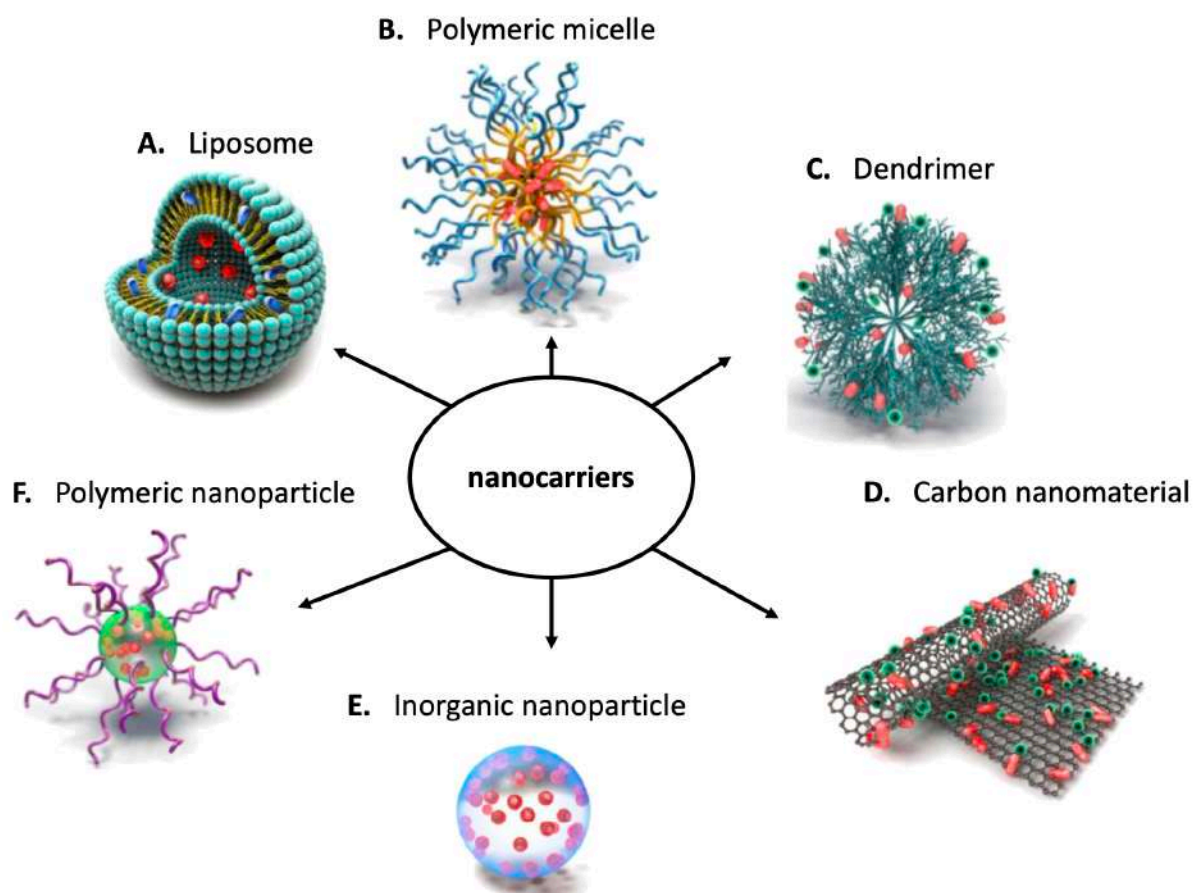


Figure 1.5: Schematic representation of nano-carriers for cancer therapy. In commerce, there are different types of nano-vectors, such as (A) liposomes, (B) polymeric micelle, (C) dendrimer, (D) carbon nano-material, (E) inorganic nanoparticle, and (F) polymeric nanoparticle (Jeong et al, 2021, modified).

Liposomes can be also designed to respond to a specific trigger signal (such as hyperthermia, pH variations, an alternation of the external magnetic field, or ultrasound) to release their content. This triggered release is extremely useful to avoid side effects and increment therapeutic efficacy. Since the first description, they have experienced exponential growth [66, 67]. Particularly, in 1995 a formulation based on these nano vectors loaded with doxorubicin and known as Doxil® was approved by FDA [68]. This formulation demonstrated an improved circulation half-life of doxorubicin and an increased accumulation in the tumor tissue [69]. To this day, more than eighteen liposomal drugs have been approved by FDA for the treatment of cancer, and many other diseases [64].

Polymeric micelles (Figure 1.5 B) are self-assembled core-shell nanostructures made by amphiphilic block copolymers. In an aqueous solution, due to their amphiphilicity, micelles have unique properties: the hydrophobic regions of the block copolymers

aggregate in order to reduce contact with water molecules producing core-shell vesicles [64]. These structures usually found application in the delivery of hydrophobic drugs which can be loaded into their core. Micelles can also be used to carry small organic molecules, peptides, carbohydrates, mAb, and DNA/RNA aptamers. Even if not yet widely utilized clinically, micelles have several advantages, such as the facility to be prepared and be loaded with drug agents, biocompatibility, and high, although limited, stability in biological fluids [70].

Differently, dendrimers (Figure 1.5 **C**) are synthetic, branched macromolecules that form a tree-like structure whose synthesis represents a relatively new field in polymer chemistry. They are fabricated through a stepwise process, which yields molecules possessing a core, interior layers composed of repeating units, and an exterior with terminal functionalities attached to the outmost generations. Dendrimers have shown to be promising for biomedical applications because they can be easily conjugated with targeting molecules, imaging agents, and drugs, have high water solubility and well-defined chemical structures and are biocompatible. Since 1984, when the first article introduced the term "dendrimer", a variety of dendrimers have been investigated for cancer treatment, but dendrimers are more expensive than other NPs and require many repetitive steps for synthesis, posing a challenge for large-scale production [37, 68, 71].

Carbon nanotubes (Figure 1.5 **D**) have also been analyzed for cancer treatment. These structures can bind to various biological materials and enter cells via endocytosis. Single-walled carbon nanotubes (SWCNTs) form highly stable suspensions in physiological buffers, making them suitable for use in biological environments. Treatments based on the use of SWCNTs are promising due to their interesting optical properties; in fact, SWCNTs can be used for photothermal and photodynamic therapy [68, 72]. However, carbon nanotubes were demonstrated to induce severe side effects such as asbestos-like inflammation and granulomas in female mice; moreover, severe impacts on the cardiovascular system were reported with specific types of carbon-based nano-materials, such as single or multi-walled carbon nanotubes [37].

Nanoparticles can be divided into two classes: organic and inorganic NPs. Inorganics NPs (Figure 1.5 **E**) are made of metal atoms (metallic), or a mixture of metal and non-metal atoms (semi-conducting). Each of these types of NPs shows peculiar features and are used for different application. Metallic NPs usually find medical applications

as diagnostic probes for magnetic resonance imaging (MRI), positron emission tomography (PET), X-ray, and optical imaging. The strength and durability of these materials are unique properties that make them suitable as delivery tools [73]. Inorganic crystalline NPs approved by the FDA are limited to hydroxyapatite and calcium phosphate for use as bone graft substitutes, nevertheless, nanocrystals are helpful to overcome the solubility issues related to several drug compounds and are marketed for a range of indications [73].

Another type of nano-carrier, frequently considered as an alternative to liposomal vehicles, is represented by organic NPs, which can be made of different polymers or lipids and due to their biodegradability are widely used for drug delivery [62]. Polymeric NPs (Figure 1.5 F) are interesting because of their improved *in vivo* stability and loading efficiency. Polymers are the most common materials for constructing NPs-based drug carriers. One of the earliest reports of their use for cancer therapy dates to 1979. Polymeric NPs are defined by their morphology and composition in the core and periphery. The therapeutic agent is either conjugated to the surface of the NP or encapsulated and protected inside the polymeric core [74]. They can be assembled in both synthetic and natural polymers and these nano-carriers have been demonstrated to be useful for a variety of applications such as imaging, detection of apoptosis, and drug delivery. Among different nanostructure morphologies for drug delivery, polymeric NP-based drug delivery shows numerous advantages for controlling the release of biological factors. These advantages include the possibility to add a selective targeting mechanism, the controlled release, protection of deliverable agents, and extension of the circulation time in the body and just like the other delivery systems, the functionalization of the NPs helps to achieve the best possible result. Among polymers, those preferred for biomedical applications are biocompatible and biodegradable, because of their reduced toxicity and the prevention of the polymer accumulation in the cells after repeated administration [75, 76]. Over the years, several different morphologies of biodegradable polymers have been fabricated and applied for drug delivery. In fact, nanomedicines should preferably be biodegradable if proposed for high dose schedules or long-term administration. Biodegradable polymers allow the utilization of higher molecular weight platforms to optimize pharmacokinetics and they are essential for the treatment of diseases that require chronic administration, e.g., for tissue repair and regenerative medicine [58].

1.2.2.1 Biodegradable polymers

Since 1976, when Langer and Folkman demonstrate that biodegradable polymers can be used for controlled release, this kind of nanodevice earned considerable success [77]. Despite the progress in the development of lipid-based NPs, polymeric materials are increasingly emerging as a better system of controlled and prolonged drug release. The process and its extent depend upon parameters relating to the nature of the carrier system. For example, the payload can diffuse through the polymer wall with a diffusion rate that is dependent on the degree of crosslinking of the matrix. Alternatively, the release can be caused by the erosion of the NPs' surface or polymer matrix degradation. Although both processes depend on a progressive alteration of the NPs' structure, the degradation of the entire polymeric network results in greater drug release [77]. Following this discovery, considerable successes have been achieved in the therapeutic field, and, over the years, several different types of polymers have been studied as potential delivery tools. The early polymeric NPs produced were based on poly(methyl methacrylate) (PMMA), polyacrylamide, polystyrene, and polyacrylates. Those were non-biodegradable and therefore they showed several issues in terms of disposal, degradation, and toxic accumulation in tissues. Thus, it was necessary to promote the elimination of NPs through carriers (e.g., feces, or urine) or physically remove them. Moreover, the use of these polymers was often associated with chronic toxicity and inflammation. These disadvantages led to a shift in the focus on biodegradable polymers. Biodegradable polymers (Figure 1.6) are both based on synthetic materials such as poly(lactide) (PLA), poly(lactide-

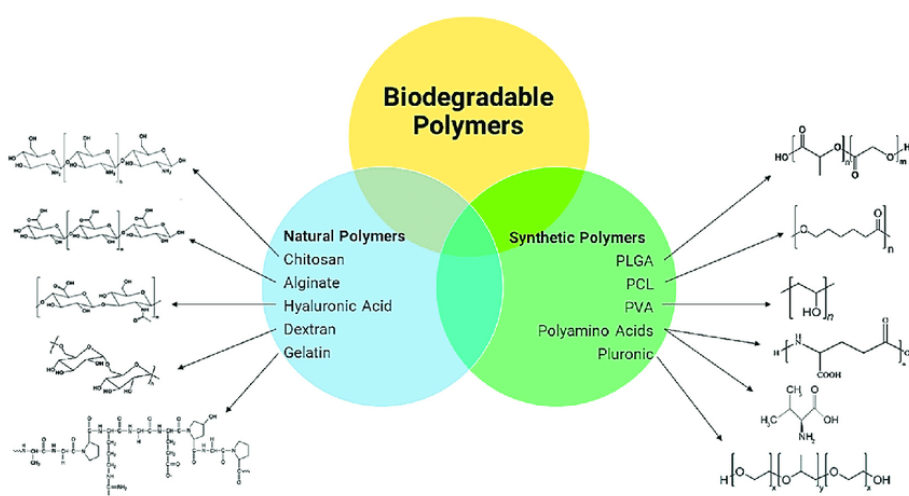


Figure 1.6: Biodegradable polymers. Examples of both natural and synthetic polymers are used in nanomedicine (Mansoor et al, 2019).

co-glycolide) copolymers (PLGA), poly(ϵ -caprolactone) (PLC), and poly(amino acids) or natural materials including chitosan, alginate, gelatin, and albumin [76, 78].

The favorable biocompatibility and biodegradability are some of the features linked to their success in drug delivery. Indeed, for a suitable outcome, after administration polymers should be disaggregated into biocompatible molecules disposable via metabolic pathways [79].

1.2.2.1.1 Chitosan polymers

Chitosan [poly (1,4- β -d-glucopyranosamine)], is a natural polysaccharide prepared by N-deacetylation of chitin, and it shows great potential as a biomaterial for the construction of nanosized drug carriers and gene transfer vectors [80]. In detail, chitosan possesses mucoadhesive and antimicrobial properties and it shows good coagulation ability and immunostimulant activity. It spontaneously forms microspheres, which could be filled with various compounds such as imaging agents and drugs. Different formulations of chitosan and its composites were investigated for medical purposes due to its biocompatibility, its ability to increase the solubility of insoluble drugs, and its safe delivery to the specific site [81]. The fact that chitosan can be sterilized explains why it has been used as a pharmaceutical excipient in oral formulations and in cosmetics. Moreover, chitosan is degraded by enzymes such as lysozyme and chitosanase into non-toxic and endogenous to the human body oligomers; a low charge density around neutral pH reduces its cytotoxicity [70]. Preferably these systems are designed in such a way that they allow for self-assembly in the presence of the drug to be incorporated [82]. Moreover, the degradation of these biodegradable polymers can be used as a tool to release nucleic acids into the cytosol. Chitosan has a strong electrostatic affinity for anionic biomacromolecules such as DNA and RNA in saline or acetic acid solution. This delivery system is advantageous as it has the added benefit of protecting DNA and RNA from degradation and it enables the controlled release of therapeutic compounds. The transfection efficiency of chitosan-DNA complexes is quite low in comparison with viral vectors, and it is shown to depend on numerous factors including the structure of the polycations used, the cell type being transfected, and NPs size and composition, in addition to the poor solubility at physiological pH [68, 83]. Nucleic acid-based therapy is a prominent, novel, and promising area in pharmaceutical and medical sciences due to its potential for treating a variety of

genetic disorders. Basically, nucleic acid-based therapy consists of two parts: first, the therapeutic nucleic acid-based itself, with plasmid DNA (pDNA) and different types of small RNA, and second, the carrier which delivers the nucleic acid-based to the desired site, including viral and non-viral vectors. Although this kind of treatment is still a challenge, it is proving to be promising. In fact, biodegradable polymeric NPs, such as chitosan, have been found to be safe and effective as carriers, by protecting the nucleic acids from degradation and cellular uptake of nuclease, without the help of transfection agents [75, 76, 84].

1.2.2.1.2 Poly(lactide-co-glycolide) and poly(vinyl alcohol) polymers

Synthetic polymers have a huge potential in the development of nano-carriers because of their chemical versatility, high purity, and controlled production process as compared to natural materials. Among the many biodegradable and biocompatible synthetic polymers, PLGA is successfully used and investigated due to its extensive properties. It is approved by the US FDA and the European Medicines Agency (EMA) as a promising drug delivery system for therapeutic agents such as chemotherapeutics, antibiotics, anti-inflammatory or antioxidant drugs, and proteins [85]. PLGA is a copolymer consisting of two different monomer units, poly(glycolic acid) (PGA) and poly(lactic acid) (PLA) which are linked together by ester linkages; the result is a linear, amorphous aliphatic polyester product. Its success is particularly related to its continued drug release compared to conventional devices. *In vivo*, the polymer undergoes degradation by hydrolysis with the following formation of the original monomers (i.e., lactic acid and glycolic acid) which are endogenous monomers also produced in normal physiological conditions. Thus, they are easily processed *via* metabolic pathways such as the Krebs cycle and removed as carbon dioxide and water, causing minimal systemic toxicity. The negative charge of the PLGA is also crucial in its activity [86] because it strongly influences the interaction between NPs and cells. Cationic surfaces promote cellular binding and uptake due to negatively charged phospholipid groups, proteins, and glycans found on surface cells. On the other hand, positively charged NPs show a rapid clearance and phagocytic uptake. In contrast, anionic NPs, as well as those with a neutral surface, show a higher circulating half-life [77]. Another synthetic and biocompatible polymer extensively studied is poly(vinyl alcohol) (PVA). It is used both in clinical and non-clinical research, in the industrial and the medical sectors. This versatility arises from

its low toxicity for human tissues and its physicochemical properties (i.e., film-forming, emulsifying, flexibility, thermostability, and water solubility) [87]. Focusing on the nanomedicine field, PVA is frequently used as an emulsifier in the formulation of PLGA NPs, due to its ability to form an interconnected structure with the PLGA, helping to achieve NPs relatively uniform and small [88].

Starting from these considerations, NPs are supposed to be interesting tools in the field of nanomedicine because of their several possible applications. However, to design a drug carrier is important to keep in mind that in the human body there are various obstacles to overcome, and therefore it is also relevant to consider how NPs are biodistributed.

1.2.3 Biological limits to nano-devices delivery

Most of the anti-tumor agents currently administered by validated therapeutic protocols are systemically distributed without preferential localization to cancer tissue. Drugs had to be administered in a high ratio to reach their target at a sufficient concentration to develop the desired effects; however, their widespread biodistribution result in both loss of anti-cancer effects and the development of off-target adverse effects. The drug toxicity includes immune hypersensitivity, off-target toxicity, and bioactivation or covalent modifications because many drugs are converted to reactive products, which induce immune responses. In addition, idiosyncratic responses are rare but one of the most problematic issues. Therefore, every time a drug is studied, research is carried out in the most efficient way to maximize efficacy, while reducing side effects. In fact, toxicity has been evaluated to be responsible for the retreat of ~ 1/3 of drug candidates and it is a major contributor to the high cost of drug development, particularly when not recognized, until late in the clinical trials or post-marketing [89]. Basically, the possibility that any molecule has sufficient therapeutic efficacy and target recognition specificity, as well as all the tools required to bypass multiple biological barriers, is probably unrealistic. A different approach is to decouple the problem. For example, it is possible to propose drugs for their therapeutic action only and deliver them to a specific microenvironment by vectors that can be preferentially concentrated at desired body locations through the concurrent action of multiple targeting mechanisms; this approach increases drug efficacy and safety including the use of NPs as drug delivery systems for cancer therapeutic approaches

[65, 89]. Since Paul Ehrlich, considered the “father of chemotherapy”, suggested the concept of a “magic bullet”, i.e., “a drug that selectively attaches to diseased cells but is not toxic to healthy cells” approximately a century ago, a great deal of interest has been channeled to overcome several obstacles that drugs meet before reaching their target [90].

The kidneys represent an obstacle to the efficacy of NPs because of the risk of premature elimination, in which NPs are eliminated prior to arriving at the target tumor tissue. In fact, they are responsible for filtering circulating blood, and therefore the barriers involved in kidney filtration need to be considered when designing NPs. After passing through the fenestrated endothelium, NPs must pass through the glomerular basement membrane. Size, charge, and shape are all characteristics that affect the clearance of NPs in kidneys. Spherical NPs with diameters less than 6 nm were shown to have greater renal clearance than those with diameters greater than 8 nm. The glomerular basement membrane is negatively charged, and therefore cationic NPs of 6-8 nm exhibit greater clearance than those negatively charged or neutral of the same size [85, 91, 92]. Moreover, highly cationic NPs are rapidly cleared from circulation by kidneys to a greater extent than highly anionic NPs. In contrast, neutral NPs, as well as those with a slight negative charge, show significantly prolonged circulating half-lives. This translates to improved accumulation in tumors, which in turn has led to recent research efforts aimed at functionalizing NPs with zwitterionic surfaces.

Another important feature that affects *in vivo* nano-carriers' fate is the size; in fact, larger particles (>200 nm) are rapidly cleared by phagocytic cells found in the liver and spleen [93, 94]. Injected NPs are not “self” and the body tends to eliminate these foreign bodies. The most efficient way to recognize and bind these “non-self” agents is the attachment of serum proteins, particularly opsonins, creating a “biomolecular corona” around the NPs [95]. At this point, as exemplified in Figure 1.7, NPs coated by opsonins are recognized by Mononuclear Phagocyte System (MPS), which is located in the liver, the spleen, the lungs, and in inflammatory tissue [96].

This process causes a release of cytokines, increasing NPs clearance from the bloodstream and local inflammation of the tissue. In this way, it is clear that NPs are rapidly eliminated, so they cannot exercise their therapeutic action. Starting from these considerations, it is obvious to focus on defining methods to make NPs stealth and limit the process. Surface modifications of NPs may permit escape from the RES

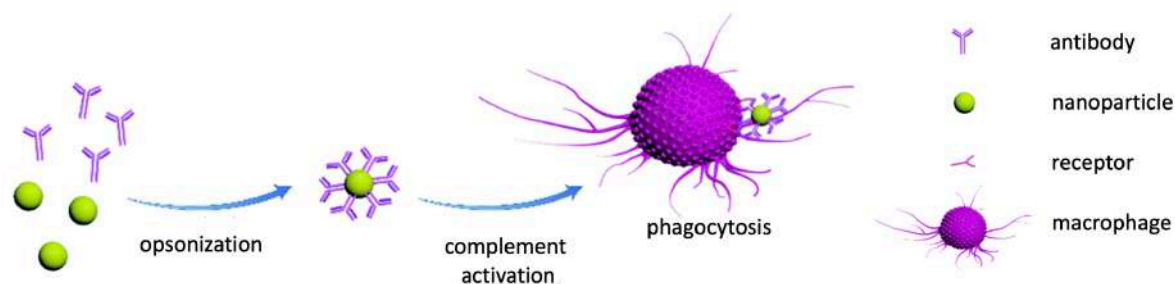


Figure 1.7: Opsonization process. Serum proteins are absorbed on the NPs' surface leading to the opsonization process; opsonized particles are subsequently recognized through receptors on phagocytic cells and then internalized (Wang et al 2021, modified).

and prolong their circulation time in the bloodstream while preventing damage to normal tissue [96].

Successful strategies to reduce and avoid the engulfment by the MPS were developed, including the NPs' surface functionalization with sterically shielding and hydrophilic polymers, such as PEG. This strategy prevents or minimizes or modifies the protein absorption, resulting in less vulnerability and prolonged circulation half-life [97-99]. Besides PEG, alternative NPs' surface modification approaches are under investigation, including those involving endogenous components, such as proteins and lipids.

1.2.3.1 Protein corona

NPs, when injected into the bloodstream, interact with more than 3000 circulating proteins [100]. Due to the high surface-area-to-volume ratio, NPs attract plasma proteins (e.g., albumin, complement proteins, fibrinogen, and Igs) onto their surface, to form a coating layer called protein corona (PC). Its formation is a time-dependent process that affects the biological identity of NPs and consequently their functionality and safety [101]. The process is based on the spontaneous absorption of circulating protein around the NPs, immediately after their administration in a biological environment. Interestingly, the protein corona is not a solid and fixed layer because its composition changes over time depending on the plasma proteins' concentration. Although the composition of a PC is controlled by multiple factors, in general, according to the binding affinity and rate of exchange of proteins from the NP's surface, the PC around a NP can be divided into two parts: a "hard" corona and "soft" corona (Figure 1.8).

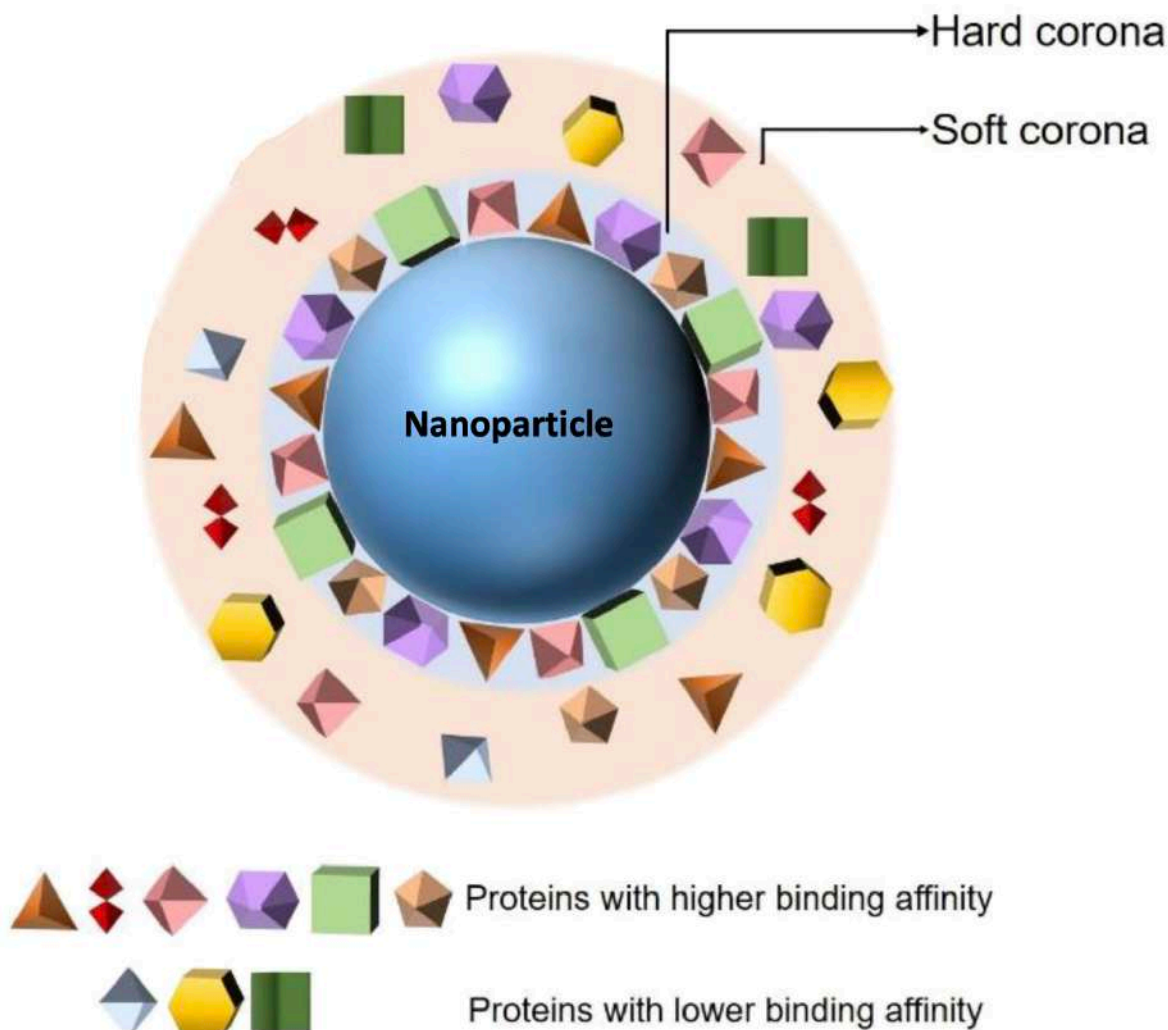


Figure 1.8: The duality of the protein corona. Proteins with a smaller size and lower affinity constitute the so-called “soft” corona. They are loosely attached to the NPs’ surface and relocate from the NP’s surface rapidly. This promotes the replacement of less abundant proteins with those with higher affinity belonging to the “hard” corona (Li e Lee 2020, modified).

In this regard, binding and exchanging are the pillars of this dynamic process that can be described by the “Vroman Effect”. According to this phenomenon, initially, blood proteins highly concentrated with smaller sizes (e.g., albumin) interact first with NPs, forming a coating called “soft” corona. They are loosely attached to the NPs’ surface and relocate from the NP’s surface rapidly. This promotes the replacement of less abundant proteins with those with higher affinity. Proteins that have been proven to have a high binding affinity with the surfaces of NPs belong to the “hard” corona and are generally located in the inner layer of the PC. “Soft” PC constitutes the outer layer of the PC and can be easily exchanged with the proteins existing in the biological environment, owing to the abundance of proteins in biological fluids and their direct contact with each other. Furthermore, a “soft” PC may interact with the formed “hard”

PC layer on the NP's surface, via weak protein-protein interaction. The "hard" PC's protein rate of exchange from the NP surface is slow, but this process plays an important role in defining the NPs' activity and biological fate [102-105]. This process of adsorption of proteins on the surfaces of NPs is a dynamic process and it is associated with the continuous adsorption/desorption equilibrium of the proteins on and off the NP surfaces; the kinetics are described by association (K_{on}) and dissociation (K_{off}) constants [105].

The extent of the coating can also change according to NPs' physicochemical properties. For example, anionic NPs are less susceptible to this phenomenon, unlike the cationic ones in which the positive charge promotes the absorption of opsonins [106]. In addition to the nano-materials, a focal role is certainly performed by the nature of the absorbed proteins, which can be classified as opsonins and dysopsonins. Opsonins (i.e., Ig, coagulation, and complement proteins) promote the recognition by MPS. In contrast, dysopsonins such as apolipoproteins and albumin reduce the absorption of opsonins conferring stealthiness and decreasing clearance [94]. In line with this, a promising surface modifier should be albumin. Generally, human serum albumin (HSA) and bovine serum albumin (BSA) are two types of serum proteins used in constructing or coating NPs, due to properties such as high solubility and long half-life in the blood. Albumin is the most abundant plasma protein in the human body, involved in the transport of nutrients and other proteins through the bloodstream. Since albumin is an endogenous protein, it has been widely used as an excipient in clinical formulations mostly for its biocompatibility and less immunogenicity [107]. Several features contribute to using albumin in drug delivery. For example, albumin is exploited by many cancer cells as a source of energy and nutrient, due to the enhanced uptake *via* macropinocytosis, which is an endocytic process. Also, its role as dysopsonin in the protein corona contributes to reducing the binding and absorption of other plasma proteins and, consequently, the MPS uptake [108]. For this reason, a preformed protective albumin corona should limit these non-specific interactions and decrease the complement activation. In addition to reducing clearance, albumin has also structural advantages; both amino and carboxylic groups can be employed for the functionalization of NPs' surfaces by targeting ligands to facilitate the transport and accumulation to the tumor site [105]. Therefore, beyond the improvement of the NPs' half-life, it is important to consider the NPs' distribution inside the tumor tissue.

1.2.3.2 The impact of targeting tumor cells

Despite the advancements in cancer therapy, chemotherapeutics-related toxicity remains still an obstacle. The cause is the inability of these agents to target the neoplastic areas without impact on healthy tissues. Consequently, after administration, they spread out resulting in off-target effects and systemic toxicity. Starting from these considerations, the research has focused on developing targeting systems capable of overcoming these pitfalls [65]. Targeting strategies should be both passive and active, also associated with stimuli-sensitive mechanisms. In this way, the drug release occurs upon internal (i.e., pathophysiological/patho-chemical conditions) or external (i.e., physical stimuli such as temperature, light, ultrasound, and magnetic force) triggers. The result is the enhanced intracellular delivery and consequently suitable therapeutic outcomes by using conditions present in the neoplastic tissue, minimizing systemic exposure, and limiting potential harm [109].

1.2.3.2.1 Passive targeting in the tumor microenvironment

Solid tumors are characterized by a vasculature that is heterogeneous in size and distribution, having a central avascular/necrotic region and a vascularized peripheral region, with discontinuous endothelium in the micro-vessels. In fact, depending on the anatomic region of a tumor, the pore size of the endothelial junctions varies from 100 to 780 nm with a mean of approximately 400 nm (while normal vasculature is characterized by pores smaller than 10 nm) characterizing the leaky microvasculature of tumors; it is also characterized by a disrupted basement membrane, abnormal branching, and enlarged inter-endothelial gaps, with an associated breakdown of tight junctions between endothelial cells. Moreover, tumor vasculature shows a lack of lymphatic drainage, it is rich in fenestrations and poor in pericyte coverage. All these features contribute to the enhanced permeability and retention (EPR) effect, firstly described by Maeda and co-workers [110]; the tumor vasculature architecture allows extravasation and selective accumulation of nano drugs in the tumor interstice via a passive targeting mechanism [65, 111, 112]. The small molecules tend to diffuse freely in and out of tumor blood vessels because of their small sizes, and thus do not accumulate in tumors as much as macromolecules do over time. These large gaps between endothelial cells facilitate the extravasation of particulate material from the surrounding vessels into a tumor (Figure 1.9) but EPR-dependent drug delivery is always compromised by regional blood flow rates, molecular size, polarity, and

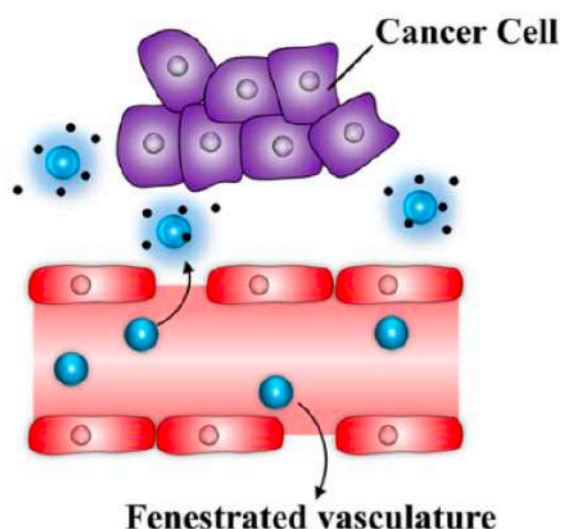


Figure 1.9: Passive targeting. In passive targeting, nanoparticles are designed for transport through leaky vessels and the unique intra-organ pressures of tumors (Aghebati-Maleki et al, 2019).

complexation to serum proteins, which are all factors that reduce the capability of bypass the membranes of the endothelium [110, 113].

However, there are stimulators that result in an enhanced vascular permeability and extravasation of macromolecules and thus increase the EPR effect. EPR augmenting factors include vasoconstrictors to raise the systemic blood pressure, free radicals that affect the integrity of vascular endothelium, and vascular permeability promoters [114]. Therefore, it is clear that the EPR effect is a very heterogeneous

phenomenon, varying dramatically from tumor to tumor and from patient to patient. As a consequence, passive targeting strategies have shown several limitations, so an alternative is represented by the investigation of tumor-selective active targeting nano-formulations that can maximize the accumulation at sites of interest [115, 116].

1.2.3.2.2 Active targeting in the tumor microenvironment

Active targeting systems are developed for selectively delivering cargo to cancerous cells without harming normal cells. This selectivity is based on molecular recognition of the over-expressed receptor/antigen on cancerous cells and by the use of targeting molecules on the surface of nano-systems; to potentially benefit from the active targeting strategy, it is imperative that the specific antigen has been present on the targeted cells and accessible to bind the NPs. It is also important that tumor antigen localization and expression remain adequate throughout the treatment. In this respect, NPs, and in particular polymeric NP, allow for versatile modification possibilities and can act as functional platforms for the assembly of well-defined multifunctional structures. In fact, slight variations in polymeric composition as well as ligand surface functionalization can facilitate the targeting ability of NPs in biological systems. Active drug targeting involves the use of a variety of affinity ligands to direct

the binding of NPs to many biological targets, largely represented by antigens differentially over-expressed both in the tumor cells, vessels endothelium in the tumor microenvironment, or in other diseased tissue (Figure 1.10) [65, 111, 117].

Moreover, margination dynamics to endothelial walls is a very important NPs-design consideration. In fact, the small spherical particles are found in a particular region of the vessel known as the cell-free layer, which is the result of the tendency of red blood cells to accumulate preferentially within the core of a vessel. NPs' tight association with vessel walls favors particle-cell binding and receptor-ligand interactions in active targeting strategies and enables extravasation through the fenestrated vasculature of tumors. So, NPs fluid dynamics in blood vessels are highly dependent on the size and geometry of the construct [56, 118].

Since the primary role of the targeting ligand is to enhance the uptake of NPs into target cells, NPs' internalization through active targeting is postulated to improve the therapeutic efficacy as compared with non-targeted NPs. This suggests that while the biodistribution would be strictly related to the colloidal properties of the NPs, the targeting ligand is important for enhancing both cell recognition and cell uptake at target sites [65, 85]. As a result, an important step in the design of the nano-carrier is represented by the choice of an appropriate targeting ligand.

Different classes of targeting agents can deliver NPs in specific tissues, including proteins (e.g., antibodies or their fragments), aptamers, or small molecules such as vitamins and peptides. Antibodies are the most common molecules used as therapeutic and targeting ligands, due to their high specificity and affinity. Indeed, their use showed a new perspective on disease treatment [90]. Limits to be considered in their application are related to their size and potential immunogenicity. These restrict their density on the NPs' surface and increase the diameter of NPs. However, the

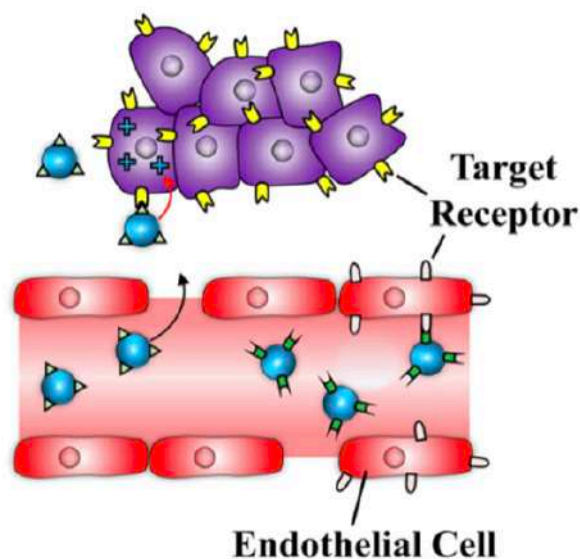


Figure 1.10: Active targeting. In the active targeting of cancer cells or tumor-endothelium nanoparticles are designed to bind specific biological structures through the molecular recognition of surface-bound ligands (Aghebati-Maleki et al, 2019, modified).

improvement of molecular technology allows circumventing these inconveniences through engineered antibodies, including single-chain variable fragments (scFv), or antigen-binding fragments (Fab) [77]. However, it is important to keep in mind that, depending on the type of ligand-receptor interaction, the type and the degree of cellular internalization would be different; moreover, proteins in biological serum were reported to shield targeted NPs by the formation of protein corona which may impact the targeted delivery [119, 120].

1.3 Therapeutic approaches to B-cell malignancies

B-cell malignancies arise from different stages of B-cell differentiation and constitute a heterogeneous group of pathologies. For this reason, they possess intra- and inter-patient differences that can greatly influence both the selection and the duration of the treatment [121]. During the last years, many various therapeutic approaches were investigated, such as chimeric antigen receptor (CAR) T-cell therapy and immune checkpoint inhibitors (ICIs), that have shown potential for improving the outcomes of patients with refractory B-cell malignancies [122]. Alternatively, strategies engaging innate immune cells to fight B-cell malignancies represent an attractive and rapidly evolving field. For what concerns the mAb therapy, there are plenty of possibilities, including different Fc-engineering strategies to enhance antibody-dependent cellular cytotoxicity (ADCC), antibody-dependent cellular phagocytosis (ADCP), complement-dependent cytotoxicity (CDC) [123]. Unfortunately, even if the treatment with CAR-T cells has produced remarkable clinical responses with certain subsets of B-cell malignancies, there are many limitations in the therapeutic efficacy, including severe life-threatening toxicities, modest anti-tumor activity, and antigen escape, and restricted trafficking. In addition, the host and tumor microenvironment interactions with CAR-T cells critically alter CAR-T cell function [124]. On the other hand, mAb therapy is, for definition, precise and selective for the selected antigen, but mostly is still used in combination with dose-intensive chemotherapy regimens that are not cell-specific, leading to the development of off-target side effects [125].

Thus, on this basis, it is interesting to develop a strategy that takes advantage of "next-generation" treatments, which combines the knowledge about NPs with drug efficacy. This alternative approach, based on nano-carriers, offers the possibility to take advantage of the specificity and selectivity of the targeting mechanism and in the meanwhile encapsulating the drug or the therapeutic molecule, avoiding off-target

side effects and reducing the costs of disease management because the doses required to achieve the same efficacy as untargeted drugs might be lower [54]. Through this approach different classes of therapeutic molecules can be investigated, alone or in combination.

1.3.1 miRNA-17~92

MicroRNAs (miRNAs) are a class of single-stranded, non-coding small RNAs of about 22 nucleotides in length, that are able to bind to target mRNAs via partial or complete complementary base pairing. miRNAs regulate gene expression and may inhibit oncogenes or tumor-suppressor genes at the post-transcriptional level. In fact, each miRNA is theoretically capable of regulating hundreds of mRNAs within a cell type and in a context-dependent manner. Considering their roles, it is not surprising that the abnormal expression of miRNAs is associated with several pathologies, thus making miRNAs useful clinical biomarkers that may be used in the diagnosis, treatment, and prognosis of tumors. In fact, it was recently reported that the pattern of miRNA expression varies dramatically across tumor types and that miRNA profiles reflect the developmental lineage and differentiation state of a tumor [126]. Particularly, the imperfect base pairing of a miRNA with complementary sequences located mainly in the 3'-UTR or 5'-UTR of the target transcripts leads to mRNA degradation or translational repression. This highly evolutionarily conserved RNA family represents approximately 800 miRNAs in the human genome and could regulate the expression of more than half of all protein-coding genes. Therefore, miRNAs are involved in the regulation of a plethora of biological processes, such as cell differentiation, proliferation, metastasis, metabolism, apoptosis, tumorigenesis, angiogenesis, and others [127]. miRNAs are also likely to play critical roles in various aspects of hematopoiesis, including the differentiation of hematopoietic stem/progenitor cells, and in events that lead to hematological disorders [128, 129]. In 2005, He et al first discovered the miRNA-17~92 cluster, which is amplified in several hematopoietic malignancies and solid tumors [130]. This cluster, also known as oncomiRNA-1, is a typical highly conserved polycistronic miRNA cluster, which is located in the human chromosome 13 and encodes for six mature miRNAs including miRNA-17, miRNA-18a, miRNA-19a, miRNA-19b, miRNA-20a, and miRNA-92a. miRNA-17~92 is probably the most well-studied cluster in the literature because it is involved in the tumor-genesis of different tumors, including B-cell malignancies [131].

Several microRNAs associated with the miRNA-17~92 cluster play decisive roles in organizing the normal development as well as the events controlling the cellular proliferation in a variety of cell types, including cells of lymphoid, epithelial, and neural origin. Therefore, the regulations imposed by the miRNA-17~92 cluster components in the context of proliferation are extremely diverse and complex [132-134]. The miRNA-17~92 cluster plays a crucial role in tumorigenesis, mainly via the activation of oncogenes and the inactivation of tumor suppressor genes (Figure 1.11).

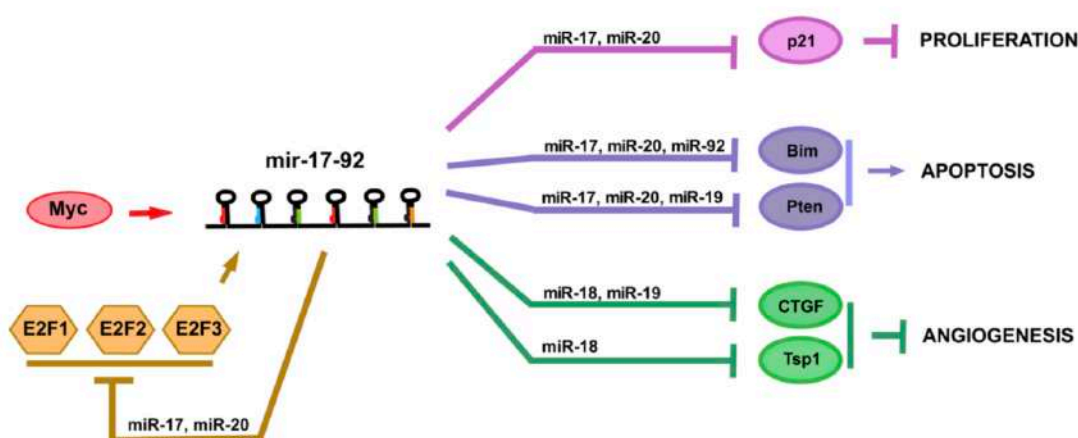


Figure 1.11: The pleiotropic functions of miRNA-17~92 achieved by repressing specific targets. Depending on both cell type and physiological context, miRNA-17~92 can promote proliferation, increase angiogenesis, and sustain cell survival through the post-transcriptional repression of a number of target mRNAs (Olive et al. 2013).

In detail, the up-regulation of the miRNA-17~92 cluster inhibits the expression of the tumor suppressor p21 and the apoptotic gene Bim in lymphoma, leading to the uncontrolled proliferation of cancerous cells. The first confirmed miRNA-17~92 transcription factor was MYC, which is involved in multiple mechanisms regulating gene expression. Over-expressed in approximately half of the human cancers, MYC binds to specific genomic sites, directly activating miRNA-17~92 expression. Along with MYC, the transcription factors E2F1, E2F2, and E2F3, which are members of the E2F family, have been identified as target genes of miRNA-17 and miRNA-20a [131, 135].

Like all the other microRNAs, the members of the miRNA-17~92 cluster function post-transcriptionally by forming complexes with the mRNAs of different target genes to either degrade or reduce the translational efficiency of the corresponding target mRNA. The regulation of almost all cellular processes occurs through several signaling pathways and the Janus kinase/signal transducer and activator of

transcription (JAK-STAT) pathway play a pivotal role in the mechanism of action of the miRNA-17~92 cluster [126]. So, the miRNA-17~92 cluster, acting as an oncogene, induces tumor cell invasion and metastasis by regulating its target genes [136]. The major functional evidence of the oncogenic activity of miRNA-17~92 comes from *in vivo* studies employing B-cell lymphoma mouse models. Of note, the over-expression of miRNA-17 and miRNA-19b promotes the oncogenesis of MYC- expressing B-cells [131, 137]. Moreover, according to another study, mice with exogenously induced miRNA-17~92 overexpression in lymphocytes B developed an aggressive lymphoproliferative disorder associated with autoimmunity and followed by a premature death; this reflects the features of B-cell malignancies, such as splenic B-cell lymphomas or B-cell leukemia/lymphomas, which highly overexpress miRNA-17~92 [137]. Moreover, mice, characterized by an overexpression of miRNA-17~92 in the hematopoietic lineages, developed a B-cell malignancy in which the B-cells proliferate more readily in response to various activation stimuli and resist cell death [138].

All these studies further highlighted the ability of miRNA-17~92 to drive tumorigenesis. Particularly, among the miRNAs belonging to the miRNA-17~92 cluster, miRNA-17 and miRNA-20a are those that target the largest number of genes. In particular, these miRNAs are able to control the expression of genes with antagonizing functions, e.g. promoting or suppressing cell cycle progression [137]. Therefore, interfering with the miRNA-17~92 cluster in clinical practice represents a promising approach, considering the accumulating evidence on its specific functions. The study of miRNAs with clinical aims may pave the way for major advances in cancer treatment in the near future [139-141]. In detail, Krutzfeldt and colleagues developed a pharmacological approach for silencing miRNAs *in vivo*, designing chemically modified, single-stranded RNA analogs, complementary to a molecule of interest [142]. This class of chemically engineered oligonucleotides able to silence endogenous miRNAs is defined as AntagomiR-17. Therefore, decreasing the level of a specific miRNA with an AntagomiR-17 is possible to freeze or even decrease the cancerous process in B-cell malignancies.

1.3.2 Anthracyclines

Anthracyclines are a class of cytostatic antibiotics, introduced into the clinical field in the 1960s. Sixty years on from its discovery, anthracycline anti-tumor alike continue to

evoke considerable interest in basic science and clinical trials research [143-145]. In fact, anthracycline chemotherapy regimens play a prominent role in many cancer treatments; e.g., 50 to 60% of childhood cancer survivors are treated with an anthracycline regimen to the point that anthracyclines are listed among the WHO model list of essential medicines [146]. The four most common anthracyclines are doxorubicin, daunorubicin, epirubicin, and idarubicin (Figure 1.12). Doxorubicin and daunorubicin were the first to be used in clinical practice and the discovery of doxorubicin from *Streptomyces peucetius* and its precursor daunorubicin was a milestone in antibiotic overproduction techniques of the day [147].

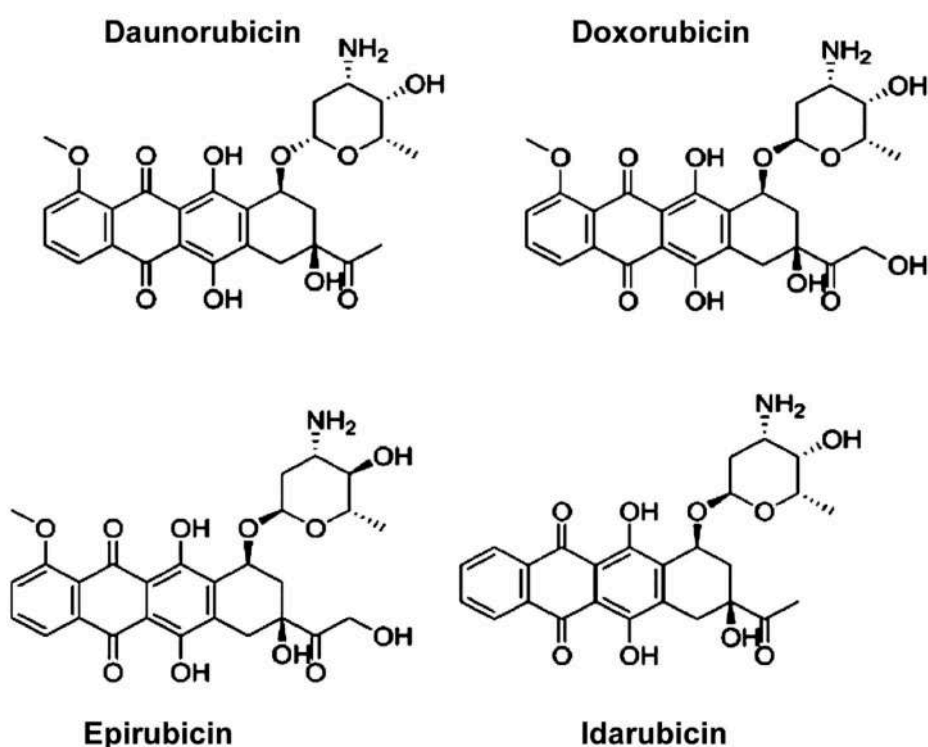


Figure 1.12: Chemical structures of clinically approved anthracyclines. Among anthracyclines clinically approved there are Daunorubicin, Doxorubicin, Epirubicin and Idarubicin (Tripaydonis et al, 2018, modified).

Despite their widely acknowledged efficacy, significant restrictions are associated with anthracycline treatment. Doxorubicin exerts its cytotoxic effect by intercalating DNA. Doxorubicin binds with DNA and topoisomerase 2 isoenzymes forming a ternary Top2-doxorubicin-DNA complex, which causes double-stranded DNA breaks. In humans, Top2 is expressed as isoenzymes Top2 α and Top2 β . Top2 α is highly expressed in proliferating cells, and it is essential for chromosomal segregation and its expression varies during the cell cycle. Differently, Top2 β is more abundant in quiescent cells, such as adult mammalian cardiomyocytes, and its expression

remains constant throughout the cell cycle. The complex inhibits DNA replication when bound to the “ α ” isoform, arresting the cell cycle, and inducing apoptosis. Conversely, when bound to the “ β ” isoform, mitochondrial dysfunction is triggered by the suppression of the peroxisome proliferator-activated receptor (PPAR), which regulates oxidative metabolism. This leads to an activation of the altered P53 tumor suppressor pathway, β -adrenergic signaling, mitochondrial dysfunction, and increased apoptosis [145, 147]. Nevertheless, with increased long-term cancer survivorship, there are also side effects. The most relevant is cardiovascular toxicity, which became apparent soon after the widespread use of anthracyclines in the 1970s, but the more recent concept of ‘cardiotoxicity’ has no standard definition. The exact mechanism of anthracycline-induced cardiotoxicity remains unclear, though it is likely to be multifactorial. Until recently, the most widely accepted hypothesis was that anthracyclines interfered with redox cycling, resulting in DNA damage due to reactive oxygen species (ROS) production. Other studies suggest that topoisomerase 2 operates as the main mediator of cardiotoxicity, through other mechanisms [143, 147]. In particular, without Top2 β , doxorubicin cannot bind directly to DNA, and animal studies with Top2 β knock-out mice have shown that the absence of Top2 β protects against doxorubicin-induced cardiotoxicity and this is probably partially due to reduced mitochondrial dysfunction [146]. Adding to the dose-related risk of cardiomyopathy, a range of other factor risks also accounts for the development of cardiotoxicity, as observed in the elderly (aged ≥ 65 years old) or child (less than 4 years old), female gender, pre-existing hypertension, and/or cardiac disease, besides coexisting treatment with cyclophosphamide, paclitaxel, and trastuzumab [148]. Moreover, cancer-treatment-related cardiotoxicity is increased in younger (especially those aged <7 years), female patients, chest radiotherapy, higher doses of anthracyclines, as well as higher body fat composition [146].

So, on these bases, in opposition to traditional therapy for B-cells malignancies, based on the use of dose-intensive chemotherapy regimens, it is interesting to develop a strategy that combines the knowledge about drugs with newborn nano-carriers. This alternative approach is supposed to be more specific, thanks to the specific targeting mechanism, and at the same time with fewer side effects. Therefore, it is possible to selectively treat the pathology through encapsulated chemotherapy or interfere in the dysregulated process, like miRNA overexpression,

reducing its level, and stopping the proliferation of cancer cells. In this way, developing a novel therapeutic approach based on biodegradable NPs, equipped with a specific targeting antigen (i.e., anti-CD19 or anti-CD20), and containing the drug (i.e., AntagomiR or anthracyclines), it is possible to selectively identify specifically malignant B-cells and obtain a more specific and safe treatment.

2. Aim of the project

ALL and BL represent the first and the fourth most common childhood cancer, respectively. It is generally not possible to prevent malignancies in children, and the most effective strategy to reduce the cancer burden is to focus on a prompt, correct diagnosis followed by effective, evidence-based therapy [4].

The management of patients suffering from ALL and BL were both helpful to highlight the limitation of the conventional chemotherapeutic approach. In fact, the chemotherapy intensity has been raised to the limit of tolerance, therefore there is a need for novel therapeutic approaches able to further improve therapeutic outcomes with a simultaneous reduction of adverse effects [28].

The aim of this work is to develop a strategy that combines knowledge about new and old drugs with newborn nano-carriers. In this way, it is possible to include a high dose of a drug, that actively reaches its target and specifically releases its content, increasing the efficacy, and parallelly reducing side effects [45]. In particular, we focused on:

- two different drug delivery systems based on biodegradable nano-carriers, in order to define which is the best option able to conceal from the IS and selectively deliver the treatment to the target,
- two different tumor-associated antigens and, as a consequence, two different targeting agents (i.e., anti-CD19 or anti-CD20), able to address all B-cell malignancies,
- two different drugs (i.e., AntagomiR-17 or anthracyclines), as examples of new and old approaches to induce tumor cell cytotoxicity,

with the final aim to develop a characterized nano-platform useful as a general drug delivery system.

The conceptualization, production, and characterization, *in vitro* and in animal models, of two different nanotechnological approaches for the treatment of B-cell malignancies were summarized in the data collected during the PhD period.

3. Materials and methods

Materials and solutions

- 3-(4,5-Dimethylthiazol-2-yl)-2,5-Diphenyltetrazolium Bromide (MTT, Sigma-Aldrich Co., St Louis, MO, USA)
- 4',6-diamidino-2-phenylindole (DAPI, Sigma-Aldrich Co., St Louis, MO, USA)
- 5-Bromo-4-Chloro-3-Indo-1-yl-phosphate (BCIP, Sigma-Aldrich Co., St Louis, MO, USA)
- Acrylamide/Bis-Acrylamide gel (stacking 5%, resolving 10%, thickness of 1.5mm)
- Alkaline phosphatase (AP) Buffer: Tris-HCl 100mM, NaCl 0,1M, MgCl₂ 5mM pH 9.6
- AP-conjugated streptavidin (Jackson ImmunoResearch Laboratories Inc., Cambridge House, UK)
- Bjab cells, a BL-like cell line
- Blocking Solution: PBS 1X added with 2% of rat serum
- Bürker chamber (Marienfeld-Superior, Germany)
- CaCl₂ 20mM
- Calcein-AM permanent dye (Thermo Fisher Scientific, Waltham, MA, USA)
- CFD-EGTA (CFD, NaCl 142mM, Na-5-5-dietylarbiturato 5mM, MgCl₂ 0.5mM, agar 0.05%, NaN₃ 0.01%, EGTA 10mM)
- CHO (Chinese Hamster Ovary) cells, an epithelial cell line, which are often used for the production of recombinant therapeutic proteins
- Complement fixation diluent (CFD, NaCl 142mM, Na-5-5-dietylarbiturato 5mM, MgCl₂ 0.5mM, CaCl₂ 0.15mM, agar 0.05%, NaN₃ 0.01%)
- Culture medium:
 - RPMI-1640 medium (Sigma-Aldrich Co., St Louis, MO, USA) supplemented with 10% fetal bovine serum (Sigma-Aldrich Co., St Louis, MO, USA), 1% penicillin-streptomycin (Sigma-Aldrich Co., St Louis, MO, USA) and 1% L-glutamine (Sigma-Aldrich Co., St Louis, MO, USA)
 - ExpiCHO™ Expression Medium (Thermo-Fisher Scientific, Waltham, MA, USA) enriched with 10U/mL penicillin, 1µg/mL streptomycin, 10% FBS, 2mM L-glutamine, and 200µg/mL Hygromycin B
- Dimethylsulfoxide (DMSO, Sigma-Aldrich Co., St Louis, MO, USA)
- Docetaxel (10mg/mL, Baxter Healthcare Corporation Deerfield, IL, USA)
- Doxorubicin (25mg/mL, Pfizer Inc., New York, NY, USA)

- E3 medium 1X supplemented with methylene blue 0,5 %
- E3 medium 1X supplemented with Phenylthiourea (PTU, 0.2mM)
- E3 medium 60X (38.4g NaCl, 1.6g KCl, 5.8g CaCl₂·2H₂O, 9.78g MgCl₂·6H₂O)
- Ethylene glycol tetra-acetic acid (EGTA, 0.5M, pH 7.4, Sigma-Aldrich Co., St Louis, MO, USA)
- Ethylenediamine tetra-acetic acid (EDTA, 0.5M, pH 7.4, Sigma-Aldrich Co., St Louis, MO, USA)
- Glass capillary (Drummond Scientific Co., Broomall, PA, USA)
- Glycine buffer (0,1M Glycine, 0,1mM MgCl₂ and 0,1mM ZnCl₂, pH 9.6)
- Goat anti-human AlexaFluor-488 antibody (1mg/mL, Sigma-Aldrich Co., St Louis, MO, USA)
- Goat anti-human serum albumin biotin-conjugated (Sigma-Aldrich Co., St Louis, MO, USA)
- Goat anti-human AP-conjugated (Jackson ImmunoResearch Laboratories Inc., Cambridge House, UK)
- Goat anti-human serum albumin antibody (Sigma-Aldrich Co., St Louis, MO, USA)
- Goat anti-mouse AP-conjugated (Jackson ImmunoResearch Laboratories Inc., Cambridge House, UK)
- H₂O MilliQ filtered 0.2µm
- Human anti-human CD19 scFv-Fc (1mg/mL)
- Idarubicin (25mg/mL, Pfizer Inc., New York, NY, USA)
- Killik (Bio Optica, Milan, Italy)
- Mec-1, a CLL cell line
- Mounting medium: 2,5% 1,4-Diazabicyclo[2.2.2]octane (Sigma-Aldrich Co., St Louis, MO, USA), 90% glycerol (Sigma-Aldrich Co., St Louis, MO, USA) in PBS 10X (NaCl 1.37mol/L KCl 27mol/L, Na₂KPO₄ 100mol/L, KH₂PO₄ 18mol/L pH 8.8)
- Mouse anti-human C5 antibody (10mg/mL Soliris, Alexion Pharma, Italy)
- Mouse anti-SV₅ antibody
- Mutton red blood cells (EA)
- NaCl 0.9%
- Nalm-6 cells, an ALL-like cell line kindly provided by Prof. Gabriele Stocco
- NBs: Chitosan (1.59mg/mL) nanobubbles conjugated (NB2, and NB3) or not (NB0, and NB1) with rituximab (0.1mg/mL), and filled with Coumarin 6 (C6, 0.05mg/mL),

and Cyanine 5.5 (Cy5.5, 13mg/mL; NB0, and NB2) or AntagomiR-17 (0.8mg/mL, NB1, and NB3), were kindly provided by Prof. Roberta Cavalli (University of Turin)

- Nitro Blue Tetrazolium (NBT, Sigma-Aldrich Co., St Louis, MO, USA)
- Normal human plasma (NHP)
- Normal human serum (NHS)
- NPs: PLGA (30mg/mL) and PVA (2% w/v) uncoated in NP0 and NP3, coated with Human Serum Albumin (HSA, 7.5mg/mL) in NP1, and NP4 or coated with HSA (6mg/mL) and an anti-CD19 Single Chain Fragment Variable linked with a human Fc (ScFv-Fc; 1.5mg/mL) in NP2, and NP5. NB0, NP1 and NP2 were filled with FITC-conjugated Bovine Serum Albumin (BSA-FITC, 20mg/mL), while NP3, NP4, and NP5 with Doxorubicin (25mg/mL).
- p-nitrophenylphosphate (pNPP, Sigma-Aldrich Co., St Louis, MO, USA)
- Paraformaldehyde (PFA) 3% (Sigma-Aldrich Co., St Louis, MO, USA)
- PBS 1X added with Tween 0,1% (Sigma-Aldrich Co., St Louis, MO, USA)
- Phorbol 12-myristate-13-acetate (PMA, Sigma-Aldrich Co., St Louis, MO, USA)
- Phosphate Buffer Saline (PBS) 1X (NaCl 137mmol/L, KCl 2.7 mmol/L, Na₂KPO₄ 10 mmol/L, KH₂PO₄ 1.8 mmol/L pH 7.4)
- Rabbit anti-rat TRITC-conjugated (Sigma-Aldrich Co., St Louis, MO, USA)
- Rat anti-mouse CD68 (1 mg/mL, Sigma-Aldrich Co., St Louis, MO, USA)
- Rituximab (10mg/mL Roche, Monza, Italy)
- Sample buffer: Tris-HCl 61.5mM pH 6.8, sodium dodecyl sulfate (SDS) 2.5%, glycerol 10%, bromophenol blue 0,0025%
- SCID mice
- SDS Running buffer: Tris-HCl 50mM, glycine 384mM, sodium dodecyl sulfate (SDS) 0,1%
- Slides (Bio Optica, Milan, Italy)
- Syringes U-100, 29G (Thermo-Fisher Scientific, Waltham, MA, USA)
- T25 Flask (Sarstedt, Nümbrecht, Germany)
- Thp-1 cells, a cell line of activated monocytes
- Transfer buffer 1X: Tris-HCl 25mM, glycine 192mM, methanol 20%, pH 8.3
- Tricaine (Sigma-Aldrich Co., St Louis, MO, USA)
- trypsin-EDTA solution (0.5g/L porcine trypsin and 0.2g/L EDTA, Sigma-Aldrich Co., St Louis, MO, USA)

- Vybrant™ Dil or DiD Cell-Labeling Solution (Thermo Fisher Scientific, Waltham, MA, USA)
- Zebrafish embryos
- Zebrafish embryos of the transgenic line Tg(fli1:EGFP)
- Zebrafish embryos of the transgenic line Tg(mpeg1:mCherry)

Procedures

3.1 Cells culture and count

Cells were defrosted warming the cryovial at 37°C, then 5mL of culture medium was added to cells to eliminate DMSO which is toxic for cells, and cells were centrifuged for 5 minutes at 400 rcf. Later, the supernatant was removed, and cells were resuspended with the culture medium (RPMI-1640 medium) in a T25 Flask. Cells were maintained at 37°C and with a percentage of CO₂ corresponding to 5% and split every 3-4 days.

To count cells, the trypan blue exclusion assay was used; cells were diluted 1:1 v/v with trypan blue (TB) and counted with the Bürker chamber. In detail, the Bürker chamber is engraved with a laser-etched grid of perpendicular lines; the area bounded by the lines (quadrants) and the depth of the chamber are both known. By observing three quadrants of the grid, it is, therefore, possible to count the number of cells per mL of culture medium in accordance with the following formula:

$$Quadrant1 + Quadrant2 + Quadrant3 \times (dilutionwithTB) \times 10,000(conversionfactor) = cells/mL$$

Thp-1 cells were differentiated to macrophages incubating cells with 100ng/mL of PMA for 72h.

3.2 Production of the targeting mechanism

The design of the scFv takes the cue from the VH and VL regions of MOR208 (Patent n°: US 2014/0227277 A1), also known as Tafasitamab, an Fc-modified, humanized, anti-CD19 antibody. The monoclonal cell line transfected with the vector pcDNA3.1/Hygro+ coding for the targeting molecule (scFv of MOR208 linked to a human-Fc) has been cultured in the CELLLine™ Device bioreactor (BD Biosciences), to maximize production. The culture started by adding ~15x10⁶ cells to the cultivation chamber of the bioreactor (ExpiCHO™ Expression Medium). Twice a week the supernatant

containing the high concentration of targeting molecule produced by cells has been collected from the cultivation chamber and replaced with fresh cells. The medium of the nutrient chamber has been changed every 2 weeks. The collected supernatant has been centrifuged at 1500g for 20 minutes to remove any debris and the resulting sample was stored at -20°C. Once obtained a considerable number of collected supernatants, the targeting molecule has been purified by protein A affinity chromatography. Finally, the fractions containing the purified targeting molecule have been dialyzed O/N in PBS at 4°C. The final concentration of the targeting molecule after dialysis has been quantified by absorbance assay at 280nm using a spectrophotometer (Eppendorf BioPhotometer Plus).

3.3 Production of PLGA-PVA nanoparticles

PLGA-PVA-NPs were produced in our laboratory following Vasir and Labhasetwar protocol [149]. Firstly was prepared the polymer solution, and 30 mg of PLGA were dissolved in 1 mL of chloroform in a 5-mL glass vial with magnetic stirring. During this process, the solution for the core of NPs was prepared, and BSA-FITC or drugs were mixed in Tris-EDTA buffer. Finally, the PVA solution was set out; 0.2 g of PVA (m.w. 30,000-70,000) were sprinkled slowly over 10 mL of cold Tris-EDTA buffer, centrifuged at 1000 rpm for 10 min at 4°C, and then 10 µL of chloroform were added to saturate the PVA solution.

The solution for the core was added to the polymer solution in two aliquots of 100 µL each, vortexing for 1 min after each addition, and sonicated. This primary emulsion was added in two portions to 6 mL of PVA solution, vortexing for 1 min after each addition. The resulting emulsion was stirred overnight (at RT) to allow chloroform to evaporate. NPs were recovered by ultracentrifugation at 110,000g for 20 min at 4°C and the pellet was resuspended in 5 mL of Tris-EDTA buffer. The sample was washed again and resuspended in H₂O MilliQ filtered 0.2µm.

3.4 Characterization of nanodevices

3.4.1 Dynamic Light Scattering (DLS)

NBs and NPs (5µL) were diluted in 995µL of H₂O MilliQ filtered 0.2µm and then analyzed through the Dynamic Light Scattering (DLS); the analysis provided information about the charge and size of nanoparticles.

3.4.2 Transmission Electron Microscopy (TEM)

NBs and NPs (10 μ L) were centrifuged for 5 minutes at 5000 rcf and resuspended in 10 μ L of H₂O MilliQ filtered 0.2 μ m. NPs have been diluted 1:1 v/v with H₂O MilliQ filtered 0.2 μ m and then a drop of the sample has been deposited on a carbon screen coated by copper; after evaporation of the excess water, the analysis was performed.

3.4.3 Enzyme-linked immunosorbent assay (ELISA)

A sandwich ELISA was performed by coating a human anti-HSA antibody (final concentration 1:8000 in a final volume of 100 μ L/wells) on the ELISA plate, overnight (O/N) at 4°C. The unbound sites were blocked by incubation with milk 2% in PBS 1X for 1 hour at room temperature (RT). Then, wells were washed three times with PBS 1X added with Tween 0,1% and three times with PBS 1X. NPs (0.1 and 1 μ L/well) were added and incubated for 1 hour at RT. After washes, to reveal the presence of HSA-coating, a biotin-conjugated anti-HSA (final concentration 1:4000) secondary antibody was added for 1 hour RT. To reveal the secondary antibody, the AP-conjugated streptavidin (final concentration 1:2000) was incubated for 30 minutes. On the other hand, to reveal the presence of the anti-CD19 scFv-Fc, an AP-conjugated anti-human secondary antibody (final concentration 1:5000) was added for 1 hour at RT. After washes, the alkaline phosphatase substrate pNPP was added (1mg/ mL) to glycine buffer in order to develop the reaction. The optical density (OD) was read at 405nm with ELISA Reader TECAN Infinite M200.

3.4.4 Western Blot of NPs

30 μ L of NPs were centrifuged at 5000 rcf for 5 minutes. After removing the supernatant, NPs were resuspended in 15 μ L of sample buffer 1X and boiled for up to 30 minutes. The anti-CD19 scFv-Fc (500ng) has been diluted in sample buffer 1X and then boiled for the last 5 minutes. Until samples reached the running gel, the run has been performed in the running buffer at 15mA and then increased to 18mA. The separated proteins have been transferred to a nitrocellulose membrane by western blotting in the transfer buffer. Afterward, the membrane has been blocked with milk 2% in PBS 1X for 1 hour.

To reveal the presence of HSA-coating the membrane was incubated with goat anti-HSA antibody biotin-conjugated (1:4000) for 1 hour at RT; after washes, it was incubated with AP-conjugated streptavidin (final concentration 1:6000) for 30 minutes

at RT. The membrane has been developed with 5-Bromo-4-Chloro-3-Indo-yl-phosphate (BCIP, final concentration 0.3mg/mL) and Nitro Blue Tetrazolium (NBT, final concentration 0,6mg/mL) in AP buffer.

3.4.5 SDS-PAGE and Western Blot of scFv-Fc anti-CD19

20 μ L of supernatant of CHO cells producing the scFv-Fc, unbound material and purified scFv-Fc anti-CD19 (300ng) has been diluted in sample buffer 1X and then boiled for the last 5 minutes. Until samples reached the running gel, the run has been performed in the running buffer at 15mA and then increased to 18mA. For the SDS-PAGE analysis, the gel was stained in Coomassie Blue, while for the Western Blot analysis, the separated proteins have been transferred to a nitrocellulose membrane by western blotting in the transfer buffer. Afterward, the membrane has been blocked with milk 2% in PBS 1X for 1 hour. The membrane has been incubated with anti-SV₅ antibody (final concentration 1:2000) in milk 2% for 1 hour at RT. After three washes with PBS 1X, the membrane was incubated with the goat anti-mouse AP-conjugated secondary antibody (final concentration 1:5000) in milk 2% for 1 hour at RT. The membrane has been developed with 5-Bromo-4-Chloro-3-Indo-yl-phosphate (BCIP, final concentration 0.3mg/mL) and Nitro Blue Tetrazolium (NBT, final concentration 0,6mg/mL) in AP buffer.

3.4.6 Red blood cells lysis

NPs were diluted in CFD 1:50, 1:100, 1:200, and 1:400 (v/v) in a final volume of 200 μ L, and incubated with 50 μ L of EA (1%) for 30 minutes at 37°C under shaking (800rpm). The positive control is represented by EA diluted in H₂O, while the negative control is represented by EA diluted in CFD. After, samples were diluted with 1mL of PBS-EDTA and centrifuged at 12,000 rpm for 1 minute. The optical density (OD) of the supernatant (200 μ L) was read at 415nm with ELISA Reader TECAN Infinite M200, and values normalized as follows:

$$Lysis(\%) = \frac{Absorbance_{(sample)} - Absorbance_{(CTRL-)}}{Absorbance_{(CTRL+)} - Absorbance_{(CTRL-)}}$$

3.4.7 Clotting test

NBs and NPs (4 μ L/well), and NHP (80 μ L/well) have been seeded in a 96 wells plate. To assess the clotting capacity of the nano-devices, CaCl₂ 20mM (80 μ L) was added to initiate the clotting reaction. The eventual coagulation causes an increase in the turbidity of the well, which has been read at 405nm every 2 minutes for 70 minutes with ELISA Reader TECAN Infinite M200.

3.4.8 CH50 screening assay

NHS (100 μ L) and NBs or NPs (8 μ L) were incubated for 2 hours at 37°C under shaking (800 rpm). Then samples were centrifuged for 5 minutes at 5000 rcf and the supernatant was recovered. This latter was diluted 1:50, 1:100, 1:200, and 1:400 in CFD in a final volume of 200 μ L. After, 50 μ L of EA 1% was added. It was also set up total lysis (50 μ L of EA 1% in 200 μ L of H₂O) and a blank (50 μ L of EA 1% in 200 μ L of CFD, in which EA do not lyse) controls. Following the incubation for 30 minutes at 37°C under shaking (800 rpm), the lysis reaction was stopped with 1mL of PBS-EDTA 10mM. Samples were centrifuged for 1 minute at 12000 rcf to settle the EA. Then the OD of the supernatant was read at 415nm, which is the wavelength of absorption of the hemoglobin. It was calculated the percentage of lysis and then the CH50 (hemolytic complement 50) that provides the number of hemolytic units needed to have 50% lysis of EA. Specifically, lower CH50 values than a reference serum indicate fewer hemolytic units present and thus that the complement system has been activated.

3.5 MTT viability assay

Bjab or Nalm-6 cells (200,000/200 μ L of culture medium) were incubated for 48 hours at 37°C under shaking (800 rpm) with free drugs (1 μ M of docetaxel, doxorubicin, and idarubicin), or NPs (2 μ L for NP0, 1 μ M of encapsulated drug for NP3, NP4 and NP5). Then cells were centrifuged for 5 minutes at 400 rcf and the supernatant was removed; cells were resuspended in 200 μ L of clear culture medium. Later, 20 μ L of MTT has been added and samples were incubated for 4 hours at 37°C under shaking (800 rpm). Afterward, samples were centrifuged for 3 minutes at 20,000 rcf in order to precipitate all the formazan crystals. The supernatant has been discarded and the deposited crystals have been solubilized in 200 μ L of DMSO. The OD was measured at a wavelength of 570 nm ELISA Reader TECAN Infinite M200.

3.6 Flow cytometric analysis

3.6.1 Binding of anti-CD19 scFv-Fc on Bjab or Nalm-6 cells

Cells (250,000) were incubated with scFv-Fc (final concentration 10ng/ μ L) or with controls (anti-C5 antibody, final concentration 5ng/ μ L or rituximab, final concentration 5ng/ μ L) at 37°C for 1 hour in PBS 1X added with 2% BSA, CaCl₂ and MgCl₂ under shaking; then, three washes were performed to eliminate the excess of primary antibody and cells were incubated with the secondary anti-human antibody (dilution 1:200) conjugated with AlexaFluor, at 37°C for 1 hour under shaking. In the end, cells were washed to remove the excess antibody and fixed in 1% PFA diluted in PBS 1X added with 2% BSA, CaCl₂, and MgCl₂. The binding on the surface of cells was evaluated by flow cytometric analysis which was performed by Attune® NxT Acoustic Focusing flow cytometer (Thermo Fisher Scientific, Waltham, MA, USA), acquiring 10,000 events; data were analyzed with Attune NxT Software.

3.6.2 Binding and internalization of nano-devices in cells

For NBs or NPs binding/internalization studies, 250,000 Bjab or Nalm-6 were centrifuged at 400 rcf for 5 minutes and resuspended in 500 μ L of culture medium. Bjab, Nalm-6, or 100,000 differentiated Thp-1 were incubated at 37°C for different periods of time (15 minutes and 4 hours for NBs and 1 hour for NPs) with increasing amounts (2 μ L for NBs and 1, 2, and 4 μ L for NPs) of NB0 and NB2 or NP1 and NP0 under shaking (800 rpm). At the end of incubation, differentiated-Thp-1 cells were incubated for 5 minutes with the trypsin-EDTA solution and then, similarly to Bjab and Nalm-6 cells, were washed twice and resuspended with 1% PFA diluted in PBS 1X added with 2% of BSA, CaCl₂, and MgCl₂. The binding/internalization on the surface of cells was evaluated by flow cytometric analysis which was performed by Attune® NxT Acoustic Focusing flow cytometer (Thermo Fisher Scientific, Waltham, MA, USA), acquiring 10,000 events; data were analyzed with Attune NxT Software.

3.7 Immunofluorescence analysis

3.7.1 Binding of anti-CD19 scFv-Fc on Bjab or Nalm-6 cells

Cells (250,000) were incubated with anti-CD19 scFv-Fc (final concentration 10ng/ μ L) or with controls (anti-C5 antibody or rituximab, final concentration 5ng/ μ L) at 37°C for

1 hour in PBS 1X added with 2% BSA, CaCl₂ and MgCl₂ under shacking (800 rpm); then, three washes were performed, and cells were incubated with the secondary anti-human antibody conjugated with AlexaFluor-488 (1:200), at 37°C for 1 hour under shacking (800 rpm). In the end, cells were washed and fixed in 1% PFA diluted in PBS 1X added with 2% of BSA, CaCl₂, and MgCl₂.

Cells were then cytocentrifuged at 400 rcf for 5 minutes on a slide. The nuclei were stained with DAPI (1:200) for 5 minutes; the excess of DAPI was eliminated by 2 washes with PBS 1X. Slides were covered with a mounting medium and a coverslip. Slides were finally analyzed using a fluorescence microscope Nikon Eclipse Ti-E live cell imaging system equipped with a Nikon DS-Qi2 camera and stage incubation system able to control temperature, humidity, and percentage of CO₂. Images were analyzed using Image-J software.

3.7.2 Binding and internalization of nano-devices in cells

For NBs or NPs binding/internalization studies, 250,000 Bjab or Nalm-6 were centrifuged at 400 rcf for 5 minutes and resuspended in 500µL of culture medium. Bjab, Nalm-6, or 100,000 differentiated-Thp-1 were incubated at 37°C for 1 hour with 2µL of targeted or untargeted nano-devices (NB0, NB2, NP1, and NP2) under shacking (800 rpm). At the end of incubation, cells were washed twice and the nuclei were stained with DAPI (1:200) for 5 minutes, while membranes with Vybrant™ Dil (1:100). Cells were washed twice with PBS 1X and then cytocentrifuged at 400 rcf for 5 minutes on a slide. Slides were covered with a mounting medium and a coverslip. Slides were finally analyzed using a confocal microscope Nikon Eclipse C1si system equipped with a Nikon DS-Qi2 camera. Images were analyzed using Image-J software.

3.7.3 Ex vivo immunofluorescence on organs slices

Explanted organs were conserved at -80°C after embedding in the Killik solution; then, they were cut through the cryostat with a section thickness of 14-16µm. Sections were stored at -20°C. Liver and tumor mass sections were fixed in PFA 4% and rehydrated in PSB 1X for 5 minutes at room temperature. For what concerns slices of liver, they were incubated with 50µl of blocking solution for 30 minutes at room temperature. Then, the blocking solution was removed, and slices were incubated with an anti-mouse CD68 antibody (1:50) at 37°C for 1 h. After, slices were

washed and incubated with the secondary TRITC-labeled antibody (1:200), at 37°C for 1h. All liver and tumor mass sections were stained with DAPI (1:200) for 5 minutes, washed, and covered with a mounting medium and a coverslip; organs were analyzed using a fluorescence microscope Nikon Eclipse Ti-E live cell imaging system equipped with a Nikon DS-Qi2 camera and stage incubation system able to control temperature, humidity, and percentage of CO₂. Co-localization and tumor-mass images were analyzed using Image-J software.

3.8 *In vivo* experiments on zebrafish embryos

All experimental procedures involving animals were done due to the Ministerial Approval 04086.N.SGL.

Zebrafish eggs were placed in E3 Medium 1X supplemented with methylene blue 0.5%, incubated at 28°C, and 24 hours after fertilization (hpf) the eggs were manually decorated. Later, embryos were placed in E3 Medium 1X supplemented with phenylthiourea (PTU, final concentration 0.2mM) to inhibit the production of melanin.

3.8.1 NPs biodistribution studies

NPs biodistribution studies were performed in healthy and tumor-bearing embryos, by injecting NPs (4.6nL/embryo) in the duct of Cuvier of anesthetized embryos (tricaine final concentration 0.02%) using capillary glasses (Figure 3.1) and a Nanoject II Auto-Nanoliter Injector (Drummond Scientific Co., Broomall, PA, USA).

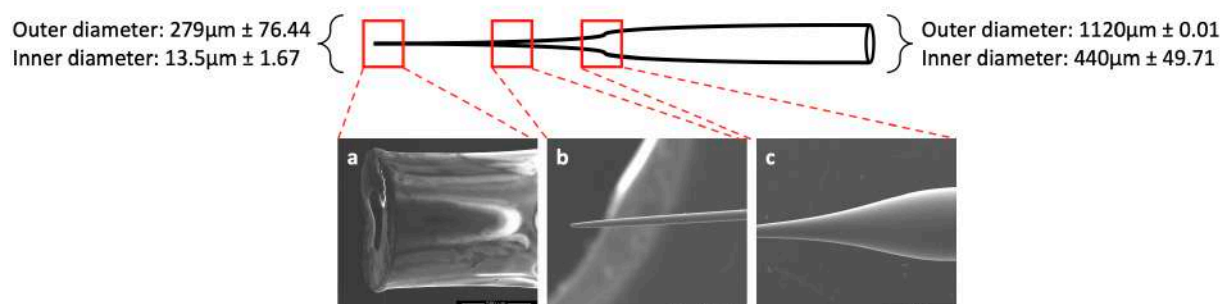


Figure 3.1: Capillary glasses. (a), (b), and (c) represents three portions of the capillary glasses analyzed through SEM microscopy in collaboration with the group of Prof. Turco (University of Trieste).

The whole process was conducted using a SteREO Microscope Discovery.V8 (Zeiss, Oberkochen, Germany, UE). At 24 hours post-injection (hpi) the biodistribution of the

NPs was evaluated using the fluorescence microscope Nikon Eclipse Ti-E live system; then, images were analyzed with Image-J software.

3.8.2 Xenograft models

48 hpf embryos were anesthetized using tricaine (final concentration 0.02%) and placed on agarose plates and the excess water was removed to facilitate injection. Nalm-6 cells were previously labeled with Fast DiD or calcein-AM (maximum excitation/emission 577/590nm) for 10 minutes (5 μ L of Fast DiD in 2mL of PBS 1X for 1x10⁶ cells, or 4 μ L of calcein-AM in 1mL of PBS 1X for 1x10⁶ cells). ~500cells/embryo were injected in a final volume of 4.6nL (final concentration 0.1cell/ μ L) using Nanoject II Auto-Nanoliter Injector (Drummond Scientific Co., Broomall, PA, USA). The localized model was set up by injecting cells in the perivitelline space, while the diffused ones by injecting cells in the duct of Cuvier. The whole process was conducted using a SteREO Microscope Discovery.V8 (Zeiss, Oberkochen, Germany, UE). After cell injection, the embryos were kept at 30°C, and evaluated using the fluorescence microscope Nikon Eclipse Ti-E live system. Images were analyzed with Image-J software.

3.9 In vivo experiments on mice

All the experimental procedures involving animals were done in compliance with the guidelines of the European and the Italian laws and were approved by the Italian Ministry of Health as well as by the Administration of the University Animal House (Prot. 42/2012).

3.9.1 Evaluation of the amount of cyanine5.5 bound to NBs

The amount of Cy5.5 bound to NPs was evaluated through spectrophotometry (adsorbance at 675nm). According to the Beer-Lambert law, the concentration of Cy5.5 was quantified:

$$A = \epsilon cl$$

where A is the obtained absorbance value, ϵ is the molar attenuation coefficient of Cy5.5 (corresponding to 250,000), c is the molar concentration of the fluorophore and l is the path length (1 cm) of the cuvette.

3.9.2 Assessment of a localized B-cell malignancy

A localized B-cell malignancy model was developed on the basis of a previous work published by our laboratory [44] injecting 10^7 MEC1 cells subcutaneously (s.c.) in the flank of SCID mice after treatment with cyclophosphamide (200mg/kg, 24 hours before). In 3-4 weeks, animals developed a visible tumor mass whose volume was measured by caliper every two/three days and quantified as follows:

$$Volume = D \times d^2 \times \frac{\pi}{6}$$

where D and d are the longer and the shorter diameters of the tumor mass, respectively.

3.9.3 NBs biodistribution studies

Biodistribution studies were performed in healthy and tumor-bearing mice. Tumor-bearing mice were developed as described in paragraph 3.7.2 and biodistribution studies were performed when the tumor mass reached the volume of 300mg mice were anesthetized, and their abdomen was epilated to avoid the possible scattering owed by the fur; mice were arranged supine in the chamber of the IVIS Lumina (PerkinElmer, Milan, Italy) machine. The parameters of the device such as exposition, focus, and resolution were set, and a pre-scan image was acquired to remove the mice's background. Then, mice were brought out of the instrument and intravenously injected with 0.3nmole of Cy5.5 bound to NBs. Mice were analyzed immediately after injection and after 24, 48, or 72 hours. At the end of the analysis, mice were sacrificed, organs explanted and analyzed by IVIS. After that, organs were embedded in the Killik compound and stored at -80° C.

3.9.4 Evaluation of the NBs therapeutic effect

A localized model of B-cell malignancy was induced with Bjab cells highly expressing miRNA-17 and with MEC1 poorly expressing miRNA-17 in SCID mice, as previously described (paragraph 3.7.2). When tumor mass reached the volume of 300mg or 500mg, mice were injected intraperitoneally (ip) with 37.5 μ L (corresponding to 30 μ g of AntagomiR-17) of targeted or untargeted NPs five times every two days. Every two days, the volume of the tumor mass was measured by caliper and when it reached

20% of mouse weight, mice were sacrificed. Then, organs were explanted embedded in the Killik compound, and stored at -80° C.

4. Results and discussion

4.1 Burkitt Lymphoma and chitosan nanobubbles

As mentioned before, BL is a rare, aggressive NHL that accounts for 1-2% of all cases of NHL in the general population. It was the first human tumor associated with a virus, one of the first tumors presenting a chromosomal translocation able to activate an oncogene, and the first lymphoma associated with HIV infection. Indeed, the three main types of BL are endemic, sporadic, and immunodeficiency-related [150]. All these features make BL an ideal candidate to develop a therapeutic nano-platform prone to analyzing the miRNA-17~92 cluster. This is a cluster of microRNAs involved in different tumors including B-cell malignancies. Particularly, among the miRNAs belonging to the miRNA-17~92 cluster, miRNA-17 is one that targets the largest number of genes and it is able to control their expression with opposite functions, such as promoting or suppressing cell cycle progression. In detail, miRNA-17 up-regulation entails the inhibition of some oncosuppressor genes leading to an augmented uncontrolled proliferation of B-cells [137]. Our group, in collaboration with the group of Dr. Riccardo Bomben (C.R.O. Aviano), designed a specific oligonucleotide (AntagomiR-17) able to pair and defeat endogenous miRNA-17. The administration of free-AntagomiR-17 was demonstrated to reduce miRNA-17 expression and consequently the proliferation of Chronic Lymphocytic Leukemia (CLL)-like MEC1 cells both *in vitro* and *in vivo*. In detail, *in vitro* studies demonstrated that Mec-1 cells, treated with AntagomiR-17, showed a significant reduction in cell rate proliferation, in comparison to the control. Moreover, when injected *in vivo* directly into a B-cell tumor mass AntagomiR-17 dramatically reduced tumor growth and increased mice survival. This effect, already relevant after the first week of therapy, was maintained until the end of the treatment leading to the complete regression of the mass in 20% of cases, and a single injection of AntagomiR-17 was sufficient to significantly reduce tumor growth for at least one week after treatment. Moreover, none of the mice showed signs of toxicity. This reported evidence suggested that miRNA-17 knock-down in CLL-like cells is sufficient to arrest cell proliferation both *in vitro* and *in vivo* [151]. This approach even though promising, own some limitations. In fact, AntagomiR-17 is a small oligonucleotide that, if injected intravenously, would be rapidly cleared from kidneys because of its small dimension. Therefore, the use of biocompatible chitosan-NBs targeted with anti-CD20 antibodies and loaded with

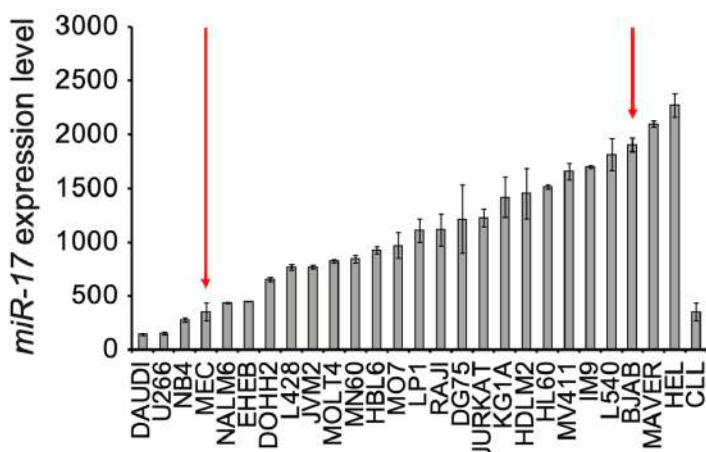


Figure 4.1: miRNA-17 expression in different cell lines. miRNA-17 expression varies among different cell lines and Bjab cells (BL's cell-line) demonstrated to own more than three times higher levels of miRNA-17 in comparison to MEC. (Supplementary of Dereani et al. 2014, modified)

AntagomiR-17 was proposed, in order to direct selectively the molecule in malignant B-cells and increase its therapeutic effect. In addition, since these promising results were obtained with a CLL-like cell line that, all things considered, possesses a very low level of miRNA-17, it was speculated that the best results can be obtained in BL (Bjab cells), which possesses a higher level of miRNA-17 (Figure 4.1, red arrows).

4.1.1 Nanobubbles

Since 1979, polymers are the most common materials for constructing nanoparticles (NPs)-based drug carriers because of their biocompatibility, biodegradability, safety, and *in vivo* stability [152]. Among polymers, chitosan is one of the most used to produce NPs with the aim to mediate selective targeting (also through the conjugation with molecules specific to target cells), induce a controlled release of the payload, protect the deliverable agents, extend the circulation time in the body of loaded drugs, load different types of molecules such as drugs, nucleic acids, and contrast agents. All these features allowed the use of chitosan for the production of nano-devices in this project. In particular, chitosan-Nanobubbles (NBs) were employed in this work, which differentiated from nanoparticles in the core structure. Indeed are gas-filled bubbles with dimensions in the sub-micron range [153].

4.1.1.1 Types of nanobubbles

NBs were kindly provided by Prof. Roberta Cavalli (University of Turin). In particular, 4 types of NBs were produced: NB0, NB1, NB2, and NB3, as shown in Figure 4.2. In detail, NBs consist of two parts: the external shell and the core. The NBs were generated by using chitosan (1.59mg/mL) which forms the shell of all the NBs which were then conjugated (NB2, and NB3) or not (NB0, and NB1) with rituximab (0.1mg/

mL) to allow their active targeting on the surface of CD20-expressing cells, such as some tumor B-cells. For what concerns the core, NBs were filled with different compounds: Coumarin 6 (C6, 0.05mg/mL), and Cyanine 5.5 (Cy5.5, 13mg/mL; NB0, and NB2) or AntagomiR-17 (0.8mg/mL, NB1, and NB3). Finally, to maintain their 3D structure, all NPs were filled with perfluoropentane (Figure 4.2).





| Name | NB0 | NB1 | NB2 | NB3 |
|---------------------|---|---|--|---|
| Structure |  |  |  |  |
| Polymers | chitosan | | | |
| Coating agent | none | | | |
| Monoclonal antibody | none | | anti-CD20 (0.1mg/mL) | |
| Encapsulated agent | Cy5.5 (13mg/mL) 6-coumarin (0.05mg/mL) | AntagomiR-17 (0.8mg/mL) | Cy5.5 (13mg/mL) 6-coumarin (0.05mg/mL) | AntagomiR-17 (0.8mg/mL) |

Figure 4.2: Nanobubbles (NBs) used for *in vitro* and *in vivo* studies. NB0 were composed of chitosan and filled with Cyanine5.5 (Cy5.5) and coumarin 6 (C6). NB1 derived from the encapsulation of AntagomiR-17 inside NB0. NB0 and NB1 conjugated with rituximab constituted NB2 and NB3, respectively. All the NPs contain Perfluoropentane (PFP), which is helpful to maintain their structure.

4.1.1.2 Shell and structure of nanobubbles

All the NB formulations were firstly characterized *in vitro*, showing round shapes, sizes lower than 400 nm and a positive surface charge (around +30 mV). The average diameter, polydispersity index (PDI) and zeta potential values of the different types of NBs are reported in Figure 4.3 (A). These data underline the fact that the incorporation of AntagomiR-17 in the NBs did not alter their structure and did not determine significant changes in their physicochemical parameters. Moreover, as shown in Figure 4.3 (B) NBs demonstrated to have a spherical shape.

The capacity of NBs to load and retain the AntagomiR-17 was tested by gel retardation assay, where a disappearance of the AntagomiR-17 band was detected when it is incorporated in NB1 and NB3 formulations (Figure 4.3, C). NB formulations showed good stability over time when stored at 4 °C for 6 months. Indeed, no size

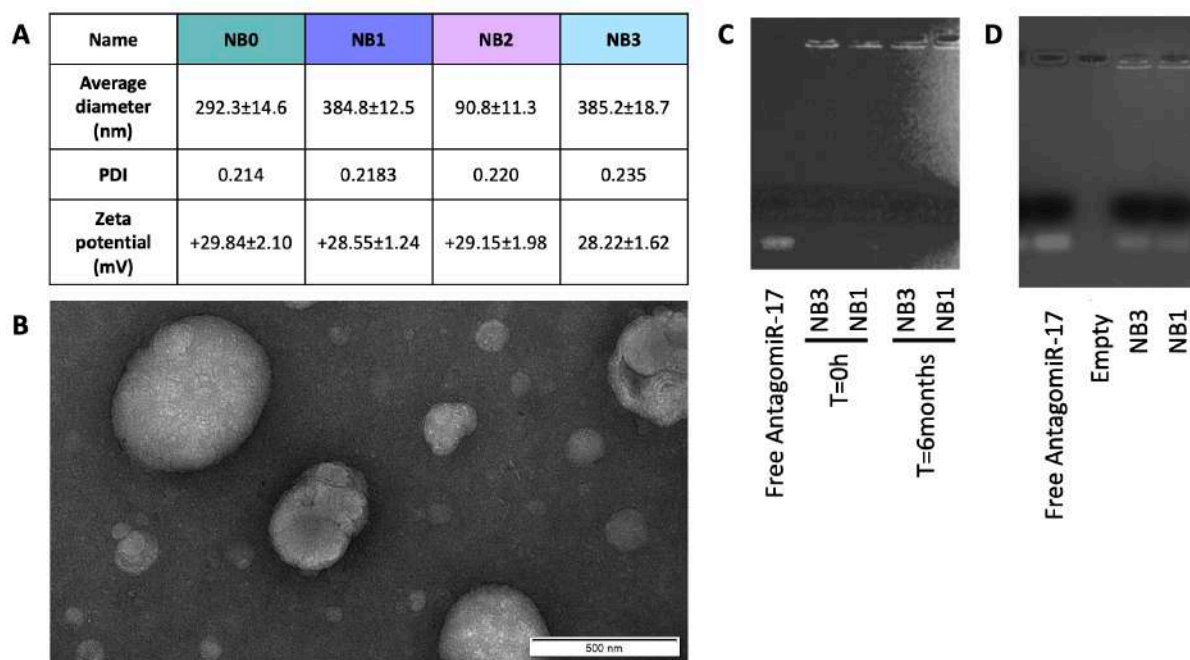


Figure 4.3: Nanobubbles characterization. (A) Physicochemical characteristics of NBs formulations. (B) TEM image of NB0 (scale bar 500 nm). (C) AntagomiR-17 incorporation in NBs and their stability over time. (D) *In vitro* release in simulated cytosol of AntagomiR-17 from AntagomiR-17 loaded nanobubbles (NB1 and NB3).

increase, zeta potential modification, or NB aggregation occurred. In addition, in collaboration with Prof. Roberta Cavalli, the *in vitro* stability of AntagomiR-17-loaded NBs was evaluated by gel retardation assay. Both the formulations NB1 and NB3 fully retained the AntagomiR-17, as shown in Figure 4.3 (C), confirming the physical stability up to 6 months. The *in vitro* release of AntagomiR-17 from the NB1 and NB3 was also evaluated in simulated cytosol, over time (Figure 4.3, D). Free AntagomiR-17 (2 μ g) migrated through the gel towards the positive pole and a band was visible on the gel. After only 6 hours of incubation, a band was observed for both the formulations, indicating that AntagomiR-17 can be released in the cell cytoplasm (Figure 4.3, D). To note, a low fluorescence signal is still visible in the wells, suggesting an incomplete release of AntagomiR-17 after 6 hours.

4.1.2 *In vitro* characterization of nanobubbles

Mammals have developed evolutionary defense mechanisms that provide immunity and resistance to invasive agents and their failure results in illness [154]. It is commonly thought that the first contact of nano-materials with the organism is through different components of the IS. However, intravenously injected nano-materials enter the bloodstream and they come into contact with blood cells (red cells,

white cells, and platelets), complement proteins, and plasma proteins [100]. In particular, the interaction with platelets begins a cascade of signals that eventually leads to the rift of hemostasis, with the activation of the coagulation cascade and the formation of blood clots, that partially or totally occlude the blood vessels by thrombi. These effects will depend not only on the size, charge, hydrophobicity, or type of cover but also on the intrinsic characteristics of the nanoparticles. On the other hand, the complement system (CS) has three known modes of activation: the classical, alternative, and lectin pathways, which differ both in their activation mechanisms and initial components [155]. Here, the surface charge plays an important role. It has been noted that charged nanoparticles are more apt to activate the complement than neutral counterparts, thus coating layers (i.e. with PEG) are helpful to partially neutralize the surface charge and reduce the inflammatory response by the release of anaphylatoxins (e.g., C3a and C5a), C3b and C5b–C9 lytic complex [156]. On these bases, it is important to understand if and how NPs interact with blood elements, to evaluate health risks, and assess their effective toxic potential, in both the blood and remote sites.

4.1.2.1 Interaction of nanobubbles with blood components

NBs were initially tested *in vitro* for clotting formation. In particular, a turbidity assay was performed (Figure 4.4, A, and B). Briefly, naked-NBs (NB0) were incubated in plasma and a solution containing Ca^{2+} was added, which triggers the coagulation

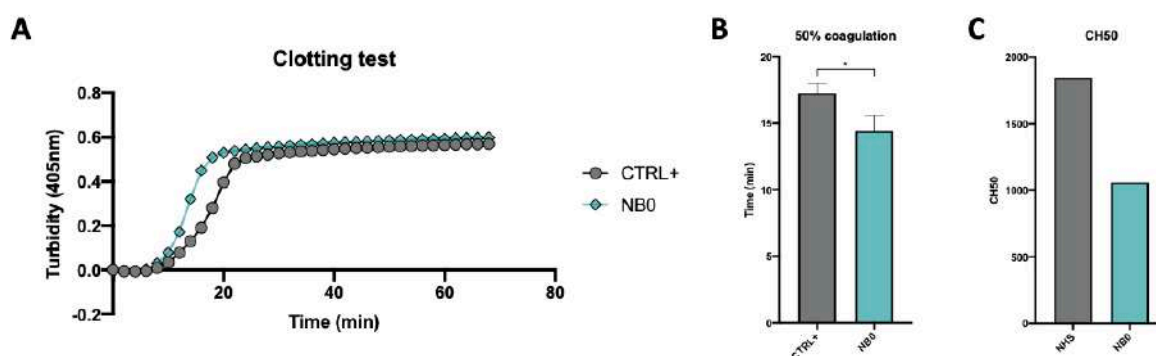


Figure 4.4: *In vitro* test of clotting formation and activation of classical pathway of the Complement. (A) Turbidity curve trend of NB0 in activated plasma during time, *in vitro* compared with simple activated plasma as control. **(B)** The half coagulation time extrapolated from the curve of trend data showed a potential NBs effect on coagulation system. **(C)** CH50 hemolytic activity was evaluated in NHS, as a control, and in the same NHS after 2 hours *in vitro* incubation with NB0. The large consumption of classical pathway, shows an important activation of the complement pathway. All data report as the mean \pm SD. Statistical significance has been assessed by unpaired Welch's test. $P \leq 0.05 = *$; $P \leq 0.01 = **$; $P \leq 0.001 = ***$; $P \leq 0.0001 = ****$.

process, and samples turbidity were analyzed during the time (Figure 4.4, A). This test demonstrated that NBs benefit from a very similar trend to that observed for simply activated plasma, used as control. However, the analysis of that data leads to a significant difference between half coagulation time of NPs and its control (Figure 4.4, B).

The activation of the CS was then investigated. In particular, the residual activity of the classical pathway was analyzed through a hemolytic assay (CH50). The CH50 assay relies on the ability of serum to lyse antibody-sensitized sheep erythrocytes through the activation of classical pathway proteins

[157]. This experiment demonstrated a reduction of the classical pathway activity, observable from the reduced lytic power of NHS after incubation with NB0; this could be due to the consumption of these proteins reacting against particles (Figure 4.4, C). The interactions of NBs with the blood coagulation system may influence the natural balance between pro- and anticoagulant pathways, and undesirable effects of nanoparticles on the coagulation system have to be monitored to avoid toxicities.

4.1.2.2 Binding and internalization of chitosan-NBs inside malignant B-cells

Over conventional treatments, nanomedicine for cancer therapy is advantageous because it has the potential to enable the preferential delivery of drugs to tumors through targeting ligands bound to nano-devices surfaces. In fact, the engineering of a targeting ligand onto NPs can result in the greater efficacy of the therapy and reduced side effects [158]. Among B-cells-related antigens, CD20 was the first molecule against whom monoclonal antibodies were developed and in particular, the anti-CD20 antibody, known as rituximab, was the first approved by the FDA in 1997 for the immunotherapy of B-cell malignancies. In detail, CD20 is a tetra-spanning membrane protein that is supposed to function as a B-cell Ca^{2+} channel subunit [159]. CD20 is expressed on B-cells from pre-B cells to the plasma-blast stage but not on early stem cells or on plasma cells allowing the restoration of the normal B-cell population after the end of the treatment. Additionally, CD20 is not secreted and its expression does not change in time. All these features render CD20 an outstanding target for immunotherapy against B-cells malignancies, as well as for the targeted approach based on the use of anti-CD20-labelled NBs.

The contribution of anti-CD20 antibodies, conjugated on the surface of NBs, to the binding and the internalization of nano-systems was evaluated by incubating NB0 and

NB2 with CD20-expressing cancer B cells (Bjab). At short-incubation-time (15 minutes), NB0 interacts with a higher number of cells than NB2 (86.0% vs 50.7%) but this difference was completely flattened at longer incubation times (4 hours, 91.3% vs 96.8%, Figure 4.5, A).

Conversely, among positive cells, the percentage of internalized NB2 at 15 minutes of incubation was higher than NB0 ($42 \pm 23.9\%$ vs $4 \pm 11.8\%$, $P < 0.05$), as suggested by NBs quantification through confocal microscopy (Figure 4.5 B and C).

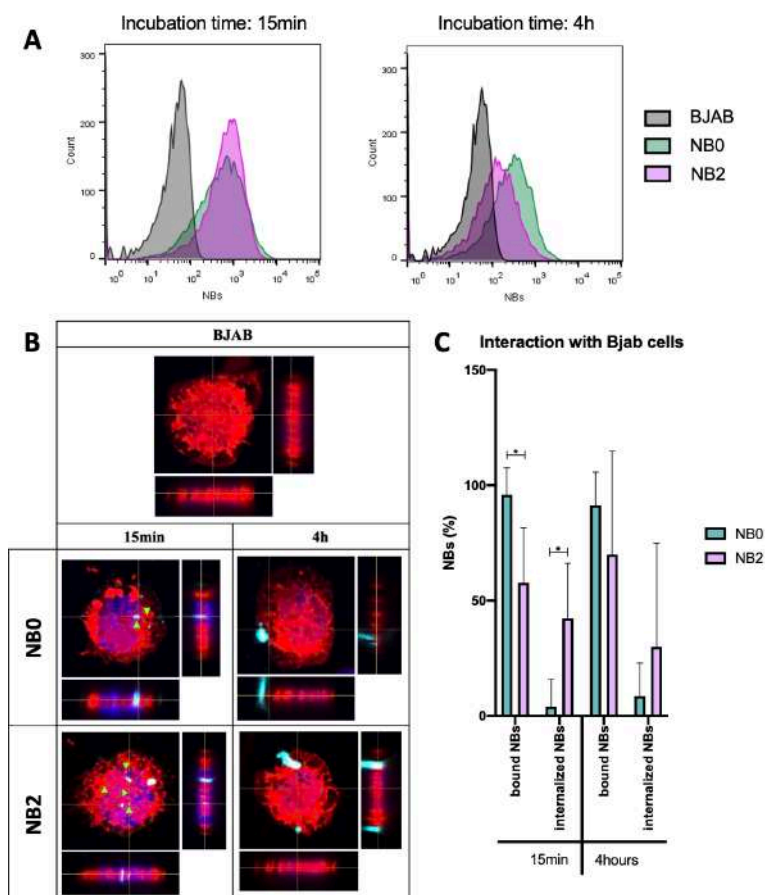


Figure 4.5: NBs bind and internalize in tumor B cells. (A) Cytofluorimetric analysis of Bjab cells incubated with Cy5.5-conjugated NBs at 37°C. (B) Analysis of NBs internalization by confocal microscopy. Cells membrane were labelled with Vybrant™ Dil (red), nuclei with DAPI (blue) and NBs with Cy5.5 (light blue). Green arrows highlight internalized particles. (C) Quantification of bound and internalized NBs in Bjab cells. Data are shown as mean \pm SD. * P-value < 0.05 . NB0: untargeted NBs; NB2: antiCD20-conjugated NBs.

4.1.2.3 *In vitro* effect on miRNA-17 levels

In collaboration with the group of Dr. Riccardo Bomben (C.R.O. Aviano), real-time-PCR assays were performed to evaluate the ratio of miRNA-17 after the incubation of Bjab cells with free AntagomiR-17 or NBs. As result, NB0 and NB2 did not affect miRNA-17 expression levels; on the contrary, AntagomiR-17-loaded NB1 and NB3 significantly decreased cytoplasmatic concentration of miRNA-17 (Figure 4.6, A), suggesting that encapsulated AntagomiR-17 is still active and released in the tumor cells. Moreover, the inability of NB0 and NB2 to reduce miRNA-17 levels suggest also that the level of miRNA-17 is modulated by encapsulated AntagomiR-17 and not by polymers/anti-CD20-mediated effect. In addition, NB3 were also analyzed in time, showing the best interfering effect after 48 hours of incubation with cells, while at 72

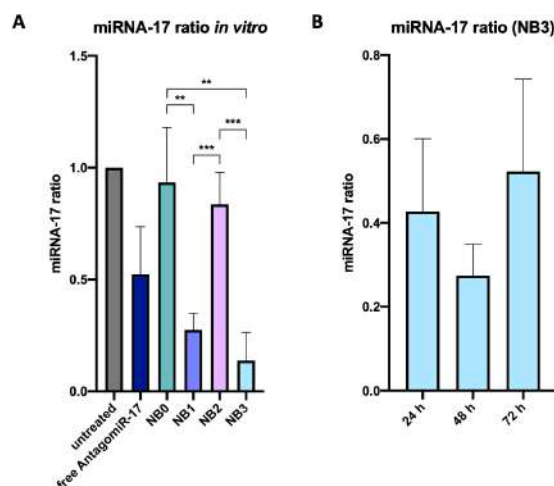


Figure 4.6: AntagomiR-17-loaded NBs reduce miRNA-17 levels in tumor B cells. (A) Analysis of miRNA-17 levels in Bjab cells incubated with free AntagomiR-17 or NBs. (B) Analysis of miRNA-17 levels in Bjab cells treated with NB3 for 24, 48 or 72 hours. NB0: empty untargeted NBs; NB1: AntagomiR-17-filled untargeted NBs; NB2: empty targeted NBs; NB3: AntagomiR-17-loaded targeted NBs. ** P-value <0.05; *** P-value <0.005.

hours the miRNA-17 expression started to be restored (Figure 4.6, B). These *in vitro* data demonstrated a general binding and internalization of all NBs into B cells, leading to the transport of AntagomiR-17 inside cells, with a consequent cytotoxic effect due to the down-regulation of miRNA-17 levels, putting the basis for *in vivo* studies.

4.1.3 *In vivo* characterization of chitosan nanobubbles

All data obtained *in vitro* highlight the potentiality of chitosan-NBs; therefore, *in vivo* tests are needed to evaluate NBs' behavior in a more complex system. In fact, many factors can influence therapeutic efficacy, including pharmacokinetics, which refers to the passage of drugs into the body, through it, and out of the body. The first step of pharmacokinetics is absorption, and when a drug is given intravenously its bioavailability is 100% because the active form of the drug is delivered immediately to the systemic circulation. The second step is represented by the distribution, which is important to determine drug efficacy and toxicity showing where the drug localizes inside the body. Finally, metabolism and elimination of the drug represent the last step, and since NBs' dimensions are prohibitive for renal clearance, these coincide in the liver. Therefore, biodistribution studies were performed to investigate the localization and the accumulation of NBs inside the body, and then therapeutic efficacy was confirmed *in vivo*.

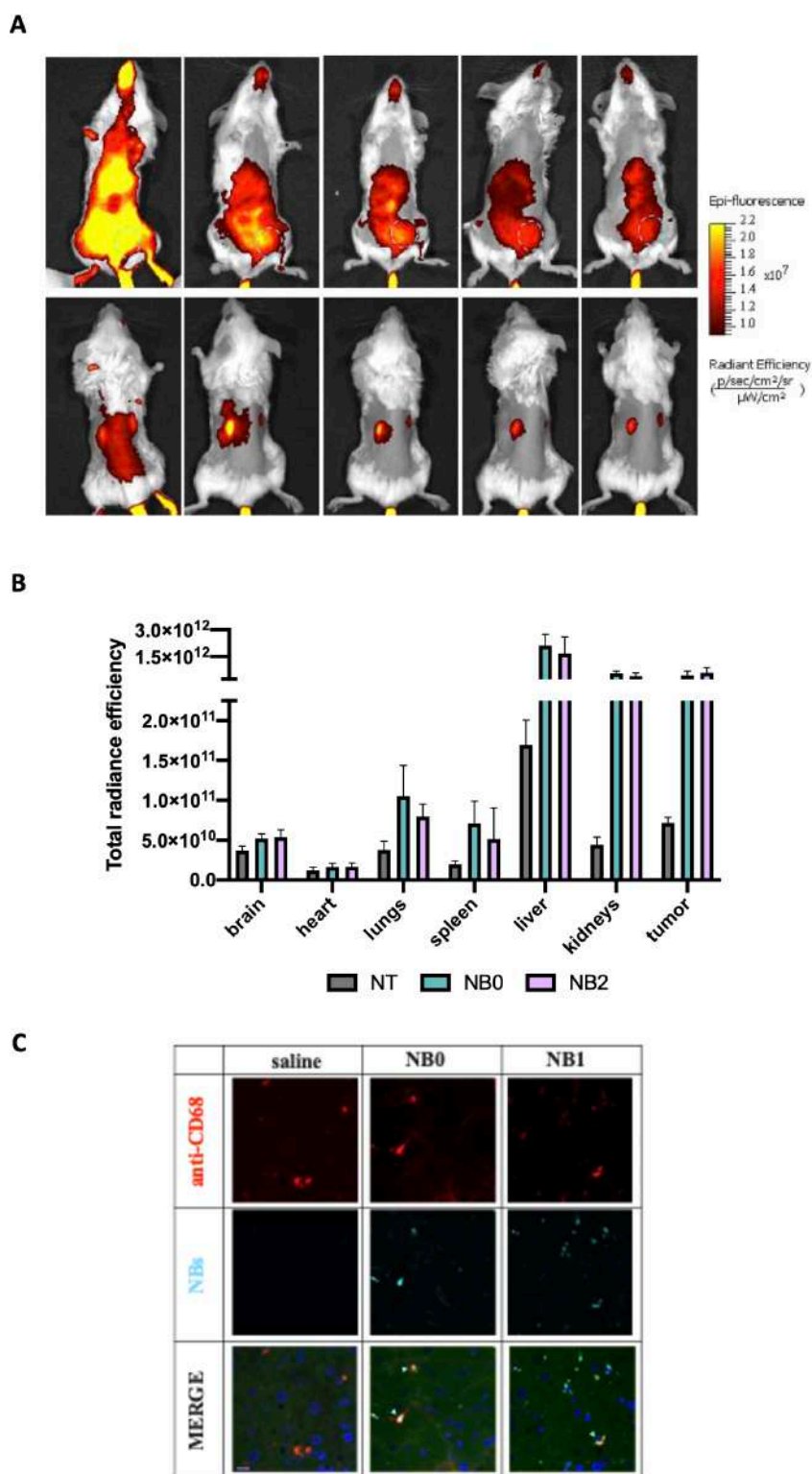


Figure 4.7: Analysis of NBs biodistribution in mice. Cy5.5-labeled NBs were injected i.v. in tumor-bearing mice. **(A)** *In vivo* distribution studies were performed for 96 hours showing NBs accumulation mainly in liver, tumor mass (from supine position-upper panel) and kidneys (from prone position-lower panel). **(B)** Data were confirmed ex vivo, analyzing NBs fluorescence in different organs at the end of the experiment. Data are showed as mean \pm SEM. ns: P-value >0.05 . NT: untreated mice; NB0: untargeted NBs; NB2: anti-CD20-conjugated NBs. **(C)** NBs elimination by the liver was also confirmed by immunofluorescence analysis. Macrophages were stained using anti-mouse CD68 and TRITC-conjugated secondary antibody (red fluorescence), cell nuclei by DAPI (blue fluorescence) and NBs by their near-infrared fluorescence (light blue); green fluorescence represents tissue autofluorescence. Samples were analyzed by confocal microscopy. Scale bar: 10 μm . Light blue arrows highlight NBs/macrophage co-localization.

4.1.3.1 Biodistribution studies

NBs biodistribution studies were made using In Vivo Imaging Instruments (IVIS), at the Centro di Riferimento Oncologico (C.R.O.) in Aviano. This is a pre-clinical non-invasive *in vivo* imaging system, which allows the study of biodistribution of labeled molecules. It is fast, and easy to perform, and it allows the evaluation of the same animal more than one time during experimentation. In fact, the same anesthetized animal can be evaluated at different time points avoiding the sacrifice that would be necessary to perform the same analysis just by *ex vivo* assays. A localized model of B-cell disorder was induced in mice, as previously described [158]. Bjab (2×10^6 cells) were injected in a flank of SCID mice and a tumor mass developed at the site of injection in 20-25 days. When the tumor mass reached an average volume of 250-300 mm³, 0.6 nmol of Cy5.5 conjugated to untargeted- and targeted-NBs (NB0 and NB2, respectively) were intravenously injected. Animals were shaved before acquisition to reduce the scattering of the signal from hair, and were analyzed (Figure 4.7, A) before the injection (background) and immediately after injection, and after 24, 48, 72, and 96 hours. Mice showed a peak of fluorescence in the abdomen (probably the liver and the intestine) and in the mouth immediately after the injection of NBs.

After 48 hours, this fluorescence signal drastically decreased, suggesting the elimination of the majority of NBs in this period. After 96 hours, mice were sacrificed, and organs were explanted and analyzed again by IVIS to have better accuracy. As shown in Figure 4.7 (B), NBs were not localized in the brain, heart, or in other organs of the Mononuclear Phagocytic System (MPS). Presumably, the macrophages of MPS were not able to phagocyte NB, which were eliminated through the liver-bile-intestine-excretion pathway, as demonstrated by the high fluorescence signal in the liver (Figure 4.7, A-upper panels) and confirmed by confocal microscopy on tissue sections (Figure 4.7, C).

In addition, biodistribution analysis also suggested an unexpected presence of NBs in the kidneys; fluorescence was revealed in these organs starting from 1-hour post-injection to the end of the observation (Figure 4.7, A-lower panels), and this was probably due to the positive charge of nano-devices (NB0: $+29.84 \pm 2.10$ and NB2: $+29.15 \pm 1.98$ mV), which induced their interaction with the negatively charged glomerular membrane of kidneys [160].

In vivo biodistribution studies also demonstrated the presence of NBs in the tumor mass, and their localization in this microenvironment was not mediated by a local presence of macrophages because these cells were absent in the tumor masses (data not shown). During *in vivo* biodistribution studies, a region of interest was selected to measure the amount of near-infrared fluorescence in the tumor mass over time. The presence of both NB0 and NB2 in the tumor mass was detected without a significant difference between particles (Figure 4.8, A).

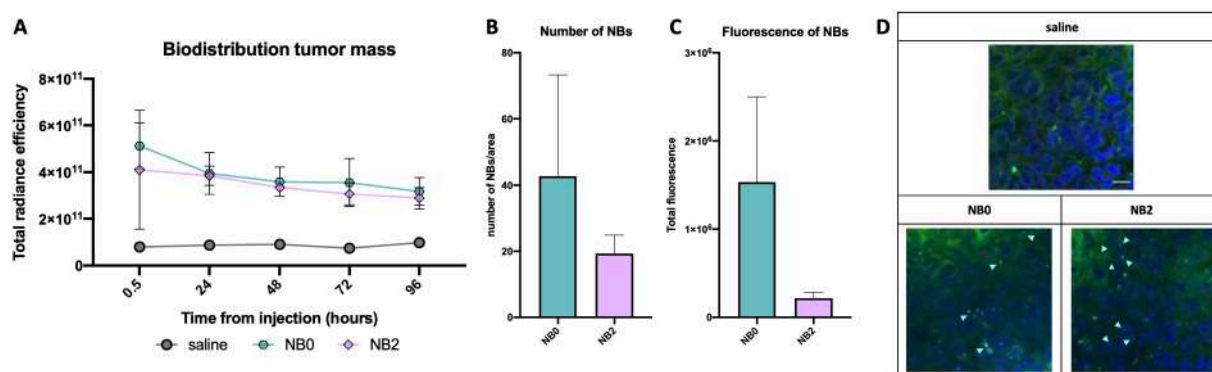


Figure 4.8: Targeted and untargeted NBs localized in the tumor mass. (A) During *in vivo* biodistribution studies, a region of interest was selected to measure the amount of near-infrared fluorescence in the tumor mass over time. Data are expressed as mean \pm SEM. (B) At the end of the study tumor section were analyzed by confocal microscopy. Cy5.5-labeled NBs (light blue) were visualized; nuclei were stained with DAPI (blue fluorescence); green fluorescence represents autofluorescence of tumor tissue. Scale bar: $10 \mu\text{m}$. (C) The number of NBs and (D) the amount of fluorescence were quantified and expressed as mean \pm SEM. NB0: untargeted NBs; NB2: antiCD20-conjugated NBs.

This was also confirmed by the *ex vivo* quantification of the fluorescence and the number of NBs in these samples after the acquisition of confocal microscopy images. Despite the absence of significant differences in terms of the number of NBs (Figure 4.8, B) and total fluorescence (Figure 4.8, C) in the analyzed area, microscopy images showed a different pattern of NBs in the tumor tissue: NB0 appeared as bigger clusters while NB2 were more scattered and smaller (Figure 4.8, D).

4.1.3.2 Therapeutic efficacy

To evaluate the therapeutic effect of AntagomiR-17-loaded NPs, a localized model of B-cell disorder was induced in three mice. When the tumor mass reached 300mg of weight, mice received four intratumorally injections (day 0, 3, 10, 16) of physiologic solution (untreated mice), AntagomiR-17 free (120 μ g) or loaded inside targeted-NBs (NB3). The dimension of the tumor mass was measured three times a week with a caliper to assess the effect mediated by AntagomiR-17 on tumor growth. Free AntagomiR-17, injected intratumorally with the same protocol previously tested [151], induced a significant reduction of miRNA-17 level *in vivo* (Figure 4.9, A), but despite these results, free AntagomiR-17 did not affect tumor growth (Figure 4.9, B).

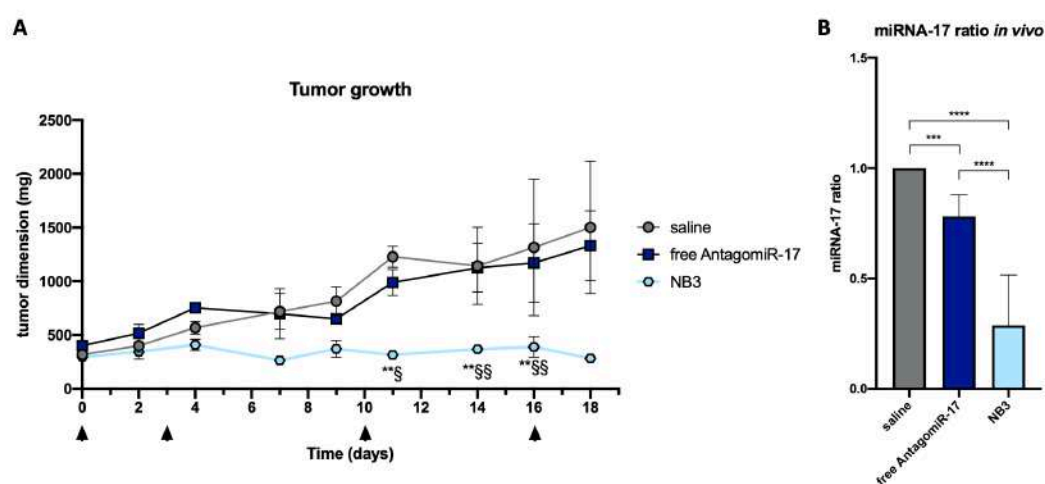


Figure 4.9: Local treatment with NB3 reduce miRNA-17 levels in tumor B-cells and inhibit tumor growth. Tumor-bearing mice received intratumoral injection of free AntagomiR-17 or AntagomiR-17-loaded targeted NBs (NB3). (A) Tumor mass dimension was measured during treatments. Data are showed as mean \pm SEM. NB3 vs saline: ** P-value <0.01; NB3 vs AntagomiR-17: § P-value <0.05; §§ P-value <0.005. (B) The expression of miRNA-17 was measured *ex vivo* by Real-Time PCR at the end of the study. Data are showed as mean \pm SD. n=3. **** P-value <0.0001.

On the other hand, AntagomiR-17-loaded NB3 strongly down-regulated miRNA-17 expression in the tumor mass after local repeated injections (Figure 4.9, A), inducing a complete arrest of tumor growth *in vivo*, particularly evident after the second injection and maintained during the treatment (Figure 4.9, B). Moreover, tumor-bearing animals were treated via intraperitoneal injections of NB1 or NB3 for 18 days to evaluate the strength of the targeting mechanism.

Animals received the nano platform three times per week, exploiting the fast accumulation of the NBs (Figure 4.8) and their pick of efficacy after 48 hours (Figure 4.6, B). The presence of the anti-CD20 antibody on the surface of the nano platform was demonstrated to be fundamental for the efficacy of AntagomiR-17-loaded nanoparticles. NB3 completely arrested tumor growth and all animals survived at the end of the study. On the contrary, NB1 (AntagomiR-17-loaded nanoparticles without a targeting agent) were ineffective, showing similar tumor growth with respect to saline-treated mice; all the animals treated with saline or NB1 have been sacrificed in less than 20 days because of the dimension of the tumor mass (Figure 4.10).

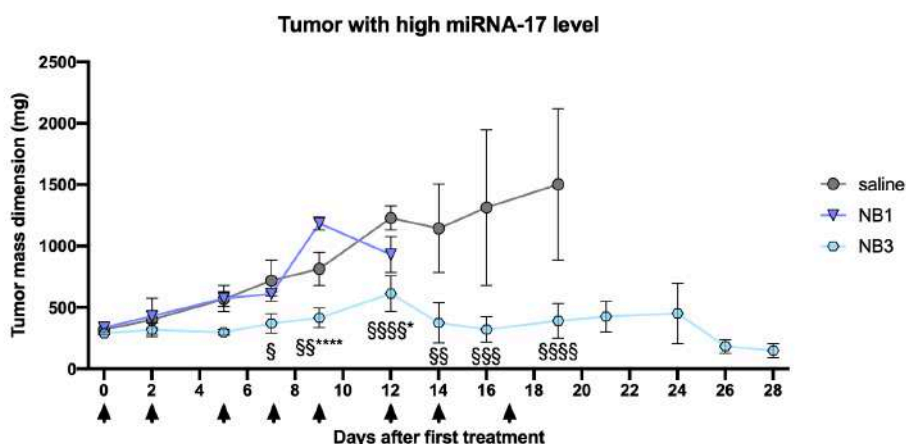


Figure 4.10: Anti-CD20 NB3 treatment decrease tumor mass neutralizing miRNA-17 activity. Human-mouse model developed injecting Bjab cells in SCID mice received i.p. injections (day 0, 2, 5, 7, 9, 12, 14, 17) of AntagomiR-17-loaded targeted (NB3) or untargeted NBs (NB1). Tumor mass was measured, and data are showed as mean \pm SEM. NB3 vs NB1: * P-value <0.05; **** P-value <0.0001; NB3 vs NT: §§ P-value <0.01; \$\$\$ P-value <0.001; \$\$\$\$ P-value <0.0001.

To demonstrate that the therapeutic effect of the targeted nano platform was dependent only on the presence of AntagomiR-17 and it was not induced by the anti-CD20 antibody or polymers, the *in vivo* experiments were repeated in a second human/mouse model of B-cell malignancy; animals were challenged with a specific population of Mec-1 cells, expressing low levels of miRNA-17. In this context, the

effect of NB3 was completely abolished and the development of the tumor mass was not different from saline-treated mice (Figure 4.11). Therefore, chitosan-based NBs developed in this study are demonstrated to represent a promising tool in the treatment of BL.

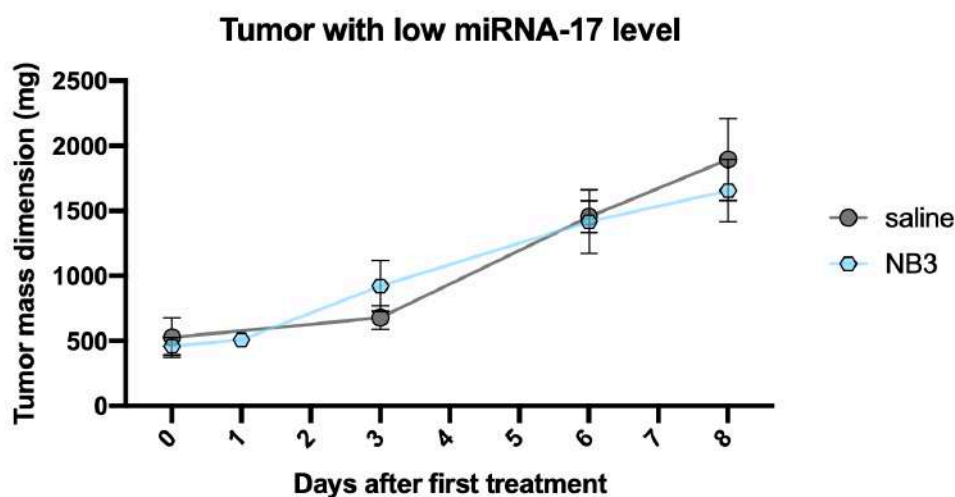


Figure 4.11: Anti-CD20 NB3 treatment in a low miRNA-17 expressing model. Human-mouse model developed injecting Mec-1 cells (expressing low levels of miRNA-17) in SCID mice received i.p. injections of AntagomiR-17-loaded targeted (NB3) or saline. Tumor mass was measured, and data are showed as mean \pm SEM.

Although the difference in the accumulation of untargeted and targeted NBs was not shown in biodistribution studies, the advantage of the targeting mechanism was particularly evident in the therapeutic efficacy studies; in fact, no therapeutic effect was described using untargeted NB loaded with AntagomiR-17, while the inhibition of tumor growth was clearly documented after repeated injection of targeted anti-CD20 NBs with AntagomiR-17, and the effect is dependent by the presence of the anti-CD20 but only for its targeting ability.

However, even though the potentiality of this nano platform there are some limitations. In particular, the anti-CD20 antibody employed in this study to label NBs resulted powerful and promising, but not being able to cover all B-cell malignancies. In particular, known, B-cell malignancies can be distinguished through the expression of characteristic surface antigens that reflect the developmental stages in which the pathology occurs. ALL, for example, originates from early-stage cells that do not possess the CD20 antigen, suggesting to employing another targeting mechanism able to target a wider class of pathologies. In addition, *in vitro* tests highlight NBs'

ability to stimulate the coagulation process, and their ability to induce CS activation. Moreover, the biodistribution of positive-charged chitosan-NBs resulted in a heightened accumulation in kidneys due to their charge. All these features suggest developing another nano platform able to overcome these limitations, characterized by different features such as a different targeting agent and a negative surface charge.

4.2 Acute Lymphoblastic Leukemia

ALL is the most common childhood malignancy, arising from the clonal expansion of transformed B-cell precursors [2, 21, 22]. A quarter of all cancers in patients under the age of 20 are represented by ALL and, while most cases happen in younger people, adult ALL patients are more challenging to treat and show a worse prognosis. ALL develop from the unregulated growth of clonal lymphoid cells, most commonly pre-B-cells (80%-85%), and recent studies demonstrated that cells became malignant before birth [12]. Fortunately, the 5-year survival rate has increased from under 50% in the second half of 1900 to nearly 85% in the 21st century [21]. Therefore, since immunotherapy and chemo-immunotherapy are demonstrated to be efficient but also related to high-risk characteristics, nanoparticles (NPs) represent an innovative choice to potentiate the effect of the drug and, at the same time, including the drug inside their core, to reduce side effects associated with the free drug. Moreover, these NPs can be equipped with a targeting mechanism able to deliver nano-structures specifically at the site of interest. As mentioned before, anti-CD20 antibodies result to be a valid targeting choice for B-cell malignancies, but unfortunately, in the specific case of ALL, the anti-CD20 is unhelpful. In fact, ALL originates from early stages B-cells that do not express the CD20 on their surface. Therefore there is a need to find another marker useful for this purpose, and this is represented by the CD19 antigen. In fact, it is expressed in nearly all B-cell leukemias and is rapidly internalized upon binding of an antibody [161], rendering this antigen an ideal candidate.

4.2.1 Nanoparticles

NPs owe their success in drug delivery to the possibility to employ materials with favorable features: biocompatibility and biodegradability. In fact, for a suitable outcome, after administration, polymers should be disaggregated into biocompatible molecules disposable via metabolic pathways [79]. Biodegradable polymers are both

based on natural materials including chitosan, alginate, gelatin, and albumin, and synthetic materials such as poly(lactide) (PLA), poly(lactide-co-glycolide) copolymers (PLGA), poly(ϵ -caprolactone) (PLC), and poly(amino acids) [76, 78].

As demonstrated here before, chitosan-NBs are proved to be a powerful tool in nanomedicine. In particular, chitosan-NBs are self-assembled in the presence of the drug, or miRNA-molecule, to be incorporated, and their degradation represents a vehicle in the release of nucleic acids into the cytosol. Moreover, our tests confirmed these characteristics and their safety, even if additional tests are needed to evaluate their behavior in the coagulation process and CS activation.

On the synthetic polymers counterpart, PLGA has been widely investigated to formulate biodegradable devices for sustained and targeted delivery of drugs, proteins, and nucleic acids. PLGA is a copolymer consisting of two different monomer units, poly(glycolic acid) (PGA) and poly(lactic acid) (PLA) which are linked together by ester linkages, and the result is a linear, amorphous aliphatic polyester product. Its success is particularly related to its continued drug release, compared to conventional devices. *In vivo*, the polymer undergoes degradation by hydrolysis forming the original monomers (i.e., lactic acid and glycolic acid). Thus, they are easily processed via metabolic pathways such as the Krebs cycle and removed as carbon dioxide and water, causing minimal systemic toxicity. The negative charge of the PLGA is also crucial in its activity because it strongly influences the interaction between NPs and cells [86]. Another synthetic and biocompatible polymer extensively studied is poly(vinyl alcohol) (PVA). PVA is frequently used as an emulsifier in the formulation of PLGA-NPs, due to its ability to form an interconnected structure with the PLGA, helping to achieve NPs relatively uniform and small [88]. Starting from these considerations, PLGA-PVA-NPs were investigated in this study as a substitute for chitosan-NBs.

4.2.1.1 Types of nanoparticles

PLGA-PVA-NPs were produced in our laboratory following Vasir and Labhasetwar protocol [149]. In particular, 6 types of NPs were produced: NP0, NP1, NP2, NP3, NP4, and NP5, as shown in Figure 4.12.

In detail, NPs consist of two parts: the external shell and the core. The shell is generally composed of PLGA (30mg/mL) and PVA (2% w/v) uncoated in NP0 and NP3, coated with Human Serum Albumin (HSA, 7.5mg/mL) in NP1, and NP4 or

coated with HSA (6mg/mL) and an anti-CD19 *Single Chain Fragment Variable* linked with a *human Fc* (ScFv-Fc; 1.5mg/mL) in NP2, and NP5.







| Name | NP0 | NP1 | NP2 | NP3 | NP4 | NP5 |
|---------------------|---|---|---|---|---|---|
| Structure |  |  |  |  |  |  |
| Polymers | PLGA-PVA | | | | | |
| Coating agent | none | HSA (7.5mg/mL) | HSA (6mg/mL) | none | HSA (7.5mg/mL) | HSA (6mg/mL) |
| Monoclonal antibody | none | | anti-CD19 Scfv-Fc (1.5mg/mL) | none | | anti-CD19 Scfv-Fc (1.5mg/mL) |
| Encapsulated agent | BSA-FITC 20mg/mL | | | Doxorubicin 25mg/mL | | |

Figure 4.12: Nanoparticles (NPs) used for *in vitro* and *in vivo* studies. NP0 were composed of PLGA-PVA polymers and filled with Bovine Serum Albumin (BSA) FITC conjugated. NP0 coated with only Human Serum Albumin (HSA) constituted NP1, while NP0 coated with a mixture of HSA and anti-CD19 *Single Chain Fragment Variable* linked with a *human Fc* (ScFv-Fc) constitute NP2. NP3, NP4 and NP5 have the same structure of NP0, NP1 and NP2, respectively, but were filled with doxorubicin.

The aim of HSA use is to guarantee a covalent binding of a protein that acts as a dysopsonin able to conceal NPs to the IS, while the targeting recombinant molecule can drive NPs on the surface of CD19-expressing tumor B-cells. For what concerns the core, NPs were filled with different compounds: FITC-conjugated Bovine Serum Albumin (BSA-FITC, 20mg/mL) in NP0, NP1, and NP2 or Doxorubicin (25mg/mL) in NP3, NP4, and NP5).

4.2.2 Developing the structure of nanoparticles

Targeted-NPs are composed of three main parts: the internal core, the surrounding shell, and the external targeting mechanism. The core contains the drug or molecules able to affect malignant cells, which should “execute the duty” once the target is reached, also through the efficiency of the targeting mechanism. The intermediate structure is represented by the shell, whose function is to protect the payload in the circulation from the IS, but also to avoid material loss, and simultaneously to be an efficient anchor for the targeting mechanism. To these ends, the shell structure was characterized in order to obtain the best fundamentals possible for the study.

4.2.2.1 *In vitro* characterization of nanoparticles

When injected into the bloodstream, NPs interact with more than 3000 circulating proteins, [100], and consequently, they attract plasma proteins onto their surface to form a coating layer called protein corona (PC). Among them, the most abundant in the human body is albumin, which is involved in the transport of nutrients and other proteins through the bloodstream. Moreover, albumin has a role in the PC as dysopsonin and hence contributes to reducing the bond and absorption of the other plasma proteins responsible for the MPS uptake. Starting from these considerations, we hypothesize that a pre-formed, covalently-bounded, protective albumin-corona should limit non-specific interactions and decrease opsonin deposition.

4.2.2.1.1 Shell and structure of nanoparticles

PLGA-PVA NPs were produced with or without covalently-linked albumin-coating (NP1 and NP0, respectively) and tested *in vitro*, showing round shapes, a diameter lower than 400 nm, and a negative surface charge. The average diameter, polydispersity index (PDI), and zeta potential values of the different types of NPs are reported in Figure 4.13 (A). These data, as expected, underline the fact that the coating addition caused a slight increment of the dimension (from 322.4±3.71nm to 348.7±4.43nm) and a slender reduction of the negative charge, which moves from -24.1 to -14.6mV. All NPs showed a spherical shape, as shown in Figure 4.13 (B) for NP0.

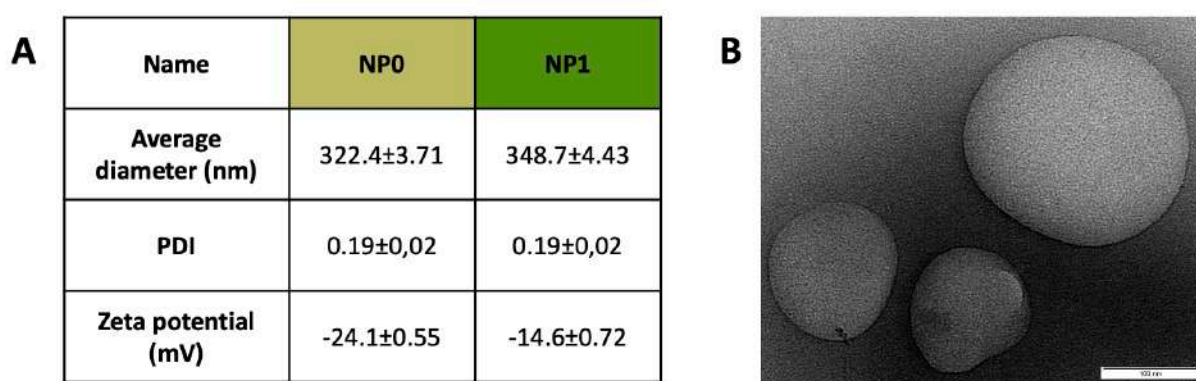


Figure 4.13: Nanoparticles characterization. (A) Physicochemical characteristics of NPs formulations. (B) TEM image of NP0 (scale bar 100 nm).

NPs formulations showed good stability over time, analyzing material stored at 4 °C for up to 6 months; indeed, no size increase, zeta potential modification, or NPs aggregation occurred.

An ELISA assay was set up to investigate the presence of HSA on the surface of NPs (Figure 4.14, A, and B). Briefly, the anti-HSA antibody was coated on the plate wells, then 0,1 and 1 μ L of NP0 and NP1 suspensions were incubated and their binding was revealed through a biotin-conjugated anti-HSA antibody, Alkaline Phosphatase (AP)-conjugated streptavidin and p-nitrophenyl phosphate (PNPP); optical density (OD) was read at 405nm (Figure 4.14, A).

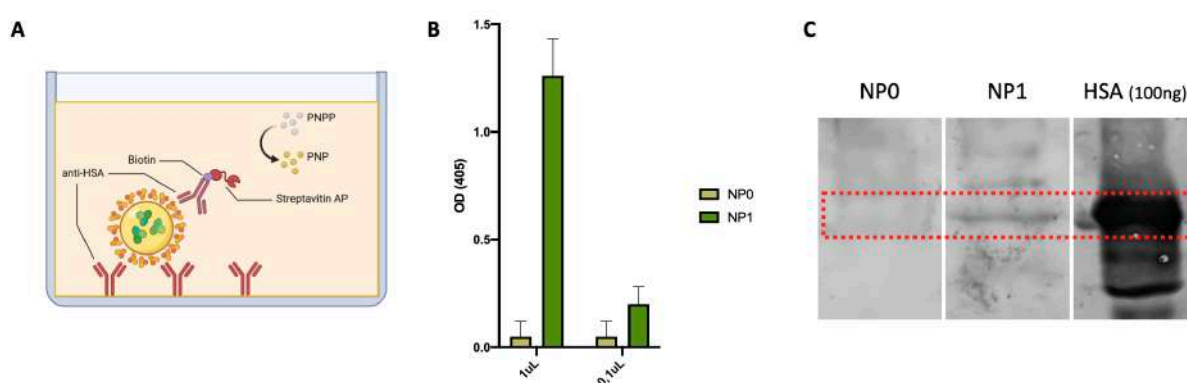


Figure 4.14: Coating with Human Serum Albumin. (A) Schematic representation of the ELISA sandwich performed to verify the presence of the HSA on NPs' surface. An anti-HSA was coated on the plate, NP0 or NP1 were added and revealed through an anti-HSA biotin-linked, which interact with streptavidin conjugated with Alkaline Phosphatase (AP). When the substrate (PNPP) was added, in presence of AP it turns in yellow PNP. (B) Results of the comparison between NP0 (without HSA) and NP1 (with HSA) in ELISA tests. The different values of OD establish the differences in the presence of HSA. Data have been reported as the mean \pm SD. (C) Western Blot analysis developed in non-reducing condition to compare NP0 (without HSA coating) and NP1 to the positive control.

The anti-HSA antibody interacted only with NP1 confirming the presence of the HSA layer on the surface of these NPs (Figure 4.14, B). These data were also demonstrated through the Western Blot analysis where NPs were destroyed and loaded into the gel. The HSA presence was revealed through the same antibodies employed in the ELISA assay; Figure 4.14, C shows the presence of HSA only on NP1.

4.2.2.1.2 Analysis of the Protein Corona on the NPs' surface

Once the HSA-coating was confirmed on the NPs' surface, these samples were used to evaluate the influence of this coating on the PC formation. Both NPs were incubated in presence of Normal Human Serum (NHS) and then analyzed by mass spectrometry. In particular, the composition and abundance of proteins adsorbed on

| Proteins on the NPO | | Proteins in common | | Proteins on the NP1 | |
|---------------------|----------|--------------------|----------|---------------------|----------|
| Q9BQI0-3 | Q9H0U3-2 | P60709 | P0DOX6 | Q96P26-2 | P13647 |
| Q9NZN9-2 | Q685J3-2 | P02768 | Q14624-2 | P02763 | Q4VXA5 |
| P08519 | Q9H094-2 | P02647 | Q9P260-2 | P04217-2 | Q2M1P5 |
| P02654 | Q96IV0-2 | P02652 | P13645 | P01023 | A6PVL3-2 |
| P54707-2 | P14543-2 | P02655 | P35527 | Q8NHS2 | P01042-2 |
| Q96L58 | P54368 | P02656 | P04264 | Q8IUA7-3 | Q8N2S1-4 |
| Q9C0J9 | Q9Y5G0-2 | P02649 | O95096 | Q9H221-2 | Q9Y6D9 |
| O75419-2 | Q9Y6V0-5 | P46100-2 | Q7Z5J4-2 | Q09666 | O15440-5 |
| O15078 | Q9H875-2 | P10909-2 | P0DJ19 | Q9BQI0-2 | P16333 |
| P52757-9 | Q9UNP9-2 | P55265-2 | Q8TF72 | Q8NAG6-1 | Q969V3-2 |
| Q9UBY8 | Q8IYL9 | Q63HQ2-2 | P46977-2 | Q8TER5-2 | Q9BTX1-4 |
| O76031 | Q9H1J1-2 | Q5W0V3-2 | Q9BZF9-2 | Q6ZS25-2 | Q86VF7-2 |
| Q9Y6Y1-2 | Q96FB5 | P02675 | Q99536-2 | Q8N3C0 | Q9UBU9-2 |
| P02748 | Q7L099-4 | Q7Z2K8-2 | P49750-3 | Q6ZP68 | Q6ZVCO-2 |
| Q969M2 | Q96NLO-4 | P00738-2 | P31629 | P04003 | Q9Y3B8 |
| Q96JB1-2 | P49589-2 | Q8IZT8 | | P01024 | Q58A45-2 |
| A0FGR8-2 | Q9UL54-2 | | | P0COL4-2 | P00747 |
| Q5T1M5-2 | Q8WUA7-3 | | | Q03001 | Q01860-2 |
| Q9NP62 | O94876 | | | Q9UBC2-2 | O75400-2 |
| Q12906-7 | O75865-2 | | | Q8TBR7-1 | Q05209-2 |
| A1L0T0 | Q6P9F5-2 | | | P07148 | Q8NC74 |
| A6NCM1 | Q9P2H5-2 | | | P02671 | Q7Z4M0 |
| Q9NVX7-2 | A4UGR9-4 | | | Q9P2B2 | Q9BZE1 |
| Q9H0B6 | Q9H7S9 | | | Q8NA03 | Q4U2R6 |
| | | | | Q16695 | P35542 |
| | | | | P69905 | Q8IYX7 |
| | | | | P68871 | Q9NQW1-5 |
| | | | | Q9Y450-4 | Q96FS4 |
| | | | | P02790 | Q8WWL2-2 |
| | | | | O15347 | Q9UQ35-2 |
| | | | | P0DOX5 | Q7RTT3 |
| | | | | P01876 | Q9NRC1-2 |
| | | | | P01859 | Q9BXT5 |
| | | | | P0DOY2 | A6NCK2 |
| | | | | P40189-3 | O75962-2 |
| | | | | P52292 | Q9P2H5 |
| | | | | P19823 | A6NCI4-2 |

79 proteins

105 proteins

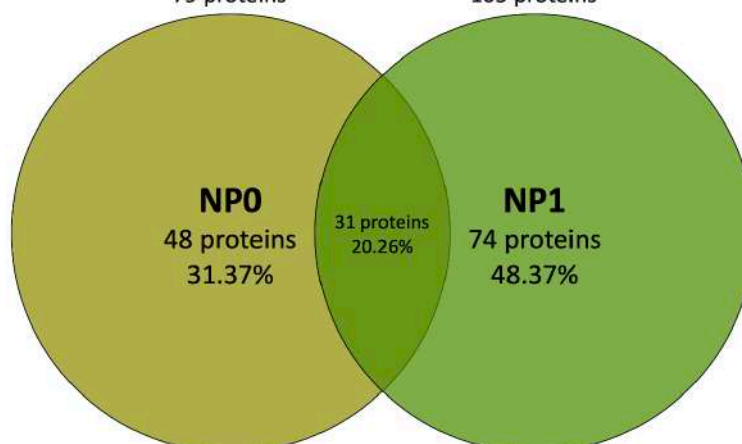


Figure 4.15: Data analysis from mass spectrometry. NPs were incubated with Normal Human Serum (NHS) for 1h and analyzed. Mass spectrometry analysis highlighted 48 proteins specific for NPO (left column), 74 proteins specific for NP1 (right column), and 31 proteins that are present on both NPs (central column).

NPs were characterized using LC-MS/MS in collaboration with Prof. Marcello Manfredi (University of Piemonte Orientale) and included in Figure 4.15. The presence of the HSA coating significantly influences the PC in the two preparations. In fact, 79 proteins resulted adsorbed on NP0 while 105 on NP1; among them, only 31 proteins were shared by both samples (Figure 4.15). Therefore, 48 proteins (31.37%) interact and remains specifically bound on the surface of NP0, 79 proteins (48.37%) interact only with NP1, and 31 proteins (20.26%) associate with both preparations. Among shared proteins, there are proteins both of the coagulation cascade and the complement system. This is consistent with previous research on other types of NPs [162], suggesting that these processes are involved in their opsonization and subsequent clearance [163]. Another relevant portion of the PC is represented by apolipoproteins and proteins generally belonging to the immune response. All these proteins can be divided into opsonins and dysopsonins. The first ones amplify the MPS uptake, while the second ones conceal NPs and prevent their clearance.

Since the albumin is classified as dysopsonin [164], the aim of the coating with HSA was to conceal NPs from the IS, and due to the importance of the balance between opsonins and dysopsonins, the different adsorption was analyzed. As evidenced in Figure 4.16, A, the two preparations of NPs differ in the amount of HSA present on their surface. This technique allowed to evaluate HSA either bound or adsorbed on NP1 and compare it with HSA adsorbed on NP0, showing the higher amount present on NP1.

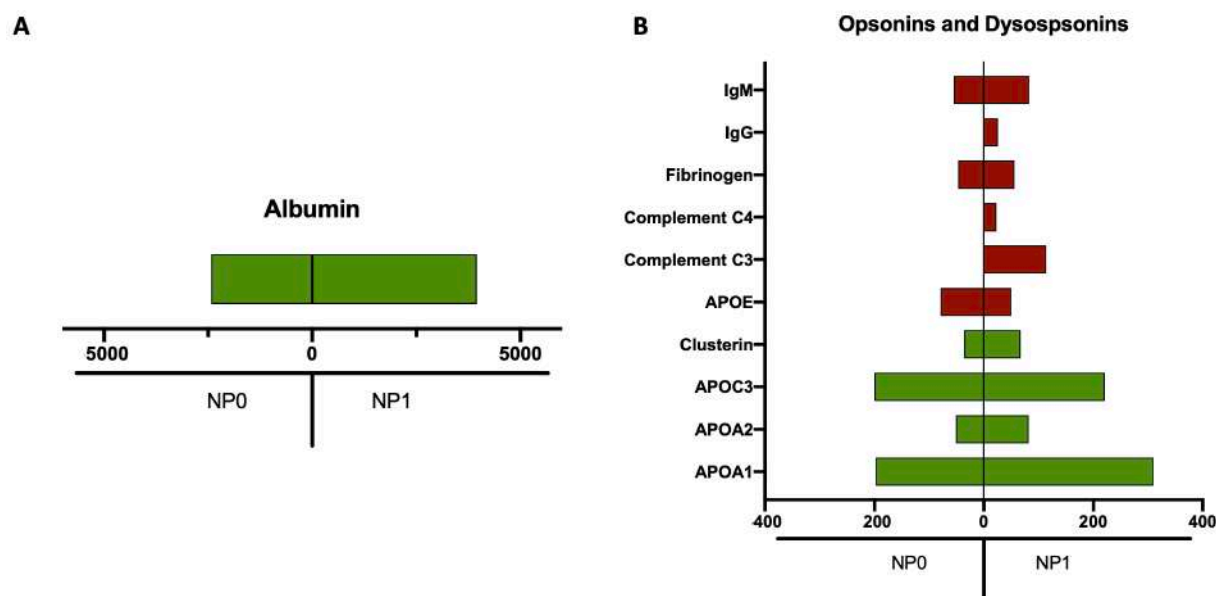


Figure 4.16: Differentially adsorbed opsonins and dysopsonins on NPs' surface. Data analysis from mass spectrometry underlines the difference in (A) HSA and (B) others opsonins/dysopsonins adsorption between NP0 and NP1.

Among other proteins, opsonins and dysopsonins [164] were isolated from the list and compared between the samples. Figure 4.16, B highlighted that more opsonins seem to be present on the surface of NP1 than NP0, including IgG and IgM but also complement proteins (C3 and C4), even if their presence is limited to the very first proteins of the CS cascade, a symptom of its incomplete activation, probably due to dysopsonins intervention. Dysopsonins seem also to be more adsorbed on the surface of the NP1. *In vitro* and *in vivo* studies have to be performed to clarify if HSA coating allowed the production of a favorable PC, able to reduce NP elimination by MPS, limits side effects and enhances NPs accumulation in the tumor microenvironment.

4.2.2.1.3 Interaction of nanoparticles with blood components

PLGA-PVA NPs were tested *in vitro* for functional characterization. Firstly, the direct lysis of red blood cells performed by NPs was investigated (Figure 4.17, A), resulting in the absence of mechanical disruption of red blood cells. Then, tests to clarify if NPs interfere with clotting formation or the activity of the CS were performed employing the same protocols used to test chitosan-NBs.

For what concerns the clotting formation, naked-NPs (NP0) and HSA-coated-NPs (NP1) were incubated in plasma and a solution containing Ca^{2+} , which triggers the coagulation process; samples turbidity was analyzed over time (Figure 4.17, B). This test demonstrated that NPs benefit from a very similar trend to that observed for simply activated plasma, used as control. These data can be summarized showing any significant difference between NPs' half coagulation time and their control (Figure 4.17, C). As said before for chitosan-NB, the interactions of NPs with the blood coagulation system may influence the natural balance between pro- and anticoagulant pathways, and undesirable effects NPs on the coagulation system have to be monitored to avoid toxicities. Comparing different types of nano-systems, we have generally shown a better profile for PLGA-PVA NPs than chitosan-NB.

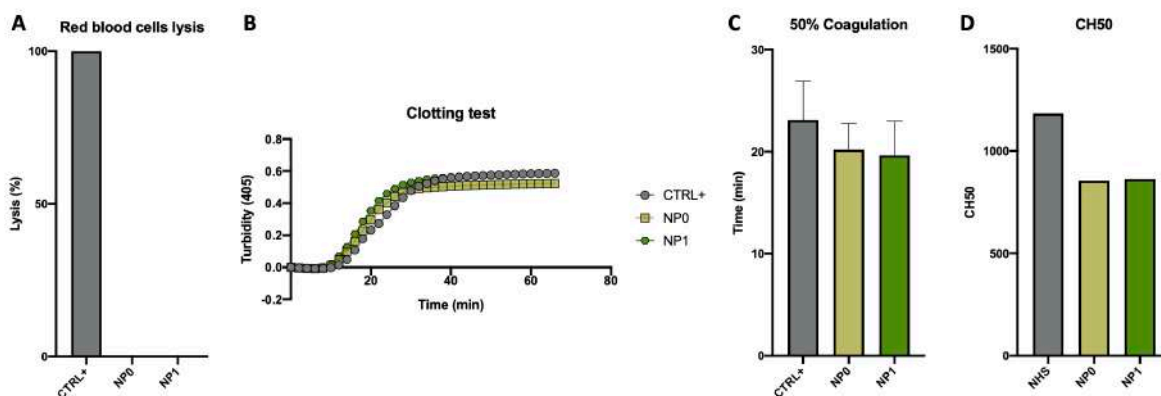


Figure 4.17: *In vitro* test of clotting formation and activation of classical pathway of the Complement. (A) *In vitro* analysis of the direct lysis of the red blood cells. (B) *In vitro* turbidity curve trend of NP0 and NP1 in activated plasma during time, compared with simple activated plasma as control. (C) The half coagulation time extrapolated from the curve of trend data showed a potential NPs effect on coagulation system. (D) CH50 hemolytic activity was evaluated in NHS, as a control, and in the same NHS after 2 hours *in vitro* incubation with NP0 or NP1. The consumption of components of the classical pathway shows a slight activation of the complement pathway. All data report as the mean \pm SD.

On the other hand, the consumption of the CS was investigated. In particular, was analyzed the residual activity of the classical pathway of the CS through the same test

used to characterize chitosan-NBs. Data demonstrated a reduced lytic activity of NHS after incubation with both NP0 and NP1 (Figure 4.17, D).

These results can be due to the activation of coagulation of complement processes by nano-systems or by a partial consumption of their proteins that are adsorbed on the surface of nanoparticles; in fact, also presented mass spectrometry analysis has not the possibility to discriminate between an activated protein, bound on NP surface (i.e. C3b), and a protein only adsorbed on NP surface (i.e. C3).

4.2.2.1.4 Binding and internalization of NPs inside malignant B-cells

To assess NPs binding and internalization on malignant B-cells different amounts of NP0 and NP1 were incubated with Nalm-6 (a leukemia cell line), in the presence or not of Normal Human Serum (NHS), and analyzed by flow cytometry. The presence of NHS permits an evaluation *in vitro* of the contribution of the PC on the surface of NPs. The binding/internalization of fluorescent NPs was evaluated by comparing the percentage of positive cells and Mean Fluorescence Intensity (MFI) values of cells incubated with NPs with the autofluorescence of cells. The obtained MFI values were then normalized by dividing them by the previously calculated fluorescence factor (FF) between the various types of NPs.

This analysis suggested a dose-dependent binding, as evidenced in Figure 4.18. In fact, the percentage of positive cells increases in both samples incubated with PBS and Serum in a dose-dependent manner, with a slight more positivity in favor of NP1 (Figure 4.18, A). Moreover, also the MFI increased with the same dose-dependency

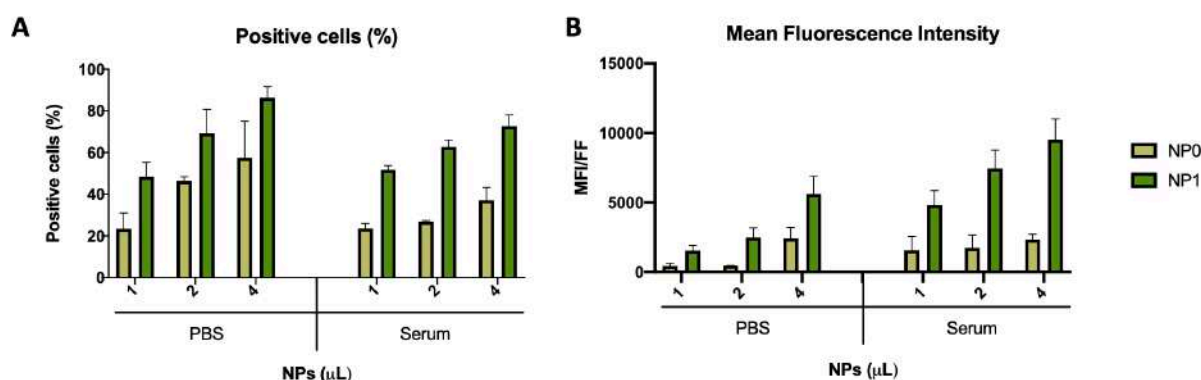


Figure 4.18: Binding/internalization of NPs in malignant B cells. 250,000 Nalm-6 cells were incubated in presence of Normal Human Serum (NHS) or not with different amounts (1μL, 2μL and 4μL) of uncoated (NP0) and coated NPs (NP1) at 37° for 1 hour and analyzed by flow cytometry. (A) The percentage of positive cells and (B) Mean Fluorescence Intensity (MFI), normalized for the Fluorescence Factor (FF), are reported in the histograms. Data have been reported as the mean ± SD.

(Figure 4.18, B), suggesting again that higher amounts of NPs, and in particular NP1 incubated with serum, are able to interact with a higher number of cells. The analysis suggested that the HSA-coating in the presence of serum increases the interaction with tumor B-cells.

To better evaluate the role of HSA in the PC's behavior and formation, the same test was performed on a monocyte cell line (Thp-1 cell line). The *in vitro* differentiation of Thp-1 to macrophages was made by incubating cells with PMA for 72 hours; cells were then incubated with increasing amounts of NP0 and NP1, in the presence or not of NHS, and then analyzed by flow cytometry. As shown for Nalm-6 cells, the binding/internalization of NPs was evaluated by comparing the percentage of positive cells and MFI values of cells incubated with NPs with the autofluorescence of cells (Figure 4.19). Since the coating with HSA was introduced with the aim to avoid macrophages' engulfment, this result was unexpected. In fact, the *in vitro* analysis demonstrated that in presence of serum, NP1 interacts in a dose-dependent manner with more cells with respect to NP0 (Figure 4.19, A) even if the histogram of MFI values suggests that the number of NPs for single cells remains constant for both NPs in presence of NHS or not.

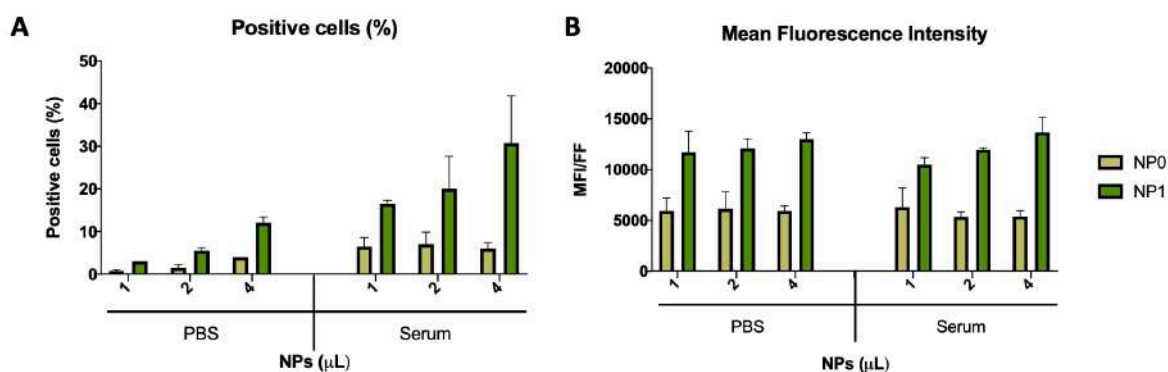


Figure 4.19: Binding/internalization of NPs in macrophages. Thp-1 (100,000 cells) were differentiated in macrophages in presence of PMA for 72h. Then, cells were incubated in presence of NHS or not with different amounts (1μL, 2μL and 4μL) of uncoated (NP0) and coated NPs (NP1) at 37° for 1 hour and analyzed by flow cytometry. (A) The percentage of positive cells and (B) Mean Fluorescence Intensity (MFI), normalized for the Fluorescence Factor (FF), are reported in the histograms. Data have been reported as the mean ± SD.

Thp-1 is a well-known cell line isolated from peripheral blood of an acute monocytic leukemia patient, widely employed to mimic macrophage behavior *in vitro* after its activation; it has been suggested that tumors utilize albumin as a source of energy, internalizing it and breaking it down into its components that are subsequently used

by cancer cells for their accelerated growth [165, 166]. Several albumin receptors have been described: the cell-surface glycoprotein (gp)18, gp30, gp60 (albondin), the magalin/cubilin complex, the secreted protein acidic and rich in cysteine (SPARC; also named osteonectin), and FcRn. In particular, SPARC has been demonstrated to be over-expressed in cancer tissues and inversely correlates with survival [166]. Moreover, FcRn protects albumin and IgG from degradation by binding both proteins with high affinity and consequently extends the half-life in serum [165]. Interestingly FcRn receptor is over-expressed on Thp-1 cells and this can explain the augmented internalization of NP1 with respect to NP0.

On these bases, the test was repeated on primary monocytes isolated from a healthy donor and macrophages obtained after their adhesion to the plate. The analysis was then performed as described for cell lines.

The results (Figure 4.20) demonstrated that in a more realistic environment, the presence of HSA-coating prevents the binding/internalization of these NPs with macrophages with respect to NP0 (Figure 4.20, A). Also, MFI data (Figure 4.20, B) are encouraging; mean values are comparable between the two samples (NP0 and NP1) incubated with serum, indicating that a minor number of macrophages interact with NP1 in comparison with NP0 (percentage of positive cells) in a context with serum, but these cells interact with the same amounts of both NPs *per cell* (MFI values).

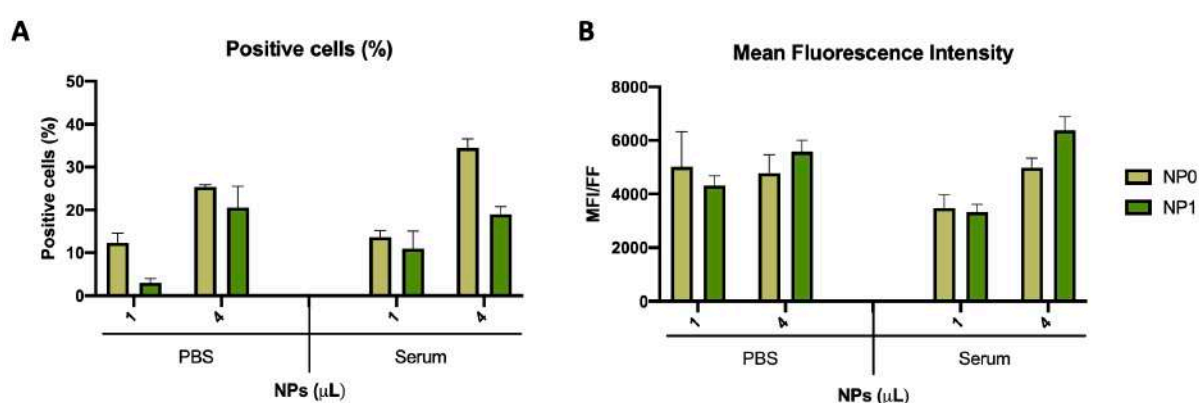


Figure 4.20: Binding/internalization of NPs in macrophages isolated from donor's blood. White cells were isolated and then macrophages were segregated by consecutive selections of adherent cells. 100,000 cells were incubated in presence of NHS or not with different amounts (1 μL, and 4 μL) of uncoated (NP0) and coated NPs (NP1) at 37° for 1 hour and analyzed by flow cytometry. (A) The percentage of positive cells and (B) Mean Fluorescence Intensity (MFI), normalized for the Fluorescence Factor (FF), are reported in the histograms. Data have been reported as the mean ± SD.

These data represent another confirmation of the initial hypothesis that the coating with HSA is able to influence the characters of the PC on NPs after the interaction with serum, as a background to potentially prolong NPs' circulation time, due to the difference in opsonins/dysopsonins balance in the PC and a reduced interaction with macrophages. Remains to reconfirmed their increased uptake by malignant cells, due to the over-expression of HSA-receptors on these cells.

All these results obtained from the *in vitro* experiments have encouraged the introduction of *in vivo* studies to evaluate the effective binding capacity of NPs in a biological system.

4.2.2.2 *In vivo studies*

The *in vivo* studies were conducted on zebrafish embryos. In particular, during this project, 3 different lines of zebrafish were employed: two transgenic lines, Tg(fli1:EGFP) and Tg(mpeg1:mCherry), and the WT ones. The first one (Tg(fli1:EGFP)) expresses enhanced green fluorescent protein-(EGFP, maximum excitation/emission 395/508nm) labeled endothelial vessels, contributing to obtaining an excellent view of these latter. The other transgenic line (Tg(mpeg1:mCherry)) is characterized by the mpeg1 promoter that drives transgene expression specifically in zebrafish embryonic macrophages, allowing their fluorescent visualization *in vivo* (maximum excitation/emission 590/650nm) [167]. Since 2005, when Lee et al. firstly employed zebrafish as an animal model for xenograft transplantation [168] it became increasingly popular. Several factors contributed to the selection of zebrafish embryos as a model for *in vivo* studies. In fact, the immaturity of adaptive immunity for up to 4-6 weeks makes xenografts possible. Moreover, embryos are completely transparent and this facilitates the imaging of the distribution of labeled cells and NPs [169, 170]. All the experimental procedures involving animals were done after the ministerial approval 04086.N.SGL.

4.2.2.2.1 *Biodistribution studies in healthy zebrafish larvae*

WT zebrafish larvae were employed for biodistribution studies.

In zebrafish, pigment formation is initiated during embryogenesis in the retinal epithelium and dorsolaterally in the skin. This process commences approximately 24 hours after fertilization and develops rapidly [171]. Since these pigmented areas are autofluorescent and can influence the following steps, the pigmentation was inhibited

through the employment of 1-phenyl 2-thiourea (PTU), which is an enzyme able to affect the conversion from tyrosine to melanin. Moreover, prior to hatching, the zebrafish embryo is surrounded by an acellular envelope, the chorion, which was manually removed -24 hours post-injection (hpi), ensuring the PTU effect (Figure 4.21, A).

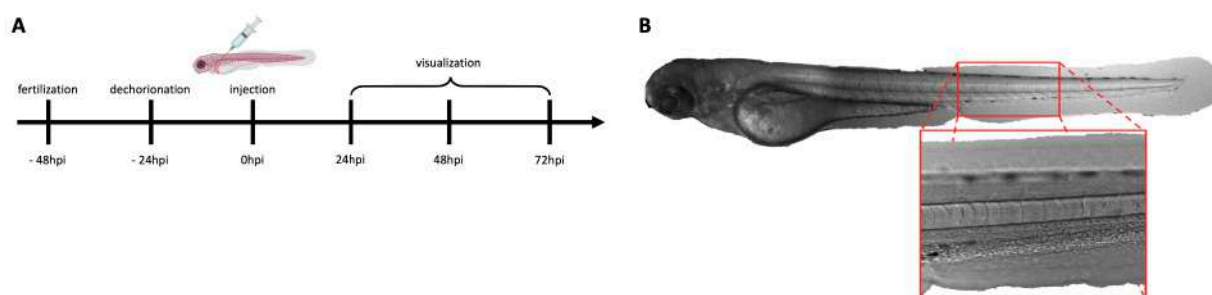


Figure 4.21: Zebrafish as animal model for *in vivo* studies. (A) Timeline of experimental procedure. Zebrafish were employed for a total of 5 days. The reference-point was set at the moment of the injection (0 hours post injection, hpi), which was performed 48 hours post fertilization. 24h prior the injection (-24hpi) embryos were manually dechorionated and incubated with PTU to prevent the formation of pigmented areas in the body. NPs were injected in the duct of Cuvier and analyzed 24, 48, 72hpi. (B) Representation of the ROI chosen for the analysis of fluorescent signals in zebrafish given by the presence of BSA-fitc-loaded NP0 or NP1.

NPs were injected in at least 20 animals per group into the duct of Cuvier, which is an embryonic vein structure collecting all venous blood and leads directly to the heart's *sinus venosus*, employed to despatch compounds into the bloodstream. Zebrafish were analyzed for the next three days through fluorescent microscopy and NPs have visualized following BSA-FITC (495 nm/521nm) encapsulated inside their core.

As described in Figure 4.21 (B), a Region Of Interest (ROI) was drawn in the tail of the fish, known as *posterior blood island* (PBI), in which the reduced speed of the bloodstream and its flatness facilitates the visualization of circulating NPs. The fluorescence in this area was then quantified in each larvae (Figure 4.22, A) and the corrected total cell fluorescence (CTCF) was calculated as follows:

$$CTCF = IntegratedDensity - [(AreaOfSelectedCell) \times (MeanFluorescenceOfBackgroundReadings)]$$

Then, results were normalized for the FF of the NPs, and results were employed to compare the fluorescent signals given by different NPs preparations (Figure 4.22, B). Data analysis highlight differences in the accumulation of the different preparation. In fact, in the analyzed ROI, the fluorescent signal given by NP0 is higher than the signal of NP1. Since the PBI is known to be a macrophages' rich area [172], the different accumulation of NPs is probably due to the macrophages' engulfment.

Therefore to verify this hypothesis the transgenic line of zebrafish, Tg(mpeg1:mCherry), was acquired. In fact, the *mpeg1*-driven transgenic lines were

exploited for imaging of interactions between macrophages and other immune cells *in vivo*, interaction studies between macrophages and intracellular pathogens, fluorescence-activated cell sorter, and analysis of macrophages as a pure population, reexamination of macrophage roles in inflammation, wound healing, and development, and also their interactions with other cell types (eg, vasculature, muscle) *in vivo* [167]. This transgenic

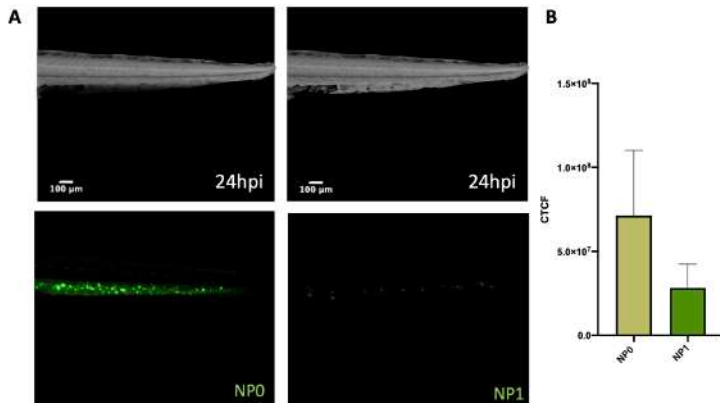


Figure 4.22: Different accumulation of NPs in the tail of zebrafish. (A) 4,6nL of NP0 and NP1 were injected in the duct of Cuvier and analyzed 24hpi. A ROI in the tail of fish, upper panels, was drawn and the fluorescence, lower panels, was quantified. (B) The corrected total fluorescence (CTCF) was normalized for the FF of NPs and compared. Data have been reported as the mean \pm SD.

line of zebrafish was initially analyzed over time (Figure 4.23, A), demonstrating that red-fluorescent macrophages are already visible in the PBI 24 hours post-fertilization (hpf) and therefore 24h prior to the injection of NPs.

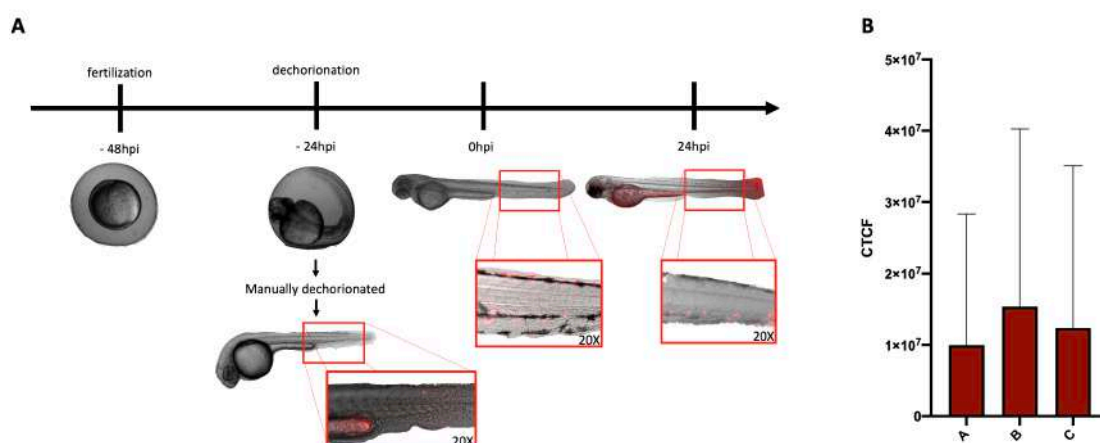


Figure 4.23: Timeline of macrophages' development in the transgenic line Tg(mpeg1:mCherry). (A) Already 24 hours prior to the injection red-fluorescent macrophages are visible in the PBI of manually dechorionated embryos, and their presence in this area persist in a consistent number also 24hpi when the fluorescent microscopy analysis is performed. (B) Data analysis of the CTCF of the red-fluorescent areas (macrophages) of zebrafish randomly assigned to three different groups, suggesting that the fluorescent signal of macrophages is comparable between different animals. Data have been reported as the mean \pm SD.

Zebrafish were randomly assigned to three different groups and the CTCF of red-fluorescent macrophages was analyzed demonstrating that the three groups of zebrafish possess comparable amounts of fluorescence and comparable amounts of macrophages (Figure 4.23, B).

This preliminary analysis demonstrated that Tg(mpeg1:mCherry) represents an interesting model in the study of the interaction between macrophages and NPs injected into the bloodstream. Therefore, 2 days post-fertilization NP0 or NP1 were injected in the duct of Cuvier of Tg(mpeg1:mCherry) transgenic line of zebrafish. As previously described, a ROI was drawn in the tail of the zebrafish and analyzed.

As shown in Figure 4.24 (A), in the selected ROI set in the PBI (upper central panel, b), there is the presence of both macrophages (red fluorescence, lower left panel, d) and NPs (green fluorescence, lower central panel, e). The upper left panel (A) shows the merged images of the area and different fluorescence signals. Focusing on the merging of the two fluorescence (upper right panel, c), it is easier to observe yellow spots given by the co-localization of green and red signals. These yellow spots were isolated (lower right panel, f) and employed to compare the co-localization signal given by macrophages and NP0 or NP1 (Figure 4.24, B). In particular, the CTCF demonstrated that NP1 are significantly less engulfed by macrophages than NP0.

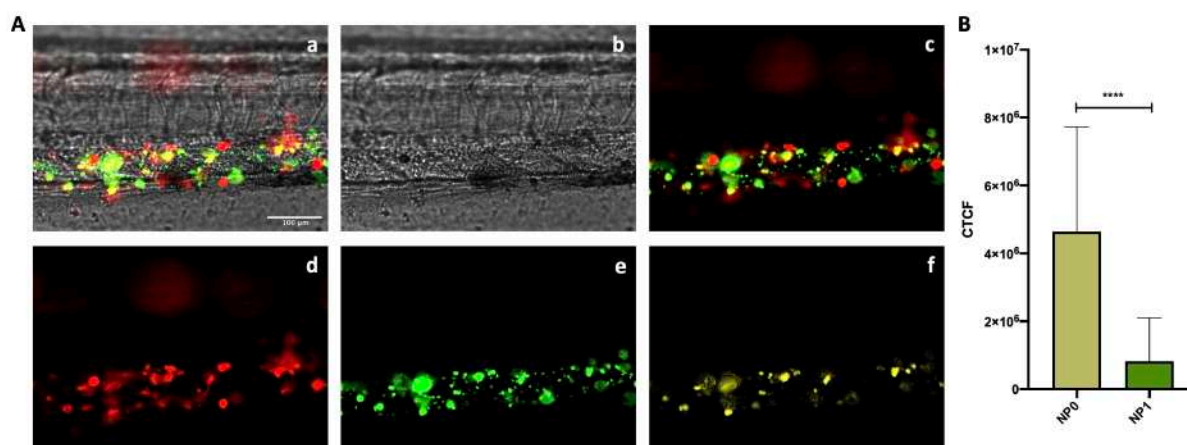


Figure 4.24: Co-localization between macrophages and NPs. (A) 4,6nL of NP0 or NP1 were injected in the duct of Cuvier of transgenic line Tg(mpeg1:mCherry), and 24hpi zebrafish were analyzed through fluorescence microscopy. Briefly, the upper right panel (a) represents the merge between macrophages (red, d), NPs (green, e) and zebrafish's tail (gray, b). Isolating the merge between macrophages (red, d) and NPs (green, e) it is easy to observe yellow spots give by the co-localization (f) of the two fluorescence and therefore by the NPs engulfed by macrophages. (B) Data analysis of the CTCF of the co-localized areas normalized for the FF of NPs. All data report as the mean \pm SD. $P \leq 0.0005 = ****$.

This result is consistent with what was previously obtained *in vitro* with donor white cells, demonstrating again the capacity of the HSA-coating on the surface of NPs to stealth nano-structures from the IS and probably increase their bioavailability.

4.2.3 Targeting mechanism: the specific delivery of nanoparticles

The purpose of the therapeutic strategy described in the aim is to guarantee the therapeutic effect given by the chemotherapeutic payload and simultaneously avoid side effects, “next-generation” approaches can be represented by nano-devices equipped with an active targeting mechanism. In particular, for what concerns B-ALL the best antigen candidate seems to be the CD19. Moreover, when commercial antibodies are bound to CD19, the complex is rapidly internalized, guaranteeing also the internalization of the linked molecule or structure [39, 161].

4.2.3.1 Production and characterization of the targeting mechanism

The targeting mechanism anti-CD19 is represented by a Single Chain Fragment Variable linked to a human Fc fragment of an IgG₁ (scFv-Fc). This structure consists of one side of a scFv, which is a fusion protein of the variable regions of the heavy (VH), a short linker peptide, and light chains (VL) of immunoglobulins; scFv is encoded in frame to the Fc region, the Hinge-CH₂-CH₃ domains of an antibody (Figure 4.25, A); the design of the scFv takes the cue from the VH and VL regions of

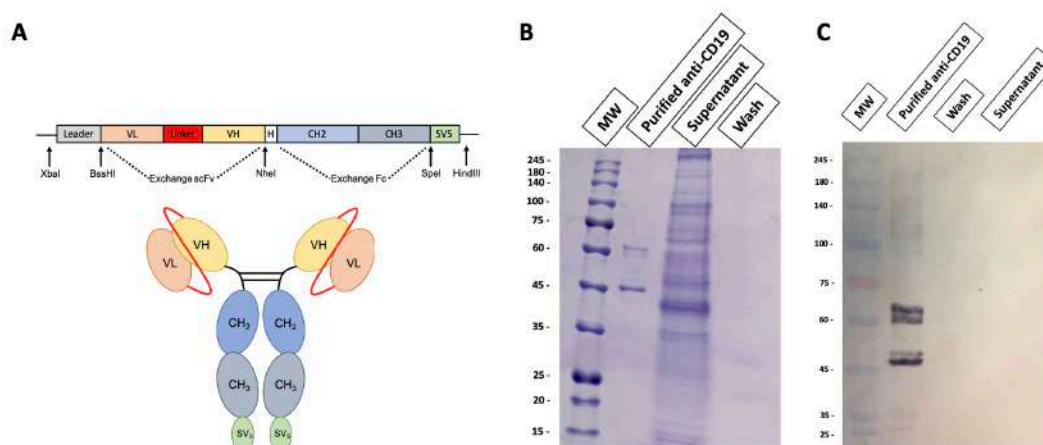


Figure 4.25: Design and production of the targeting mechanism. (A) The published sequence of VH and VL regions of Tafasitamab (MOR208), were obtained from its patent, optimized for CHO cells production, and then cloned in frame with Hinge-CH₂-CH₃-SV₅(tag) of human IgG₁ in an expression vector. CHO-S cells were then transfected and screened to obtain a population of cells highly producing the anti-CD19 scFv-Fc. (B) SDS-Page test performed to compare the supernatant of producing cells (lane 3) to the purified molecule (lane 2) and to the unbound material (lane 4). (C) Western Blot conducted in reducing condition of 300ng of the targeting molecule (lane 1) and developed with an anti-SV₅ antibody, which shows the correct molecular weight of 55 kDa.

MOR208 (Patent n°: US 2014/0227277 A1), also known as Tafasitamab, an Fc-modified, humanized, anti-CD19 antibody, combined with the immunomodulatory drug lenalidomide, actually in an open-label, single-arm, phase II study in patients with relapsed/refractory diffuse large B-cell lymphoma (DLBCL). The published amino-acidic sequences were optimized for CHO-cell production and then cloned in frame with Hinge-CH2-CH3 of human IgG₁ in a eukaryotic expression vector. CHO-S cells were then transfected and screened to obtain a population of cells highly producing the anti-CD19 scFv-Fc in cell supernatant. The molecule was purified from the cell-conditioned medium, checked for purity, and quantified. Figure 4.25, B shows SDS-PAGE stained with Coomassie Blue of the purified anti-CD19, compared to the supernatant and the unbound material. The same material was also analyzed by western blot using an anti-SV₅ antibody (Figure 4.25, C) evidencing the correct molecular weight of the recombinant molecule. The purified molecule was then tested for the binding to the antigen; the anti-CD19 molecule was incubated with CD19⁺ cells (Bjab and Nalm-6 cells) and the interaction was revealed through an Alexa Fluor 488-conjugated antibody in flow cytometric analysis and fluorescence microscopy (Figure 4.26, A and B, respectively).

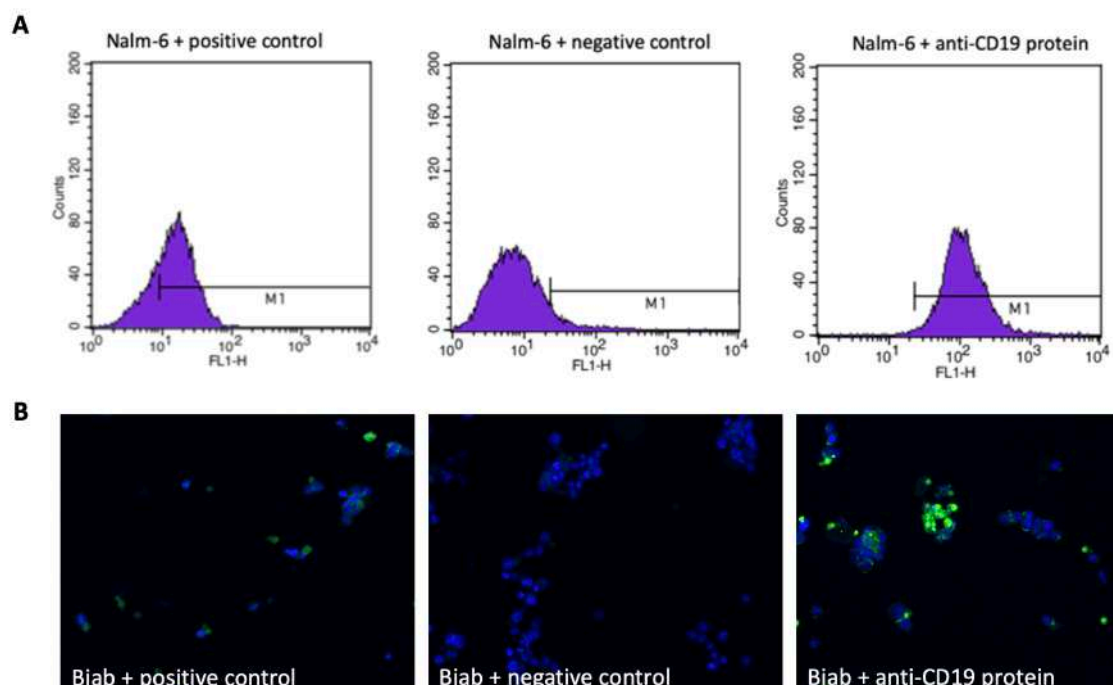


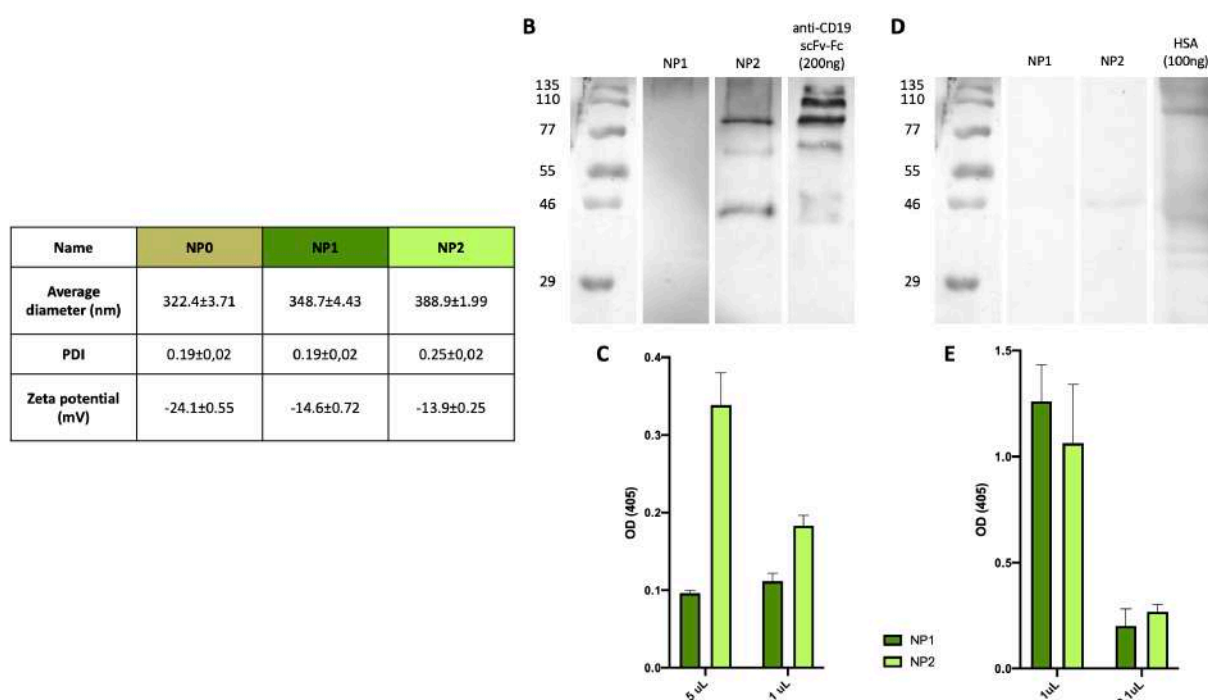
Figure 4.26: Binding of the targeting molecule to CD19-expressing cells. 250,000 Nalm-6 or Bjab were incubated for 1h with 10ng/ μ L of anti-CD19 scFv-Fc or controls and revealed through an anti-human antibody conjugated with AlexaFluor 488. **(A)** Flow cytometric analysis of Nalm-6 cells in which the fluorescent signal (FL1-H) of cells incubated with the negative control (central panel) increases if cells were incubated with a positive control (left panel) or the homemade anti-CD19 (right panel). **(B)** The same experiment was performed with Bjab cells and analyzed in fluorescent microscopy. The green fluorescent signal is appreciable in cells incubated with positive control (left panel) or with the homemade anti-CD19 protein (right panel), whereas there is the absence of signal with negative control (central panel).

Flow cytometric analysis highlights that the fluorescent signal of cells incubated with the negative control (Figure 4.26, A, central panel) increases if cells were incubated with the commercial anti-CD19 mAb (Figure 4.26, A, left panel) or even more with the homemade anti-CD19 scFv-Fc (Figure 4.26, A, right panel). The same experiment was performed with Bjab cells, a BL cell line, and analyzed through fluorescent microscopy. The green fluorescent signal is appreciable in cells incubated with the positive control (Figure 4.26, B, left panel) or with the homemade anti-CD19 protein (Figure 4.26, B, right panel), where the fluorescent signal is even higher, as demonstrated with Nalm-6 cells in flow cytometry. These tests demonstrated that the homemade scFv-Fc is able to bound CD19⁺ cells, resulting in an ideal targeting mechanism candidate.

4.2.3.2 Targeted nano-devices: *in vitro* characterization

According to the recent literature, already discussed in the introduction of this work, nanoparticles can be designed in order to increase specificity for a target tissue reducing doses of drugs and their consequent toxicity. Following the rationale of the project, biodegradable polymeric nanoparticles made of PLGA-PVA and coated with HSA were equipped with the homemade scFv-Fc anti-CD19 and characterized. This final preparation of NPs showed a diameter lower than 400 nm and a negative surface charge. The average diameter, polydispersity index (PDI), and zeta potential values of the different types of NBs are reported in Figure 4.27, A). These data underline the fact that the addition of the targeting mechanism demonstrated a slight increment of the dimension (from 348.7 ± 4.43 nm to 388.9 ± 1.99 nm) and a slender reduction of the negative charge which moves to -13.9 mV. NPs formulations showed good stability over time when stored at 4 °C for 6 months. Indeed, no size increase, zeta potential modification, or NB aggregation occurred (data not shown).

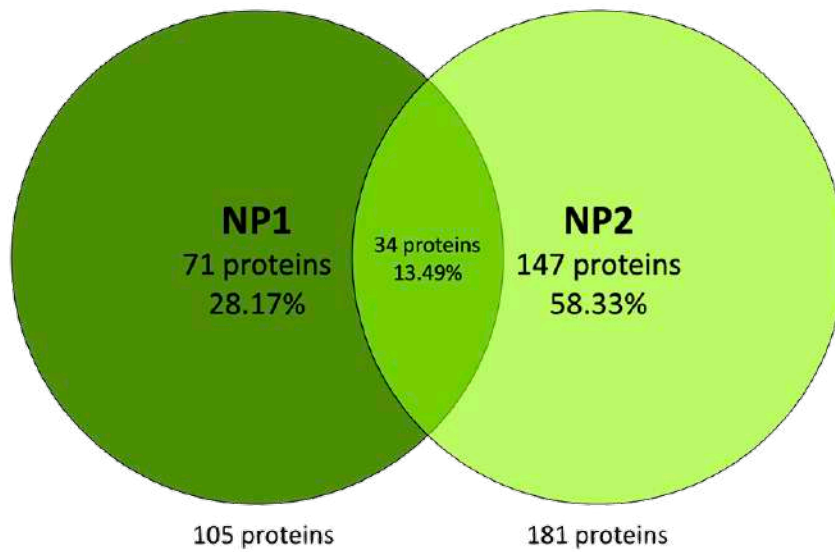
Western Blot analysis (Figure 4.27, B), was conducted in non-reducing conditions, and an ELISA test (Figure 4.27, C) were performed to evaluate the presence of the targeting molecule comparing NP1 (untargeted-NPs) and NP2 (targeted-NPs) to a positive control (purified recombinant antibody). The different values of OD and the presence of bands in the Western Blot showed the presence of anti-CD19 protein only on the surface of NP2. The same tests were performed with the aim to confirm also the presence of the HSA coating. Western Blot analysis (Figure 4.27, D) and



ELISA (Figure 4.27, E) demonstrated that the HSA coating is maintained also in the presence of Anti-CD19 scFv-Fc.

4.2.3.2.1 Analysis of the Protein Corona on the NPs' surface

The consequence of modifications on NPs surface is a different interaction of serum proteins; for this reason, PC's compositions was evaluated. To this end, NP1 and NP2 were incubated in presence of NHS, and bound material was then analyzed by mass spectrometry. The compositions and abundances of proteins adsorbed on NPs were firstly characterized using LC-MS/MS. These data were obtained in collaboration with Prof. Marcello Manfredi (University of Piemonte Orientale), which provided the list of proteins and their abundance (Figure 4.28). The anti-CD19 scFv-Fc on the surface of NPs significantly influences the PC. In fact, NP1 adsorbed 105 proteins and NP2 181; among them, 34 proteins were shared by both particles (Figure 4.28). Therefore, 71 proteins (28.17%) interact and remains specifically bound on the surface of NP1, 147



| Proteins on the NP1 | | | Proteins in common | | | Proteins on the NP2 | | | | | | | |
|---------------------|--------------|----------|--------------------|----------|-------------|---------------------|-------------|-----------|--------------|------------|--------------|----------|--------------|
| Q9P25-2 | SNTB1_HUMAN | A6PVL3-2 | KNOC1_HUMAN | Q8NPS2 | AATC2_HUMAN | Q8ZT8 | HS355_HUMAN | P52209-2 | EPGD_HUMAN | P51978-2 | HNRPK_HUMAN | P42766 | RL35_HUMAN |
| P02763 | ALAG1_HUMAN | Q8N251-4 | LTBP4_HUMAN | P60709 | ACTB_HUMAN | Q01876 | IGHA1_HUMAN | Q8W022 | ABRA_HUMAN | P07900-2 | HS90A_HUMAN | P18077 | RL35A_HUMAN |
| P04217-2 | A1BG_HUMAN | Q9V6D9 | MDM11_HUMAN | Q98Q10-2 | AIF1L_HUMAN | P01859 | IGHG2_HUMAN | P53396-2 | ACLY_HUMAN | P08258 | HS90B_HUMAN | P62424 | RL7A_HUMAN |
| P01023 | A2MG_HUMAN | D15440-5 | MIRP5_HUMAN | P02768 | ALBU_HUMAN | P00072 | IGLC2_HUMAN | Q08043 | ACTN3_HUMAN | P11142-2 | HSP7C_HUMAN | Q8NHWS | RLAOL_HUMAN |
| Q8UAA7-3 | ABC9_HUMAN | P16333 | NCK1_HUMAN | P02647 | APOA1_HUMAN | P52252 | INM1L_HUMAN | P80394 | ADH7_HUMAN | Q52743 | HTRAI1_HUMAN | P09651 | ROA1_HUMAN |
| Q9H221-2 | ABCG8_HUMAN | Q969V3-2 | NCLN_HUMAN | P02652 | APOA2_HUMAN | Q14624-2 | ITIH4_HUMAN | Q727M1 | AGRD2_HUMAN | A0A0A0V514 | HV145_HUMAN | P62277 | RS13_HUMAN |
| Q05666 | AHKK_HUMAN | Q987K1-4 | NDCL1_HUMAN | P02653 | APOC2_HUMAN | P13645 | K1C10_HUMAN | Q8W725 | ANR31_HUMAN | Q13089-2 | IFT88_HUMAN | P62244 | RS15A_HUMAN |
| Q8HAG6-1 | ANKK1_HUMAN | Q55096 | NIX22_HUMAN | P02656 | APOC3_HUMAN | P35527 | K1C9_HUMAN | P02654 | APOC1_HUMAN | P000X2 | IGA2_HUMAN | P62249 | RS16_HUMAN |
| Q8TER5-2 | ARIH40_HUMAN | Q86V77-2 | NIAP_HUMAN | P02649 | APOE_HUMAN | P04264 | K2C1_HUMAN | P05090 | APOD1_HUMAN | P01857 | IGHG1_HUMAN | P08708 | RS17_HUMAN |
| Q62525-2 | ARHG1_HUMAN | Q6ZV02-2 | NYAP1_HUMAN | P06100-2 | ATRX_HUMAN | P01042-2 | KNG1_HUMAN | Q8WXX1 | ASB15_HUMAN | P01860 | IGHG3_HUMAN | P62269 | RS18_HUMAN |
| Q8N3C0 | ASCC3_HUMAN | Q9Y388 | ORH1_HUMAN | P10909-2 | CLUS_HUMAN | Q9UBU9-2 | NXF1_HUMAN | O75185-2 | AT2C2_HUMAN | P01871-2 | IGHM_HUMAN | P15880 | RS2_HUMAN |
| Q6Z9F8 | ATP1U1_HUMAN | Q58A45-2 | PANL1_HUMAN | P01024 | CO1_HUMAN | Q05209-2 | PTN12_HUMAN | Q8TE59 | ATS151_HUMAN | P000X7 | IGK3_HUMAN | P60866-2 | RS20_HUMAN |
| P08003 | CIBPA_HUMAN | P00747 | PLMN1_HUMAN | P0C2L4-2 | CO4A_HUMAN | Q4U2R6 | RMS1_HUMAN | P02745 | CIQA_HUMAN | Q5VWKS-7 | IL23R_HUMAN | Q71UM5 | RS27L_HUMAN |
| P55265-2 | DSRAD_HUMAN | Q01880-2 | POSF1_HUMAN | Q722K8-2 | GRIN1_HUMAN | P00J49 | SAZ2_HUMAN | P02747 | CIQC_HUMAN | Q9WQ38-3 | IKK5_HUMAN | P23396-2 | RS3_HUMAN |
| Q03001 | DVST_HUMAN | O75400-2 | PRADA4_HUMAN | P69905 | HBA_HUMAN | Q07772 | SHRM3_HUMAN | P05871 | C1S_HUMAN | P15908 | K2Z1_HUMAN | P61247 | RS3A_HUMAN |
| Q63HQ2-2 | EGFL4_HUMAN | Q72514-2 | RAI1_HUMAN | P68871 | HBB_HUMAN | Q59536-2 | VAT1L_HUMAN | O14523 | C2C2L_HUMAN | P19013 | K2C4_HUMAN | Q8T047 | RS4Y2_HUMAN |
| Q9UBC2-2 | EPTSR1_HUMAN | Q8WC74 | RB81L_HUMAN | P00738-2 | HPT1_HUMAN | P31629 | ZEP2_HUMAN | Q9Y549-2 | CABIN_HUMAN | Q9N0V2 | KCTD5_HUMAN | P62753 | R5E_HUMAN |
| Q9W0V3-2 | F16B1_HUMAN | Q729M0 | REL14_HUMAN | | | | | Q15878-2 | CACIE_HUMAN | Q8H086 | KLC2_HUMAN | P62081 | RS7_HUMAN |
| Q8TR87-1 | FASTA_HUMAN | Q8B2E1 | RM87_HUMAN | | | | | Q43866 | CD5L_HUMAN | P07195 | KPYM_HUMAN | P62241 | RS8_HUMAN |
| P07146 | FABP1_HUMAN | P35542 | SAA4_HUMAN | | | | | B2FD01 | CENP1_HUMAN | A0A0C4DH55 | KVDX7_HUMAN | P46701 | RS9_HUMAN |
| P02671 | FIBA_HUMAN | Q8VX7 | SAXD1_HUMAN | | | | | O55813 | CER1_HUMAN | P00338-3 | LDHA_HUMAN | P08865 | RS9A_HUMAN |
| P02675 | FBF3_HUMAN | Q9NQW3-5 | SC3B1_HUMAN | | | | | Q9H2X0-5 | CHRD_HUMAN | P07195 | LDHB_HUMAN | Q82503-2 | S14L1_HUMAN |
| Q9P282 | FPR3_HUMAN | Q86F54 | SIP1A1_HUMAN | | | | | Q96526-2 | CKSP1_HUMAN | P06858 | LIP1L_HUMAN | Q61841 | S4A10_HUMAN |
| Q8NA03 | FSIP1_HUMAN | Q8WV12-2 | SPIR2_HUMAN | | | | | P20298 | COSA1_HUMAN | Q5N2R2 | LRP1B_HUMAN | P84350-3 | SKOR1_HUMAN |
| Q15695 | H31T_HUMAN | Q9UG35-2 | SRRM2_HUMAN | | | | | P23528 | COF1_HUMAN | Q9H0U3-2 | MAGT1_HUMAN | Q8ND07 | SPART1_HUMAN |
| Q9Y450-4 | HBS3L_HUMAN | Q7R773 | SSX9_HUMAN | | | | | P38432 | COL1_HUMAN | Q72204-2 | MAMC2_HUMAN | Q9U8B2 | SPAT2_HUMAN |
| P02790 | HMO2_HUMAN | Q9NRC1-2 | ST7_HUMAN | | | | | Q9U8F2-2 | COPG2_HUMAN | Q8UHC1-2 | MLHE_HUMAN | Q68X87 | SPT16_HUMAN |
| O15347 | HMOGB3_HUMAN | P46977-2 | STT3A_HUMAN | | | | | Q9Y600-2 | CSAD_HUMAN | P20545 | MFRD1_HUMAN | Q07955-3 | SRPF1_HUMAN |
| P0D0X5 | IGG1_HUMAN | Q96X75 | TEK3L1_HUMAN | | | | | O00622 | CYR61_HUMAN | Q685J3-2 | MUC17_HUMAN | Q72289 | SSAS1_HUMAN |
| P0D0X6 | IGM1_HUMAN | A6NCK2 | TRAB3_HUMAN | | | | | P59665 | DEF1_HUMAN | P15579 | MYHE_HUMAN | Q8X0J1-3 | SUGP2_HUMAN |
| P40169-3 | IL6RB_HUMAN | O79963-2 | TRIO_HUMAN | | | | | Q5V7E0 | EF1A3_HUMAN | P15172 | MYOCD1_HUMAN | Q82777-2 | SYN2_HUMAN |
| P19823 | ITIH2_HUMAN | Q96793-2 | UACA_HUMAN | | | | | P13639 | EF2_HUMAN | Q9BK09 | NAAT5_HUMAN | Q135Y0 | TLOP1_HUMAN |
| Q9P260-2 | K146B_HUMAN | Q8P7H5 | UBP35_HUMAN | | | | | Q8ND11 | EBHP2_HUMAN | Q8NA29-3 | NLS1_HUMAN | Q08Q03 | TBA1C_HUMAN |
| P13647 | K2C5_HUMAN | A6N014-2 | VAVAS1_HUMAN | | | | | Q98U13-3 | ELMO2_HUMAN | Q8F000 | OR2T2_HUMAN | P07437 | TBBS_HUMAN |
| Q4VXAS | KHDC1L_HUMAN | P49750-3 | YLPAT1_HUMAN | | | | | Q6ZMVA3-2 | EMAL16_HUMAN | Q9ULB9-6 | P2R1Q1_HUMAN | P17987 | TCFA_HUMAN |
| Q2M1P5 | KIF7_HUMAN | | | | | | | Q98W95-1 | FACD2_HUMAN | Q9UQ80 | PA2G4_HUMAN | P78371-2 | TOPB_HUMAN |
| | | | | | | | | Q66CS3 | FAF2_HUMAN | P25122-2 | PCSKE_HUMAN | Q43151-4 | TET3_HUMAN |
| | | | | | | | | Q15485 | FN2_HUMAN | Q504Y2 | PKDCC_HUMAN | Q95932-2 | TGMB1_HUMAN |
| | | | | | | | | O75626-2 | FN3_HUMAN | Q8TCL6-3 | PREK1_HUMAN | Q8N242-8 | TITR1_HUMAN |
| | | | | | | | | P04406 | G3P_HUMAN | Q8V19 | PSYR_HUMAN | P62094-2 | TMP1_HUMAN |
| | | | | | | | | O14556 | G3PT_HUMAN | Q725J4-3 | RAI1_HUMAN | P45378-2 | TNNT3_HUMAN |
| | | | | | | | | P32455 | GBP1_HUMAN | P52826 | RAN_HUMAN | Q96556-2 | TOPRS_HUMAN |
| | | | | | | | | Q98684 | GF1_HUMAN | P18821-2 | RL17_HUMAN | Q18061 | TRDN_HUMAN |
| | | | | | | | | Q6PRD1 | GP179_HUMAN | Q02543 | RL18A_HUMAN | P04064 | VINC_HUMAN |
| | | | | | | | | P16402 | H13_HUMAN | P35268 | RL22_HUMAN | Q9Y351-2 | WNK2_HUMAN |
| | | | | | | | | P16104 | H2AX_HUMAN | Q9UN03 | RL28L_HUMAN | Q14980 | XPOL_HUMAN |
| | | | | | | | | Q9QW46-2 | H2B2F_HUMAN | P46779-2 | RL28_HUMAN | Q8I2N3-3 | ZDH2A_HUMAN |
| | | | | | | | | P06431 | H31_HUMAN | P62888 | RL30_HUMAN | Q8H759 | ZN703_HUMAN |
| | | | | | | | | P62805 | H4_HUMAN | P49207 | RL34_HUMAN | Q32M1Q | ZN750_HUMAN |

Figure 4.28: Data analysis from mass spectrometry. NPs were incubated with Normal Human Serum (NHS) for 1h and analyzed. Mass spectrometry analysis highlighted 105 proteins specific for NP1 (left column), 181 proteins specific for NP2 (right column), and 34 proteins that are present on both NPs (central column).

proteins (58.33%) interact with NP2, and 34 proteins (13.49%) associate with both preparations.

In particular, among shared proteins, as described here before, there are proteins both of the coagulation cascade, of the complement system, apolipoproteins, and proteins generally belonging to the immune response. Part of these proteins was divided into opsonins and dysopsonins, according to their ability to amplify the MPS uptake or conceal NPs from the IS (Figure 4.29).

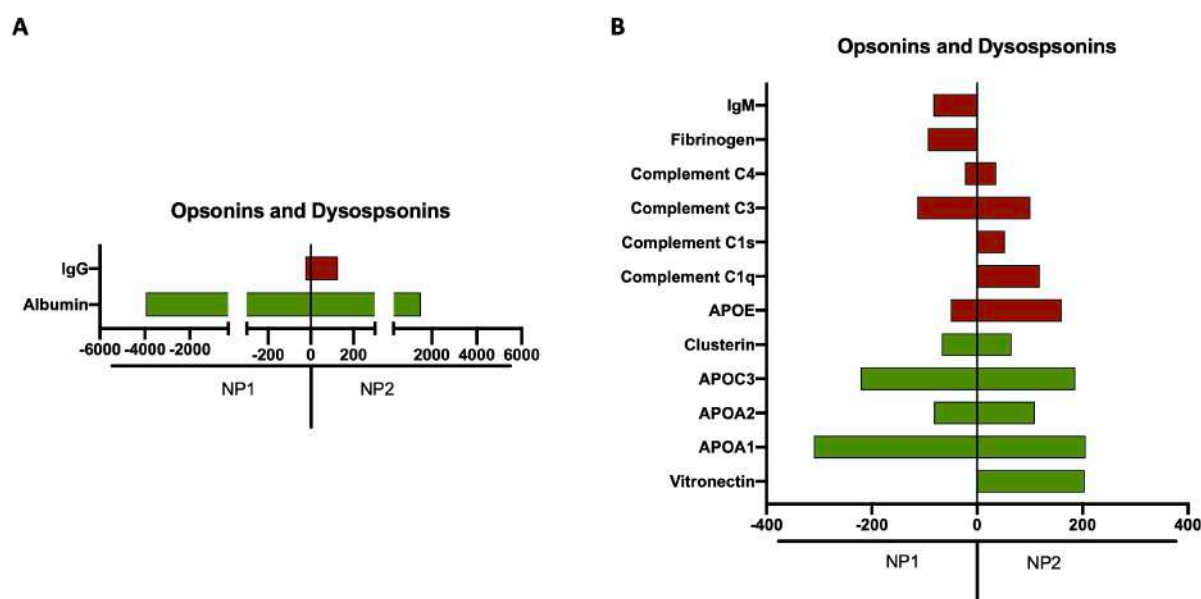


Figure 4.29: Differentially adsorbed opsonins and dysopsonins on NPs' surface. Data analysis from mass spectrometry underlines the difference in (A) HSA and IgG coating and (B) others opsonins (in red)/dysopsonins (in green) adsorption between NP1 and NP2.

First of all the presence of the anti-CD19 and the HSA on the surface of NPs were analyzed. As highlighted in Figure 4.29 (A), mass spectrometry analysis confirms the presence of the homemade scFv-Fc only in NP2. In fact, there is a difference in the adsorption of IgG on the surface of NPs, and, even though IgG are classified as opsonins, the anti-CD19 possesses the Fc fragment of an IgG1. The presence of albumin was also confirmed, and according to the protocol employed to label NPs, less albumin was coated on NP2 in comparison with NP1. Moreover, among the proteins, opsonins, and dysopsonins [164] were isolated from the list and compared between the samples. Figure 4.29, B highlighted that more opsonins are present on the surface of NP2 than NP1; IgM and fibrinogen are located only in the NP1 column, whereas APOE and complement proteins (C1q, C1s, C3, and C4) are located mostly in the NP2 column. Nevertheless, their presence is, again, limited to the very first

proteins of the CS cascade, a symptom of its incomplete activation, probably due to dysopsonins intervention, which are more adsorbed on the surface of the NP2.

4.2.3.2.2 Interaction of nanoparticles with blood components

Since IgG are classified as opsonins and NP2 possess on their surface the scFv-Fc, NPs were initially characterized *in vitro*. Firstly, the direct lysis of red blood cells performed by NPs was investigated (Figure 4.30, A), resulting in the absence of mechanical disruption of red blood cells. Then, tests to clarify if NPs interfere with clotting formation or the activity of the CS were performed employing the same protocols used before for the characterization of NP0 and NP1.

As shown in Figure 4.30 (B), for what concerns the clotting formation assay, targeted-NPs and untargeted-NPs benefit from a very similar trend to that observed for simply activated plasma, used as control, even if the half coagulation time extrapolated from the curve (Figure 4.30, C) demonstrated that there is a slight acceleration in the coagulation process in NP2 samples, but with no statistical difference. This is probably due to the presence of a different PC on the surface of NPs.

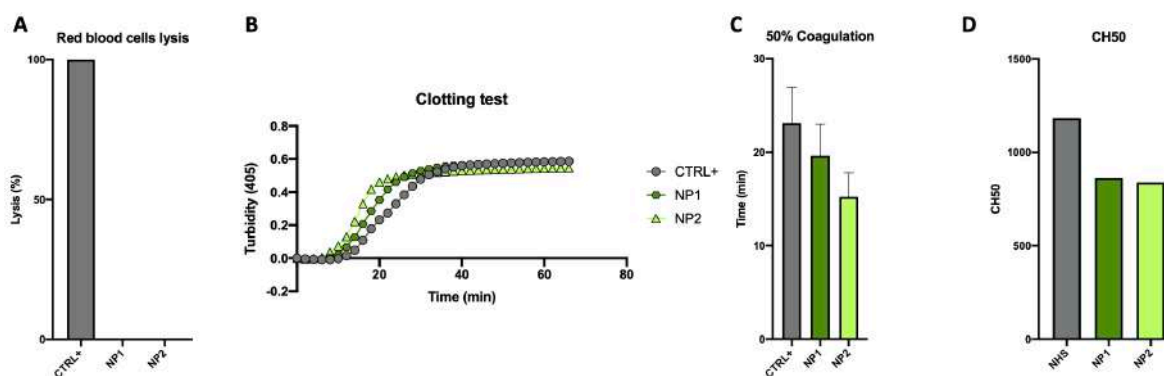


Figure 4.30: *In vitro* test of clotting formation and activation of classical pathway of the Complement. (A) *In vitro* analysis of the direct lysis of the red blood cells. (B) *In vitro* turbidity curve trend of NP1 and NP2 in activated plasma during time, compared with simple activated plasma as control. (C) The half coagulation time extrapolated from the curve showed a potential NP2 effect on coagulation system. (D) CH50 hemolytic activity was evaluated in NHS, as a control, and in the same NHS after 2 hours *in vitro* incubation with NP1 or NP2. The consumption of components of the classical pathway shows a slight activation of the complement pathway. All data report as the mean \pm SD.

For what concerns the evaluation of the residual activity of the CS after the incubation of serum with NPs (Figure 4.30, D), it was demonstrated that NP2 reduces CS activity as well as NP1, probably because of a similar capacity to activate the system (even if a recombinant antibody is bound on the surface as targeting agent) or the similar protein adsorption on the surface of nanoparticles. These data confirm the previous

results obtained with mass spectrometry even if more tests are needed to confirm their safety *in vivo*, but our data suggest that the coupling of a targeting recombinant antibody on the surface of polymeric NPs do not enhance their side effects after the injection in the circulation.

4.2.3.2.3 Binding and internalization of NPs inside malignant B-cells

To assess the efficacy of the targeting mechanism after the covalent binding on NPs in the binding on and internalization in malignant B-cells, different amounts of NP1 and NP2 were incubated, in the presence or not of NHS, with Nalm-6 and analyzed through flow cytometry. The binding/internalization of NPs was evaluated by comparing the percentage of positive cells and MFI values of cells incubated with NPs with the autofluorescence of cells (Figure 4.31).

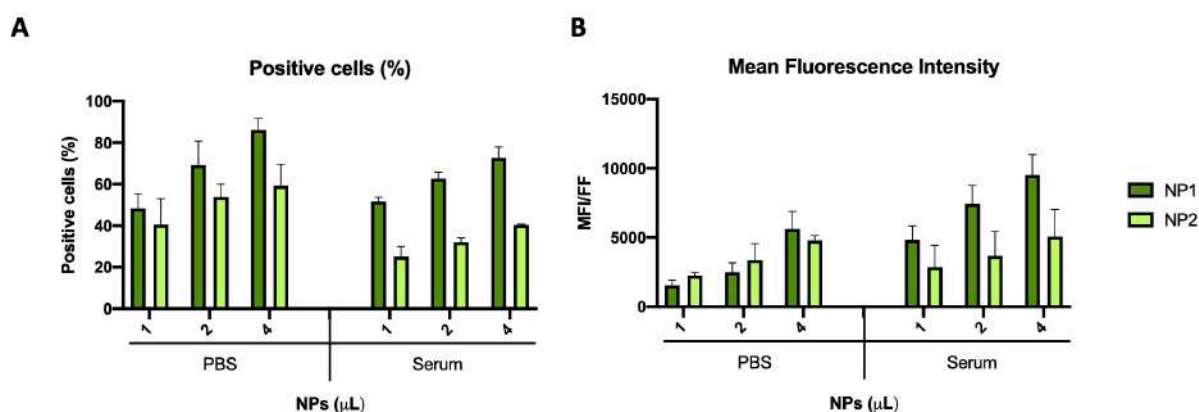


Figure 4.31: Binding/internalization of NPs in malignant B cells. 250,000 Nalm-6 cells were incubated in presence of NHS or not with different amounts (1μL, 2μL and 4μL) of untargeted (NP1) and targeted NPs (NP2) at 37° for 1 hour and analyzed by flow cytometry. (A) The percentage of positive cells and (B) MFI, normalized for the FF, are reported in the histograms. Data have been reported as the mean ± SD.

This analysis suggested a dose-dependent binding, as evidenced in Figure 4.31. In fact, the percentage of positive cells increases in both samples incubated with PBS and Serum in a dose-dependent manner, with a slight more positivity in favor of NP1 (Figure 4.31, A). Moreover, also the MFI increased with the same dose-dependency (Figure 4.31, B), suggesting that higher amounts of NPs, and in particular NP1, are able to interact more with a higher number of cells. The analysis suggested that there are no significant differences between targeted and untargeted NPs, and the targeting mechanism does not seem to increase the binding/internalization. To better evaluate this aspect, cells were analyzed also by confocal microscopy. In particular, cells were incubated with 2μL of NPs in presence of NHS, and later the membranes were

labeled with Fast Dil, and the nuclei with DAPI. For the analysis, two different ROIs were set on pictures: the first one on nuclei, which represents the biggest part of cells, and the other on the membranes. Total NPs (bound and internalized) were counted in the membrane-ROIs, while internalized-NPs were counted in the nuclei-ROIs; the subtraction of internalized from total-NPs resulted in the bound-NPs.

As described in Figure 4.32 (A), there is a slight difference in the samples, even if not significant. In fact, untargeted-NPs that are bound to the membranes are more than targeted-NPs, and parallelly untargeted-NPs that are internalized are less than targeted-NPs. This behavior is clear also in the orthogonal views of confocal pictures, where green-fluorescent NP1 (untargeted-NPs) were localized almost exclusively on the red-fluorescent membrane (Figure 4.32, B), while green-fluorescent NP2

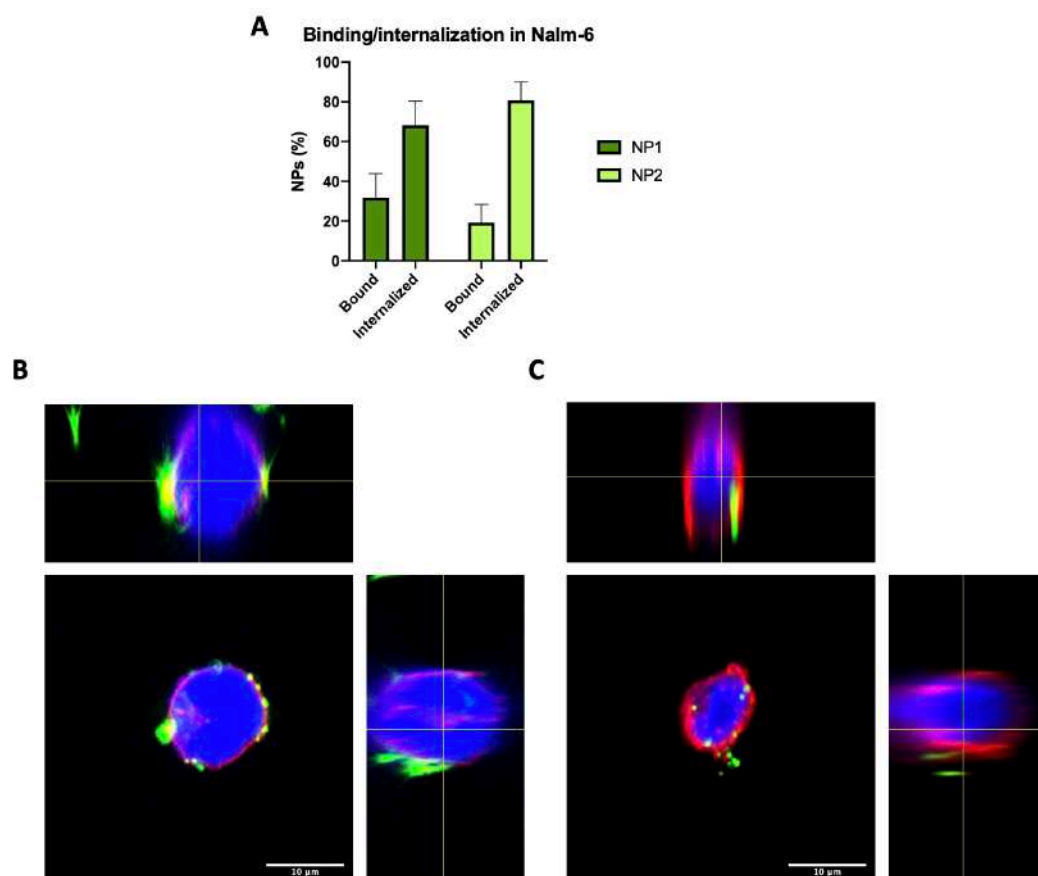


Figure 4.32: Localization of NP inside cells. 250,000 Nalm-6 cells were incubated with 2 μ L of NPs in presence of NHS, membranes were labeled with Fast Dil, and the nuclei with DAPI. **(A)** Total NPs (bound and internalized) were counted with Fiji software in a ROI set on the cell membrane, internalized-NPs were counted in another ROI set on nuclei, and the subtraction of internalized from total-NPs resulted in the bound-NPs. Untargeted-NPs that are bound to the membranes are more than targeted-NPs, and parallelly untargeted-NPs that are internalized are less than targeted-NPs, even if not with a statistical significance. **(B)** green-fluorescent NP1 (untargeted-NPs) are localized almost exclusively on the red-fluorescent membrane, while **(C)** green-fluorescent NP2 (targeted-NPs) are localized both on the red-fluorescent membrane and in the blue-fluorescent-nuclei. Data have been reported as the mean \pm SD.

(targeted-NPs) were localized both on the red-fluorescent membrane and immediately below, inside the cells (Figure 4.32, C).

Regarding the interaction between NPs and cells of the IS, as previously discussed we focused on macrophages and in particular on differentiated Thp-1 cells in order to study NPs elimination. Cells were incubated with increasing amounts of NP1 and NP2 in the presence or not of NHS; samples were analyzed by flow cytometry and the binding/internalization of NPs was evaluated by comparing the percentage of positive cells and MFI values of cells incubated with NPs with the autofluorescence of cells. The analysis demonstrated that both NPs interact in a dose-dependent manner with the same amount of cells (Figure 4.33, A) even if the histogram of MFI values suggests that the number of NPs for single cells remains constant for both NPs in presence of NHS or not (Figure 4.33, B).

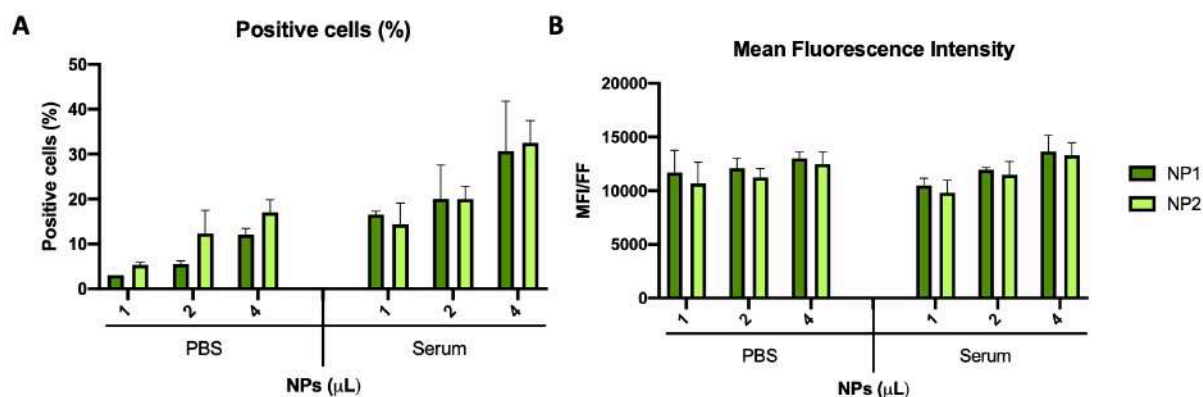


Figure 4.33: Binding/internalization of NPs in macrophages. 100,000 Thp-1 cells were differentiated in macrophages in presence of PMA for 72h, and incubated in presence of NHS or not with different amounts (1μL, 2μL and 4μL) of untargeted (NP1) and targeted NPs (NP2) at 37° for 1 hour and analyzed by flow cytometry. **(A)** The percentage of positive cells and **(B)** Mean Fluorescence Intensity (MFI), normalized for the Fluorescence Factor (FF), are reported in the histograms. Data have been reported as the mean \pm SD.

To better evaluate this aspect, cells were analyzed also by confocal microscopy. Thp-1 membranes were labeled with Fast Dil, and the nuclei with DAPI and two different ROIs were set on pictures, one on nuclei and the other on the membranes to count the total number of NPs (bound and internalized) and the internalized-NPs. As described in Figure 4.34 (A), there is a similar interaction of these cells with these particles, taking into consideration both NPs bound to the membranes and internalized in the cells. This behavior is clear also in the orthogonal views of confocal pictures, where both NPs were localized on the red-fluorescent membrane (Figure 4.34, B and C).

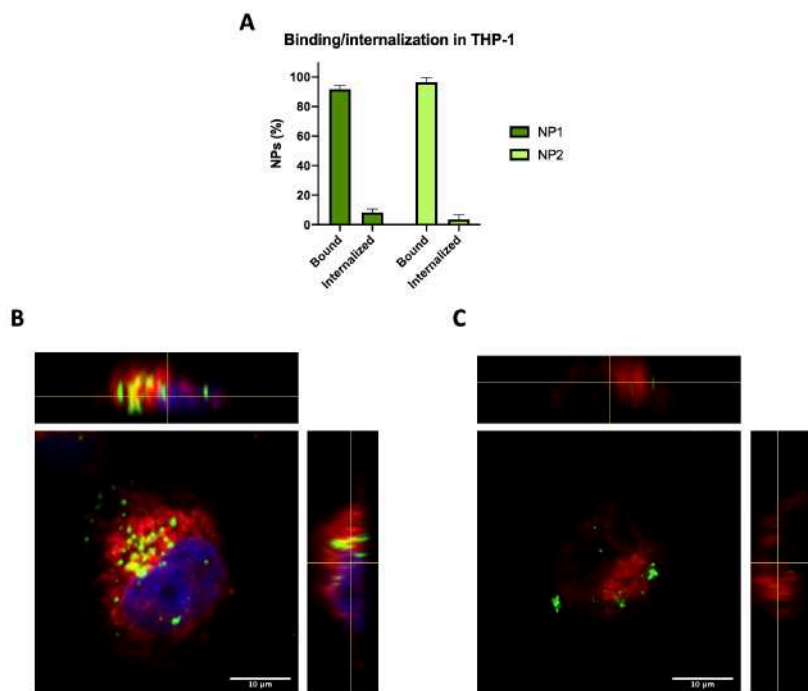


Figure 4.34: Localization of NP inside cells. 100,000 Thp-1 cells were differentiated in macrophages (100ng/mL of PMA) incubated with 2 μ L of NPs in presence of NHS, membranes were labeled with Fast Dil, and the nuclei with DAPI. **(A)** As previously described, with Fiji software were counted the total number of NPs (bound and internalized) and the number of internalized-NPs; the subtraction of internalized from total-NPs resulted in the bound-NPs. Untargeted-NPs that are bound to the membranes are less than targeted-NPs, and parallelly untargeted-NPs that are internalized are more than targeted-NPs, even if not with a statistical significance. **(B)** green-fluorescent NP1 (untargeted-NPs) are localized both on the red-fluorescent membrane and in the blue-fluorescent-nuclei, while **(C)** green-fluorescent NP2 (targeted-NPs) are localized almost exclusively on the red-fluorescent membrane. Data have been reported as the mean \pm SD.

The binding/internalization test of NPs has been repeated also on primary macrophages obtained from monocytes isolated from a healthy donor. The analysis was performed, as previously described, incubating increasing amounts of NPs and analyzing them through flow cytometry.

The percentage of positive cells and their MFI increases in a dose-dependent manner without differences between targeted and untargeted NPs (Figure 4.35, A and B), showing that the targeting agent bound on the surface of NP2 does not enhance phagocytosis by macrophages, at least in this *in vitro* setting.

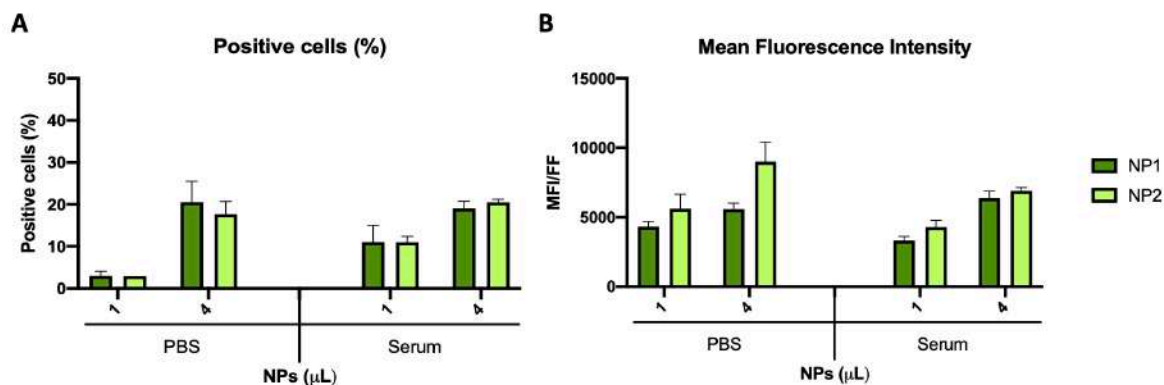


Figure 4.35: Binding/internalization of NPs in macrophages isolated from donor's blood. White cells were isolated and then macrophages were segregated by consecutive selections of adherent cells. 100,000 cells were incubated in presence of NHS or not with different amounts (1 μ L, and 4 μ L) of untargeted-NPs (NP1) and targeted-NPs (NP2) at 37° for 1 hour and analyzed by flow cytometry. (A) The percentage of positive cells and (B) the MFI, normalized for the FF, are reported in the histograms. Data have been reported as the mean \pm SD.

4.2.3.2.4 Evaluation of NPs toxicity

Firstly, *in vitro* tests were performed to evaluate the actual toxicity of the nano-delivery system in tumor B-cells. For this purpose, a viability assay was performed on both Nalm-6 cells using NP1 and NP2. Specifically, cells were incubated with 2 μ L of NP1 and NP2 for 48 hours. Samples were then analyzed by evaluating the OD at 570nm (Figure 4.36). Data analysis suggests that both NPs are not toxic for cells; rather nano-systems seem to increase cell viability confirming the literature. In fact, in literature, it is described that in many situations albumin may offer improved cell performance, promoting cell growth and maintaining a variety of eukaryotic cells

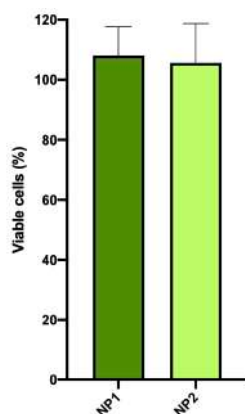


Figure 4.36: Toxicity evaluation of NP on malignant B-cells. 200,000 Nalm-6 cells were incubated with 2 μ L of untargeted- (NP1) and targeted-NPs (NP2) for 48h. The viability of cells was evaluated analyzing the OD at 570nm. Data have been reported as the mean \pm SD.

under *in vitro* culture environment [173, 174]. Moreover, albumin also scavenges the reactive oxygen species that are harmful to cell survival, by binding to the metal ions and limiting the ability of these ions to participate in the ROS generation [174].

In conclusion, NP1 and NP2 demonstrated to be safe and capable to interact with ALL cells, encouraging the introduction of *in vivo* studies to

evaluate the effective binding ability of NPs in a complex biological system.

4.2.3.3 *In vivo studies*

Targeted and untargeted NPs were compared to investigate their behavior in an *in vivo* model. The transgenic line of zebrafish Tg(mpeg1:mCherry) was initially used to investigate the *in vivo* biodistribution, analyzing if there are modifications in the engulfment of NPs by macrophages, and, in subsequent studies, also to verify the efficacy of the targeting mechanism in the reaching of the target on cancer B-cells in a new model of human cells in zebrafish larvae.

4.2.3.3.1 *Elimination studies in healthy zebrafish larvae*

NP1 or NP2 were injected in the duct of Cuvier of Tg(mpeg1:mCherry) transgenic line of zebrafish and the analysis was performed 24hpi. In particular, a ROI was drawn in the tail of the zebrafish and the CTCFs of red-fluorescent-macrophages, green-fluorescent-NPs, and the co-localized areas were analyzed. Data demonstrated that NP1 are significantly less engulfed by macrophages than NP2 (Figure 4.37), suggesting that targeted-NPs can be opsonized *in vivo*, probably for the presence of anti-CD19 recombinant antibody, and result less concealed to the IS, confirming what was obtained *in vitro*.

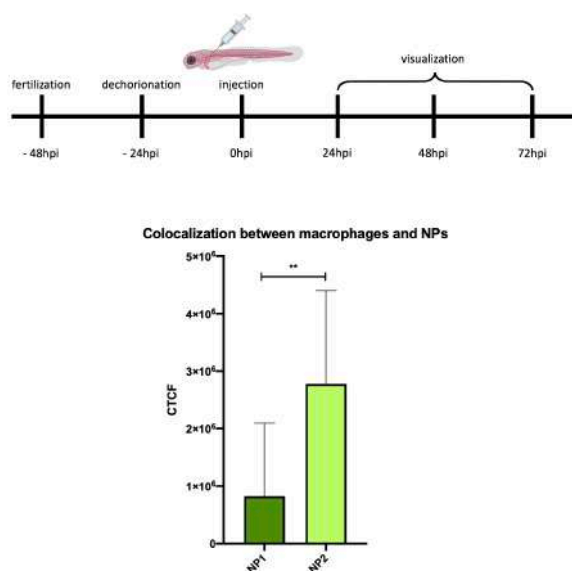


Figure 4.37: Co-localization between macrophages and NPs. (A) Timeline of experimental procedure. (B) Data analysis of the CTCF of the co-localized areas normalized for the FF of NPs. All data report as the mean ± SD. $P \leq 0.01 = **$.

4.2.3.3.2 *Creation of the tumor-bearing zebrafish model*

NP2 are characterized by the presence of the targeting mechanism on the surface, which is an anti-CD19 scFv-Fc able to recognize CD19⁺ cells, such as ALL cells. It was also previously demonstrated the ability of the scFv-Fc, alone or bound on the surface of PLGA-PVA NPs, to target Nalm-6 cells *in vitro*. However, for this kind of

nano-system, there is the need to deeply investigate its behavior in a more complex system, such as an animal model, and again were employed the Tg(mpeg1:mCherry) transgenic line of zebrafish. Nalm-6 (500 cells) (labeled with a near-infrared fluorescent dye) were injected 48hpf in the duct of Cuvier and followed over time.

As shown in Figure 4.38 (A) Nalm-6 cells were broadly distributed in the body of zebrafish, with a preferential accumulation in the PBI. Moreover, at 24hpi was analyzed the CTCF of near-infrared fluorescent areas in three different groups (in which zebrafish were randomly assigned), demonstrating a uniform variability of the groups (Figure 4.38, B).

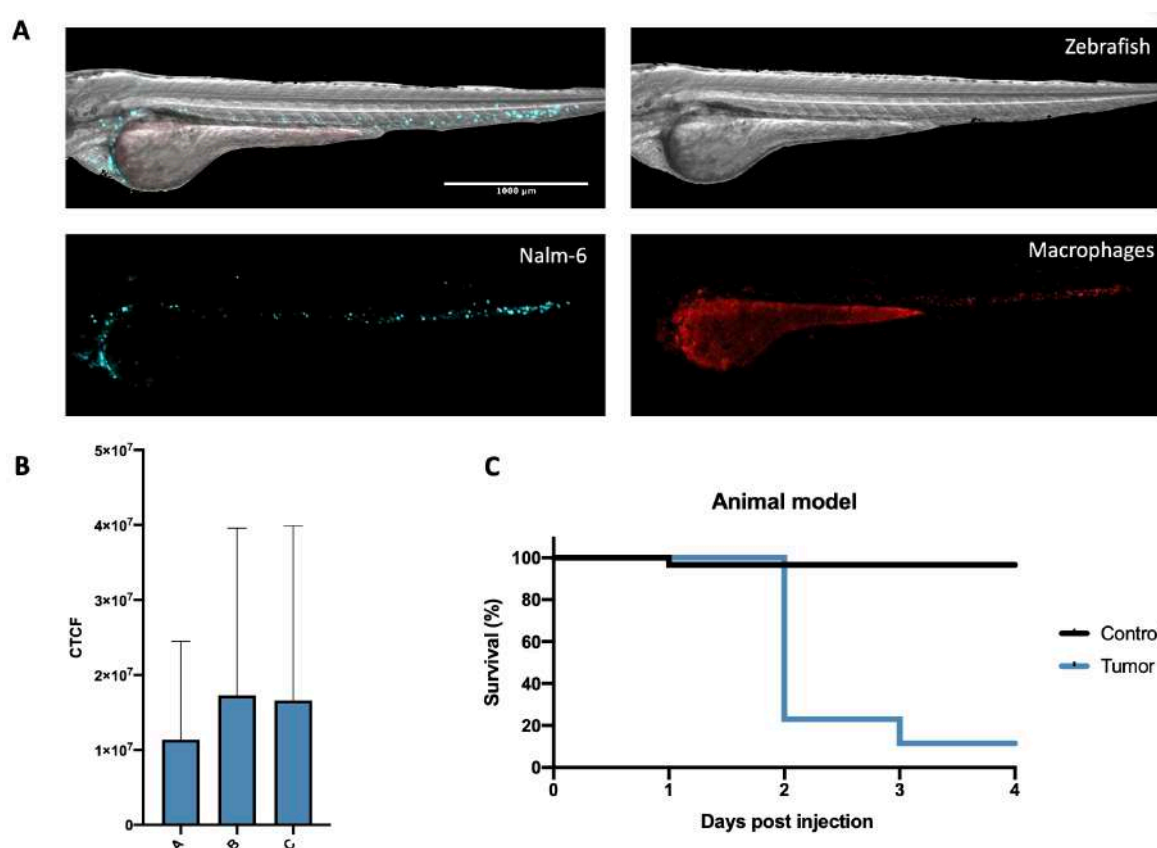


Figure 4.38: Setting up of the animal model. (A) 500 Nalm-6 cells, labelled with Fast DiD (near-infrared fluorescent dye, lower left panel) were injected 2dpf in the duct of Cuvier of Tg(mpeg1:mCherry) transgenic zebrafish (upper right panel), which possess red-fluorescent macrophages (lower right panel). (B) Data analysis of the CTCF of the near-infrared-fluorescent areas (Nalm-6 cells) of zebrafish randomly assigned to three different groups, suggesting that the three groups received the same amount of cells. (C) Zebrafish (nControl=30, nTumor=30) received Nalm-6 cells (500). Animal survival was represented as Kaplan Mayer curve. Data have been reported as the mean ± SD. Control vs tumor: **** P-value <0.0001.

Finally, the survival was analyzed, comparing 30 control zebrafish and 30 cell-receiving zebrafish. The Kaplan Mayer curve (Figure 4.38, C) shows that the 80% of zebrafish that received cells do not survive more than 2 dpi, while, at the end of the

study (5dpf), only 3 larvae survived, demonstrating the possibility to use this parameter as an endpoint in this setting.

4.2.3.3.3 Biodistribution studies in tumor-bearing zebrafish larvae

The human/zebrafish model was employed to study the biodistribution of NPs. Briefly, as described in Figure 4.39, zebrafish of the Tg(mpeg1:mCherry) transgenic line received Nalm-6 cells into the duct of Cuvier, and NPs were then injected via the same route.

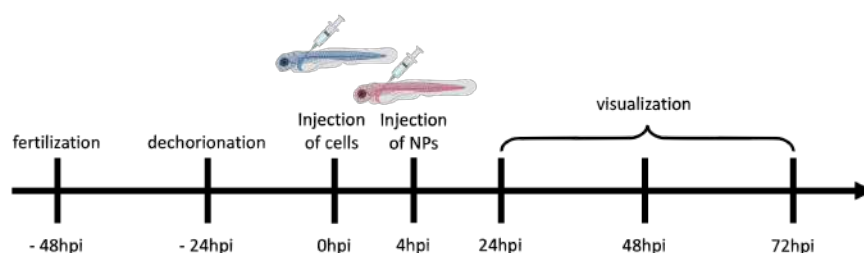


Figure 4.39: Experimental timeline. 500 cells/zebrafish were injected in the duct of Cuvier of previously (-24hpi) dechorionated embryos, and 4hpi of cells, 4,6nL of untargeted- or targeted-NPs were injected again in the duct of Cuvier. Zebrafish were analyzed immediately after the second injection and after 24h through fluorescence microscopy.

Zebrafish were analyzed through fluorescence microscopy immediately after the second injection and the analysis started 24hpi.

As described before, a ROI was set in the tail of zebrafish (Figure 4.40, A) and different CTCFs were analyzed.

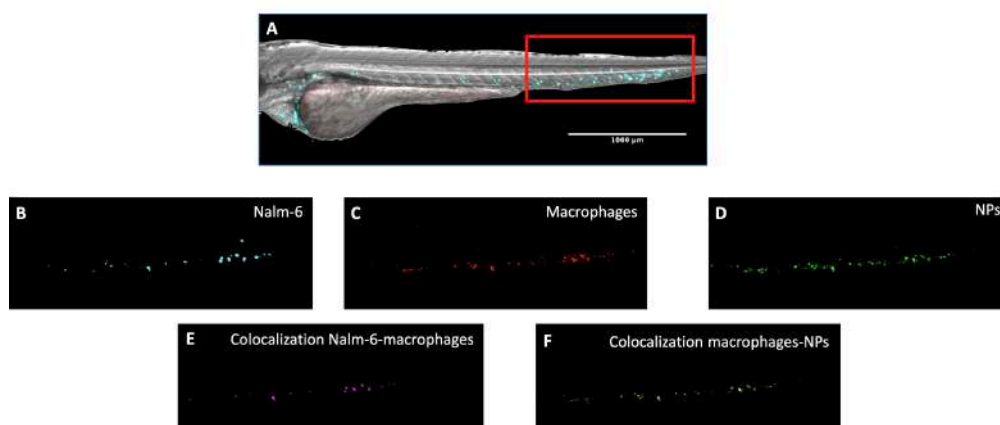


Figure 4.40: Co-localization analysis. (A) A ROI was set in the tail of zebrafish and the CTCF of (B) Nalm-6 cells (cyan), (C) macrophages (red), (D) NPs (green), was analyzed. After, signals of the co-localization between (E) cells and macrophages (purple), and between (F) macrophages and NPs (yellow) were extrapolated and quantified.

Cell (near-infrared, Figure 4.40, B), macrophages (red, Figure 4.40, C), and NPs (green, Figure 4.40, D) fluorescences were visualized, and cells / macrophages (purple, Figure 4.40, E) and macrophages / NPs (yellow, Figure 4.40, F) co-localization signals were then extrapolated.

Biodistribution data (Figure 4.41, A), expressed as a percentage of NPs localized in the various districts, indicated that at 24hpi the majority of the injected NPs, both untargeted (NP1) and targeted-NPs (NP2), were still in the bloodstream (Figure 4.41, B) and available to interact with the target, while less than 35% of injected NPs were phagocytosed by macrophages in zebrafish (Figure 4.41, C). On the other hand, the remaining NPs were co-localized with Nalm-6 cells with a significant difference in favor of targeted NPs with respect to untargeted NPs (NP2 and NP1, respectively, Figure 4.41, D), highlighting the importance of the targeting mechanism also in this *in vivo* setting, to enhance NPs accumulation in tumor cells.

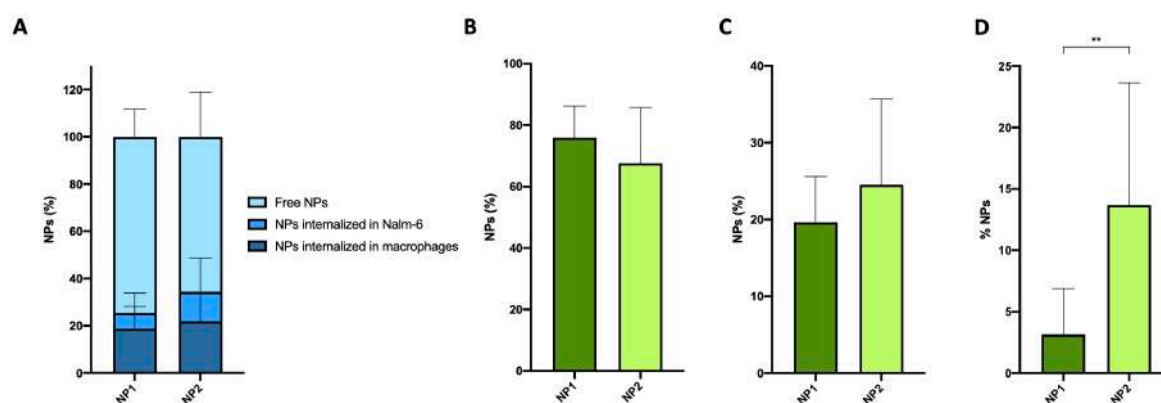


Figure 4.41: Biodistribution studies in tumor-bearing zebrafish. (A) Data analysis of the biodistribution expressed as a percentage of NPs localized in the various districts analyzed. (B) Comparison of the percentage between NP1 and NP2, not yet internalized by cells or macrophages. (C) The percentage of the macrophages' internalization of NP1 or NP2. (D) The percentage of the internalization of NP1 or NP2 in tumor B-cells. All data report as the mean \pm SD. $P \leq 0.05 = **$.

The biodegradable PLGA-PVA shell is demonstrated to be safe; the HSA coating is demonstrated to be able to modify the PC on the surface of nano-devices, allowing a minor engulfment by macrophages and so consenting to the NPs to be available to reach their target for an increased period of time; in addition, the efficacy of the targeting mechanism was proved to reach the target, also in an *in vivo* setting.

All these results encourage us to investigate the last step, filling the NPs with a drug and verifying their therapeutic efficacy.

4.2.4 Developing the nanoparticles' core

The major goal of nanomedicine is represented by the possibility of treating selectively a disease with no side effects, with the aid of a nano-device, which can reach the diseased tissue and release its content and execute its function. In particular, a drug can be encapsulated inside a nano-device, which through a targeting ligand transports the whole amount of the drug to its final destination, where it can be released, while they minimize systemic exposure that causes side effects while enhancing drug efficacy. In this way, side effects that characterized the traditional administration routes (e.g. oral or i.v.) can be avoided, increasing, at the same time, the circulation time of drugs in blood and the ability of drugs to reach their sites of action [69].

For what concerns the treatment of ALL, anthracyclines are a well-known class of chemotherapeutics, that acts mainly by intercalating DNA and interfering with DNA metabolism and RNA production. Two major dose-limiting toxicities of anthracyclines include myelosuppression and cardiotoxicity [144]. The PEGylated liposomal doxorubicin formulation “Doxil” was the first FDA-approved liposome chemotherapeutic agent in 1995. It has shown highly selective tumor localization and excellent pharmacokinetic properties in clinical applications.

Starting from this point, anthracyclines were chosen as candidates to be encapsulated inside nano-devices. Among anthracyclines, doxorubicin is widely used, however, its clinical use is restricted due to the severe risk to develop cardiotoxicity [144]. To avoid or minimize this problem, several anthracyclines derivatives were introduced, and idarubicin is one of them [175]. It was initially studied in the '90s, demonstrating an increased therapeutic index if compared to doxorubicin. As control was chosen another well-known chemotherapeutic: docetaxel. This is in the taxane family of medications; it interferes with the normal function of microtubules, thereby stopping cell division, but is not commonly active in hematological malignancies.

On these bases, these mentioned drugs were tested on B-cells to assess which was the best candidate to be loaded inside NPs, without taking into consideration their side effect but only their cytotoxicity.

4.2.4.1 In vitro evaluation of the most effective drug-NP couple

Doxorubicin, idarubicin, and docetaxel were initially tested in a viability assay to verify which drug was the most effective in tumor B-cell cytotoxicity. Briefly, B-cells were

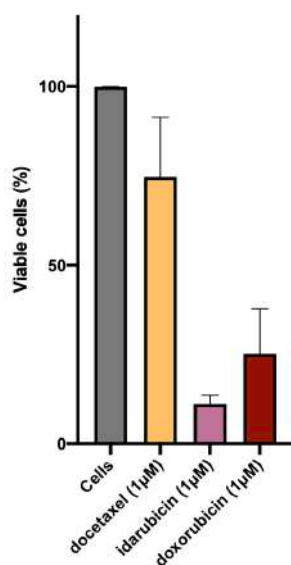


Figure 4.42: Viability assay after incubation with free drugs. 200,000 Bjab cells were incubated with different free-drugs (doxorubicin, idarubicin, or docetaxel, 1 μM final concentration) for 48 hours. Samples were then analyzed by evaluating the OD at 570nm. Data have been reported as the mean ± SD.

incubated with the drug and cell viability was then assessed. As shown in Figure 4.42, docetaxel does not have a relevant toxic effect on Bjab cells, while idarubicin and doxorubicin were able to affect more than 75% of cells. Between the last two preparation, idarubicin seems to be more effective but the loading process showed that doxorubicin was better encapsulated than idarubicin in the NPs (data not shown). For these reasons, Doxorubicin has been chosen and loaded in new NPs preparations.

PLGA-PVA NPs, loaded with doxorubicin, were produced and tested in a viability assay (Figure 4.43). Bjab cells were incubated with the free doxorubicin (and compared to cells incubated with NP0 (empty, uncoated, and untargeted NPs) or NP3 (doxorubicin-loaded, uncoated, and untargeted NPs). As evidenced in Figure 4.43 the efficacy of doxorubicin-loaded NPs was comparable to that obtained with the free drug and in parallel, it was demonstrated that this effect was obtained due to the encapsulated drug since NP0 do not affect cells viability.

PLGA-PVA NPs filled with doxorubicin were produced with or without covalently-linked albumin-coating (NP3 and NP4, respectively) and with both albumin-coating and anti-CD19 targeting mechanism (NP5) and characterized *in vitro*. NPs showed round shapes and sizes lower than 400 nm and a negative surface charge. The average diameter,

incubated with the drug and cell viability was then assessed. As shown in Figure 4.42, docetaxel does not have a relevant toxic effect on Bjab cells, while idarubicin and doxorubicin were able to affect more than 75% of cells. Between the last two preparation, idarubicin seems to be more effective but the loading process showed that doxorubicin was better encapsulated than idarubicin in the NPs (data not shown). For these reasons, Doxorubicin has been chosen and loaded in new NPs preparations.

PLGA-PVA NPs, loaded with doxorubicin, were produced and tested in a viability assay (Figure 4.43). Bjab cells were incubated with the free doxorubicin (and

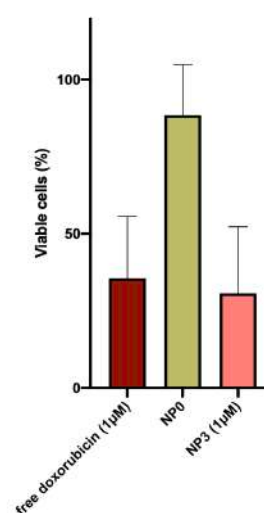


Figure 4.43: Viability assays after incubation with loaded-NPs. 200,000 Bjab cells were incubated with free-doxorubicin (1 μM) or NP3 (1 μM final concentration of drug), or the same amount of NP0 for 48 hours. Samples were then analyzed by evaluating the OD at 570nm. Data have been reported as the mean ± SD.

| Name | NP3 | NP4 | NP5 |
|-----------------------|-------------|--------------|---------------|
| Average diameter (nm) | 201.53±1.37 | 381.50±41.72 | 489.25±244.59 |
| PDI | 0.12±0.02 | 0.51±0.15 | 0.53±0.17 |
| Zeta potential (mV) | -0.27±0.11 | 0.17±0.12 | -0.22±0.06 |

Figure 4.44: Characterization of targeted-NPs. Physicochemical characteristics of NPs formulations.

be a bit bigger (489.25 ± 244.59) with a slight negative charge of -0.22 ± 0.06 .

Loaded- and coated-NPs were tested in a viability assay (Figure 4.45). Nalm-6 cells were incubated with the free doxorubicin and compared to cells incubated with NP0 (empty, uncoated, and untargeted NPs) or loaded-NPs: NP3 (doxorubicin-loaded, uncoated, and untargeted NPs), NP4 (doxorubicin-loaded, HSA-coated, and untargeted NPs), and NP5 (doxorubicin-loaded, HSA-coated, and targeted NPs). As evidenced in Figure 4.45 the efficacy of doxorubicin-loaded NPs was maintained any was the agents were covalently bound on the surface.

polydispersity index (PDI), and zeta potential values of the different types of NPs are reported in Figure 4.44. These data underline the fact that the coating addition demonstrated a slight increment of the dimension (from $201.53\pm 1.37\text{nm}$ to $381.5\pm 41.72\text{nm}$) and a slender increment of the negative charge which moves to 0.17mV . However, targeted-NPs demonstrated to

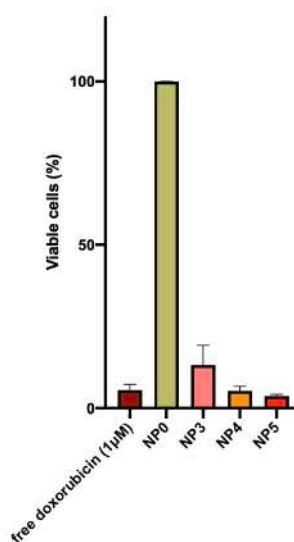


Figure 4.45: Viability assays after incubation with loaded-NPs. 200,000 Nalm-6 cells were incubated with free-doxorubicin ($1\mu\text{M}$) or doxorubicin loaded-NPs (NP3, NP4, NP5, $1\mu\text{M}$ final concentration of drug), or the same amount of NP0 for 48 hours. Samples were then analyzed by evaluating the OD at 570nm. Data have been reported as the mean \pm SD.

4.2.4.2 Evaluation of the therapeutic effect of loaded-NPs

In vivo experiments are strongly needed to verify NPs' behavior in a complex environment and the optimal way to assess the efficacy of loaded-NPs is represented by observation of the tumor growth arrest and a reduction of its volume. A diffused model of ALL is obviously a more realistic scenario, however, to better quantify the effect of loaded-NPs a localized one is recommended. Therefore, an ALL xenograft model was developed on WT zebrafish embryos.

4.2.4.2.1 Xenograft zebrafish models

Firstly a localized xenograft model was set up to easily verify if the tumor dimension can be easily determined through the fluorescent signal given by the fluorescent-labeled cells. In particular, B-cells were labeled with the calcein-AM (Figure 4.46, A), which is a cell-permeant dye that can be used to determine cell viability in most eukaryotic cells. In live cells, the non-fluorescent calcein-AM is converted to red-fluorescent calcein (ex/em 577/590 nm), after acetoxymethyl ester hydrolysis by intracellular esterases. Therefore, 48hpf, 500 Calcein-AM labeled Nalm-6 were injected in the perivitelline space (at the margin between the yolk sac and the embryonic cell mass), resulting in the localization of tumor cells in the ventral thoracic area (Figure 4.46, B).

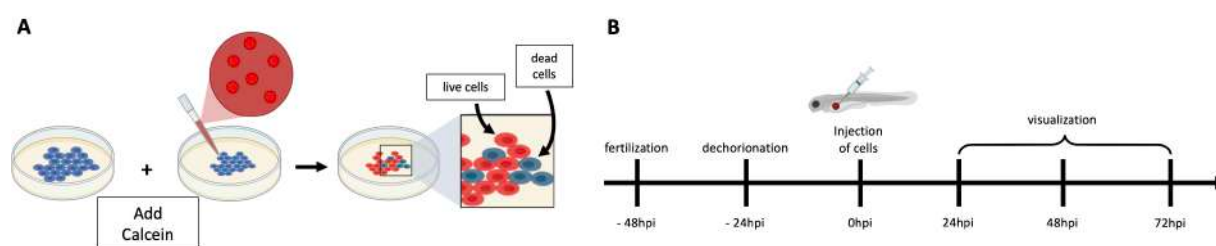


Figure 4.46: Localized xenograft zebrafish model. (A) Nalm-6 cells were labeled with Calcein-AM, which is a cell-permeant dye, used to determine cell viability. After the addition of Calcein-AM, the non-fluorescent Calcein-AM is converted in living cells to red-fluorescent Calcein. (B) Timeline of the experimental procedure.

Zebrafish were followed over time and the red-fluorescent Calcein-AM was analyzed through fluorescence microscopy (Figure 4.47), immediately after cells' injection (Figure 4.47, left panels), 24hpi (Figure 4.47, central panels), and 48hpi (Figure 4.47, right panels). The tumor mass does not lose fluorescence over time, indicating that cells are still alive, and it is selectively localized in the flank of the zebrafish, over the yolk sac, and do not move through the zebrafish body.

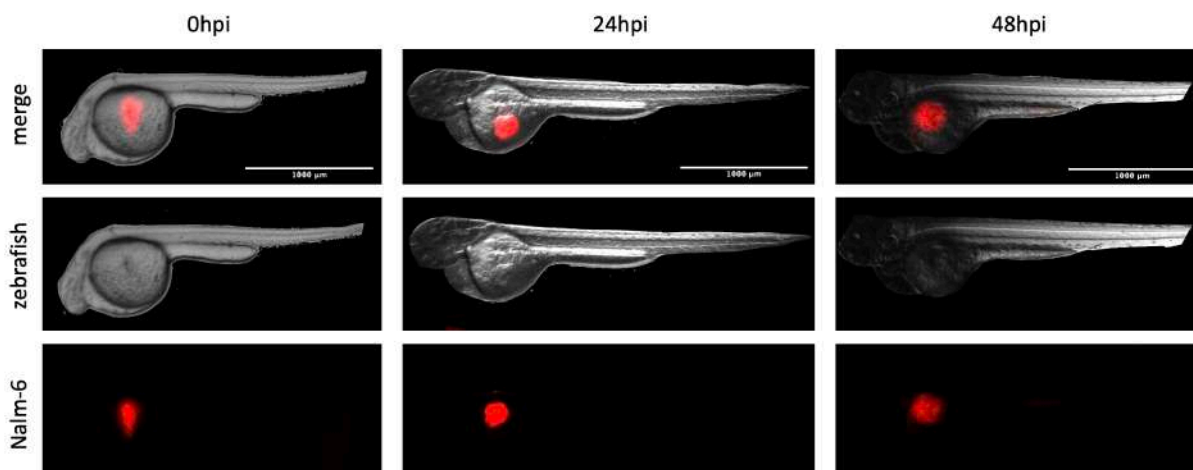


Figure 4.47: Setting up of a localized model of B-cell malignancies. 500 Nalm-6 (labeled with red-fluorescent Calcein-AM) were injected at 48hpf in the perivitelline space of zebrafish. Zebrafish were analyzed immediately after the injection (left panels), 24 hpi (central panels), and 48hpi (right panels).

Since ALL is a hematological disease a localized model of the pathology is not totally realistic. Therefore, a diffuse one was set up, and 48hpf, 500 Calcein-AM labeled Nalm-6 were injected into the duct of Cuvier, resulting in the localization of tumor cells in the blood vessels of the embryo. Cells' fluorescence was observed in the whole body of the zebrafish until the endpoint at 48hpi (Figure 4.48).

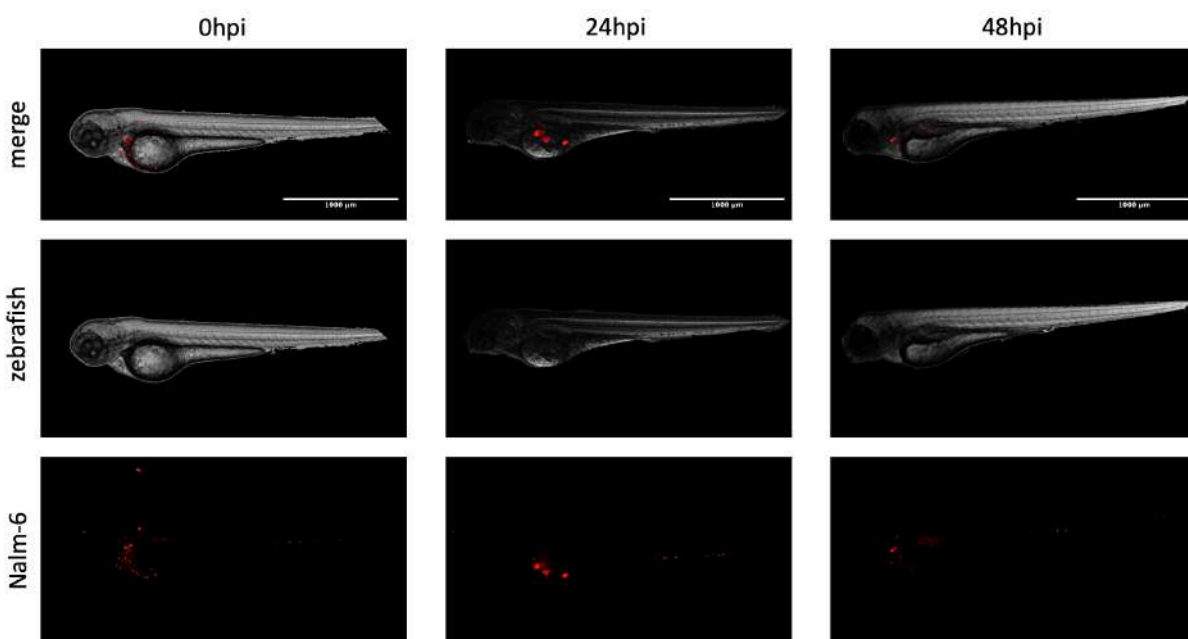


Figure 4.48: Setting up of a diffused model of B-cell malignancies. 500 Nalm-6 (labeled with red-fluorescent Calcein-AM) were injected at 48hpf in the duct of Cuvier of zebrafish. Zebrafish were analyzed immediately after the injection (left panels), 24 hpi (central panels), and 48hpi (right panels).

4.2.4.2.2 *In vivo* NPs efficacy

Finally, the therapeutic efficacy of this nano-system was evaluated in a diffused model of B-cell malignancy to verify if targeted-loaded-NPs were able to reach the target and execute their assignment. The previously set up model of diffused ALL was developed in the Tg(fli1:EGFP) transgenic line of zebrafish, which is characterized by green fluorescent blood vessels. Red-fluorescent Nalm-6 were injected into the duct of Cuvier of zebrafish embryos and, after 4h, free doxorubicin or NP5 (targeted-, doxorubicin-loaded-NPs) were injected into the duct of Cuvier. Zebrafish were analyzed immediately after the injection of NPs (Figure 4.49, A, upper panels) and 24hpi (Figure 4.49, A, lower panels) through fluorescence microscopy. As shown in Figure 4.49 (A) Nalm-6 cells were initially localized into the whole body of the fish, and this signal was almost abolished 24h later.

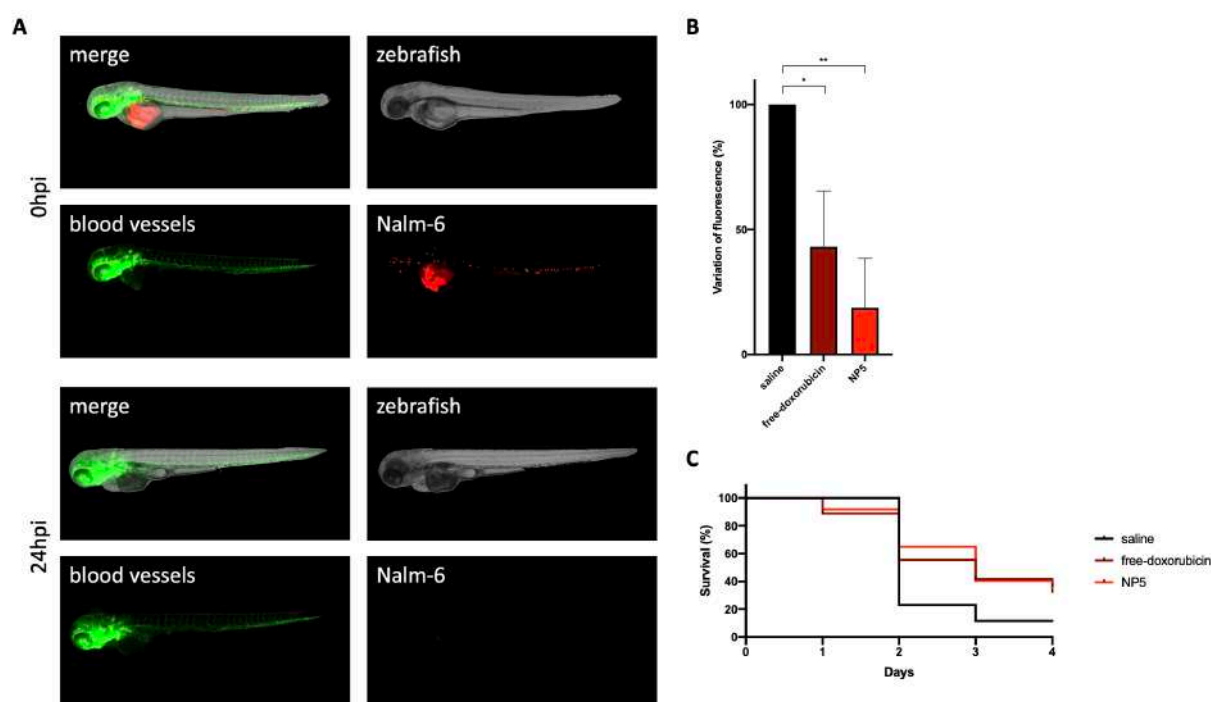


Figure 4.49: Therapeutic effect of NP5 in a diffused model of B-cell malignancy. (A) 48hpf, 500 Nalm-6 (labeled with red-fluorescent Calcein-AM) were injected through the duct of Cuvier in the blood-vessels (green fluorescence) of zebrafish embryos, and after 4h, 4,6nL of free-doxorubicin or NP5 (targeted-, doxorubicin-loaded-NPs) were injected in the duct of Cuvier. Zebrafish were analyzed immediately after the injection of NPs (upper panels) and 24hpi (lower panels) through fluorescence microscopy. (B) Data analysis of the variation of cells' fluorescence after treatment with free-doxorubicin or NP5 expressed as percentage. All data report as the mean \pm SD. $P \leq 0.05 = *$; $P \leq 0.01 = **$. (C) Zebrafish (nSaline=26, nFree-doxorubicin=37, nNP5=36) received Nalm-6 cells (500) and 4h later, 4,6nL of saline or free-doxorubicin or NP5. Animal survival was represented as Kaplan Mayer curve. Saline vs free-doxorubicin: * P-value <0.1; saline vs NP5: * P-value <0.1.

As performed before, the CTCF was calculated at 0hpi and compared to the CTCF at 24hpi (Figure 4.49, B); the variation of the fluorescent signal demonstrated that free-

doxorubicin was able to arrest cell growth, significantly decreasing the red-fluorescent signal of cells in comparison to zebrafish treated with saline. More interestingly, this result was even more evident in zebrafish treated with NP5. In addition, zebrafish's survival was observed for the next 3dpi (five days in total, according to the ministerial approval 04086.N.SGL, Figure 4.49, C) and, at the end of the study, tumor-bearing zebrafish treated with free-drug or NP5 demonstrated a comparable, between treatments, ~30% of survival more than zebrafish's treated with the saline.

These data put the basis for further studies in more complex animal models of B-cell malignancies, such as in mice. However, all these results together, already highlighted that PLGA-PVA NPs targeted with anti-CD19 antibodies and filled with doxorubicin represent a promising approach for the treatment of B-cell malignancies, but also for other pathologies. In fact, PLGA-PVA NPs result biodegradable and therefore safe; moreover, the albumin coating conceals the nano-devices from the IS prolonging NPs' circulating time and the targeting mechanism ensures the reaching of the objective, potentially decreasing off-target effects. Additionally, these nanostructures can be imagined as a nano-platform in which the single components, such as the payload or the targeting mechanism, can be replaced to achieve different goals.

5. Conclusions

The major public health problem worldwide is represented by cancer and it is still the second leading cause of death in the United States, even if in 2020 the diagnosis and treatment of cancer were hampered by the coronavirus disease 2019 (COVID-19) pandemic [1]. Among children and adolescents, “Cancer is a leading cause of death” according to the WHO (World Health Organization 2021); leukemia is the most common childhood cancer (28% of cases) and, globally, ALL is the most common childhood cancer (19% of total childhood cancer incidence), followed by BL (5%).

For these reasons, this Ph.D. project was focused on the preclinical development of targeted NPs as novel approaches for the treatment of BL and ALL.

BL is often characterized by the expression of high levels of miRNA-17, which is part of the miRNA-17~92 cluster. This is involved in the tumor-genesis of different tumors, including B-cell malignancies, and its up-regulation entails the inhibition of some oncosuppressor genes. Particularly, among the miRNAs belonging to the miRNA-17~92 cluster, miRNA-17 targets a large number of genes and it can control their expression with antagonizing functions, e.g. promoting or suppressing cell cycle progression. In collaboration with Dr. Bomben's (C.R.O. Aviano) group, an oligonucleotide (AntagomiR-17) capable of pairing and defeating miRNA-17 was produced, and it was demonstrated to affect B cells' growth *in vitro* and *in vivo*. However, this oligonucleotide is not specific to malignant cells, and because of its small dimension, it is rapidly eliminated by kidneys. Therefore, chitosan-NBs, produced by the group of Prof. Roberta Cavalli (University of Turin) were tested as vehicles to protect and deliver the molecule directly to malignant B-cells, thanks to the targeting mechanism present on the surface of these nano-systems. Firstly, NBs were characterized *in vitro* for dimensions and shape, and then for their interaction with blood components. In fact, when injected into the bloodstream, foreign structures interact with more than 3000 proteins, cells, and structures [100]. NBs demonstrated to significantly reduce the coagulation half time and also the activity of the CS, showing potential causes of side effects. At the same time, their interaction with malignant B-cells demonstrated that the targeting mechanism enhances their internalization. As a consequence, it is possible to increase the delivery of the material using targeted NB-loaded; the evaluation of the effect of AntagomiR-17

confirmed the binding and the internalization, leading to the transport of AntagomiR-17 inside cells, with a consequent cytotoxic effect due to the down-regulation of miRNA-17 levels, putting the basis for *in vivo* studies. Biodistribution studies on healthy mice reveal that NBs were eliminated through the liver-bile-intestine-excretion pathway, and these nano-structures were not localized into the brain, heart, or other organs of the MPS. Moreover, an unexpected presence of NBs in the kidneys was observed, probably due to the positive charge of NBs, which induced their interaction with the negatively charged glomerular membrane of the kidneys [160]. Biodistribution studies performed in tumor-bearing mice demonstrated the presence of NBs in the tumor mass, even if the targeting agent seems not to have a significant effect. On the contrary, NB1 (AntagomiR-17-loaded nanoparticles without a targeting agent) were ineffective, showing similar tumor growth with respect to saline-treated mice. To demonstrate that the therapeutic effect was due only to the presence of AntagomiR-17 and it was not dependent on the anti-CD20 antibody or polymers, the *in vivo* experiments were repeated in a second human/mouse model of B-cell malignancy, but animals were challenged with a specific population of Mec-1 cells, expressing low levels of miRNA-17. In this context, the effect of NB3 was completely abolished and the development of the tumor mass was not different from saline-treated mice.

These data showed that chitosan-based NBs developed in this study represent a promising tool in the treatment of BL, even if in the potentiality of this nano-platform there are some limitations, shown *in vitro* studies and in biodistribution analysis. In addition, B-cell malignancies can be distinguished through the expression of characteristic surface antigens that reflect the developmental stages in which the pathology occurs; ALL, for example, originates from early-stage cells that do not possess the CD20 antigen, suggesting employing another targeting mechanism able to address a wider class of B-cell malignancies.

All these features prompt us to take in consideration and develop another nano-platform, potentially able to overcome these limitations, characterized by a different targeting agent, a negative charge and the possibility to modify surface properties.

Starting from these considerations, PLGA-PVA are FDA-approved polymers chosen as substitutes of chitosan for the nano-platform structure. PLGA is a copolymer consisting of two different monomer units, poly(glycolic acid) (PGA) and poly(lactic

acid) (PLA) linked by ester bonds; its success is particularly related to its continued drug release compared to conventional devices, associated to minimal systemic toxicity. Poly(vinyl alcohol) (PVA) is frequently used as an emulsifier in the formulation of PLGA-NPs, due to its ability to form an interconnected structure with the PLGA, helping to achieve a uniform and small NPs [88]. The negative charge of the PLGA is also crucial in its activity, influencing the interaction with plasma protein and cells [86]. We hypothesize that a pre-formed, covalently-bounded, protective albumin-corona should limit non-specific interactions with plasma proteins, contributing to decreasing the activation of the complement system, the opsonization of the nano-systems, and the interaction with immune cells that cause a rapid elimination. In fact, albumin has a role in the PC as dysopsonin and hence contributes to reducing the bond and absorption of the other plasma proteins responsible for the MPS uptake.

PLGA-PVA NPs were produced with or without covalently-linked albumin coating (NP1 and NP0, respectively), and then characterized to evaluate the shape, dimensions, and charge. The coating addition demonstrated a slight increment of the dimension (from $322.4 \pm 3.71 \text{ nm}$ to $348.7 \pm 4.43 \text{ nm}$) and a slender reduction of the negative charge. Differences in the PC formation on NPs were investigated in collaboration with Prof. Marcello Manfredi (University of Piemonte Orientale), analyzing the presence of specific proteins and their abundance: 48 proteins (31.37%) interact and remain specifically bound on the surface of NP0, 79 proteins (48.37%) interact with NP1, and 31 proteins (20.26%) associate with both preparations. Dysopsonins are more adsorbed on the surface of the NP1 (albumin-coated NPs) but, in general, there are proteins both in the coagulation cascade and the complement system on NP0 and NP1. Covalent-bound albumin NPs did not cause mechanical disruption of red blood cells, not influenced the half coagulation time, but, for both preparation (NP0 and NP1) it was demonstrated a slight reduction of the CS activity, confirming mass spectrometry data showing the adsorption of CS proteins on the surface of nanoparticles.

Since the coating with HSA was introduced with the aim to avoid macrophages' engulfment, NPs were then tested on primary macrophages isolated from a donor's blood, demonstrating that the presence of HSA-coating prevents the interaction of NPs with macrophages and confirming the initial hypothesis that the stable coating with HSA is able to influence the characters of the PC on NPs after the injection in the

bloodstream and potentially prolong NPs' circulation time, due to the difference in opsonins/dysopsonins balance in the PC.

In vitro results were confirmed *in vivo*. Zebrafish were chosen as animal models for biodistribution studies; data analysis highlighted differences in the accumulation of the different NPs preparations, in particular focusing on posterior blood island (PBI), known to be a macrophages' rich area [172]. To clarify this aspect, the transgenic line of zebrafish Tg(mpeg1:mCherry) was acquired because of the expression of a fluorescent signal linked to the *mpeg1* gene in macrophages [167]. This approach demonstrated that NP1 were significantly less engulfed by macrophages than NP0. The result is consistent with what was previously obtained *in vitro* with healthy donor' white cells, highlighting again the importance of the HSA-coating on the surface of NPs to conceal nano-structures from the IS and to increase their bioavailability.

Albumin-coated PLGA/PVA polymeric NPs represent our nano-platform for future studies of drug delivery in cancer microenvironment; to specifically address B-cell malignancies a different tumor-associated antigen was chosen to produce the targeting mechanism of NPs. CD19 is a 95-kDa member of the Ig superfamily and is expressed nearly exclusively on B lymphocytes, in almost all B-cell developmental stages, and, as a consequence, in the major part of B-cell malignancies. In particular, starting from the anti-human CD19 antibody MOR208 (Patent n°: US 2014/0227277 A1), its sequences of the VH and the VL regions were optimized to produce an anti-human CD19 scFv-Fc from CHO-S cell culture medium. NPs were equipped with this molecule on the surface and characterized, showing a slight increment of the dimension (from $348.7 \pm 4.43 \text{ nm}$ to $388.9 \pm 1.99 \text{ nm}$) and a slender reduction of the negative charge which moves to -13.9 mV , with good stability over time. The presence of the antibody increases the presence of opsonins on the surface of targeted-NPs with respect to untargeted, even if the presence of CS proteins, for example, remains limited to the very first proteins of the cascade, a symptom of its incomplete activation, probably due to dysopsonins intervention, which is more adsorbed on the surface of the NP2. These differences in PC composition were confirmed in functional tests, which demonstrated that there is a slight acceleration in the coagulation process in the presence of NP2 and a consumption of CS proteins that are adsorbed on their surface, still avoiding the mechanical disruption of red blood cells. The binding/internalization test of NPs on primary macrophages, obtained from monocytes

isolated from a healthy donor, evidenced no differences between targeted and untargeted NPs, and showed that the targeting agent bound on the surface of NP2 does not enhance phagocytosis by macrophages. On the contrary, *in vivo* data obtained in the transgenic line of zebrafish Tg(mpeg1:mCherry) demonstrated that NP1 are significantly less engulfed by macrophages than NP2, suggesting that targeted-NPs can be opsonized in this setting, probably for the presence of human anti-CD19 recombinant antibody, and result less concealed to the IS.

The transgenic line of zebrafish Tg(mpeg1:mCherry), initially used to investigate the *in vivo* biodistribution and the engulfment of NPs by macrophages was then used to verify the efficacy of the targeting mechanism in the binding of cancer B-cells. To this end, a new model of human cells distributed in zebrafish larvae has been developed, injecting Nalm-6 cells in the duct of Cuvier. This human/zebrafish model was initially used to study the NPs biodistribution. 2 dpi both untargeted (NP1) and targeted-NPs (NP2) were still in the bloodstream and available to interact with the target while less than 35% of injected NPs were phagocytosed by macrophages. On the other hand, the remaining NPs were co-localized with Nalm-6 cells with a significant difference in favor of targeted NPs with respect to untargeted NPs (14% of NP2 and 4% of NP1, respectively), highlighting the importance of the targeting mechanism also in this *in vivo* setting, to enhance NPs accumulation in tumor cells.

All the data accumulated in our studies demonstrated that targeted HSA-coated PLGA-PVA NPs are safe; the HSA coating is able to modify the PC on the surface of nano-devices, allowing a minor engulfment by macrophages, allowing NPs availability to reach their target for an increased period of time.

Finally, these results encourage us to investigate the last step, filling the NPs developed in this nano platform with a drug and verifying their therapeutic efficacy. Different chemotherapeutic agents were initially tested for their activity against B-cells without taking into consideration their side effects: docetaxel does not have a relevant toxic effect, and idarubicin seems to be more effective but the loading process showed that doxorubicin was better encapsulated than idarubicin in the NPs. For these reasons, doxorubicin-loaded HSA-coated anti-CD19 polymeric NPs (NP5) was produced, characterized *in vitro*, and further studied in the treatment of B-cell malignancies. Loaded- and coated-NPs have similar dimensions and charge to empty

particles and anti-CD19 scFv-Fc maintained its capacity to target tumor B-cells; moreover, the activity of the encapsulated drug remained similar to “free” doxorubicin. As the last step of this project, the therapeutic efficacy of this nano-system was evaluated in the diffused model of B-cell malignancy, comparing the results with the treatment with a “free” drug. Collected data demonstrated that doxorubicin was able to arrest tumor growth in comparison to zebrafish treated with saline. More interestingly, this result was even more evident in zebrafish treated with NP5: at the end of the study, tumor-bearing zebrafish treated with free-drug or NP5 demonstrated a comparable, between treatments, ~30% of survival more than zebrafish treated with the saline, putting the basis for further studies in more complex animal models of B-cell malignancies, such as in mice.

To complete this study remains also to be analyzed the biodistribution and the therapeutic effect of PLGA-PVA-NPs in a more complex animal model, such as mice, and to evaluate the possibility to combine the two approaches, filling PLGA-PVA-NPs with AntagomiR-17 in order to take only the advantages of both. Moreover, all these results together, already highlighted that PLGA-PVA NPs targeted with anti-CD19 antibodies and filled with doxorubicin represent a promising tool for the treatment of B-cell malignancies, but also the result of a platform that can be applied for other pathologies. In fact, PLGA-PVA NPs result biodegradable and therefore safe; moreover, the albumin coating conceals the nano-devices from the IS prolonging NPs' circulating time and the targeting mechanism ensures the reaching of the objective, potentially decreasing off-target effects.

These nanostructures can be seen as a nano-platform in which the single components, such as the payload or the targeting mechanism, can be tailored for the diagnosis or the treatment of pathologies that develop in different patients.

6. Bibliography

1. Siegel, R.L., et al., *Cancer Statistics, 2021*. *CA Cancer J Clin*, 2021. **71(1)**: p. 7-33.
2. Fujita, T.C., et al., *Acute lymphoid leukemia etiopathogenesis*. *Mol Biol Rep*, 2021. **48(1)**: p. 817-822.
3. Ward, Z.J., et al., *Estimating the total incidence of global childhood cancer: a simulation-based analysis*. *Lancet Oncol*, 2019. **20(4)**: p. 483-493.
4. Steliarova-Foucher, E., et al., *International incidence of childhood cancer, 2001-10: a population-based registry study*. *Lancet Oncol*, 2017. **18(6)**: p. 719-731.
5. Wei, Y., et al., *B cell heterogeneity, plasticity, and functional diversity in cancer microenvironments*. *Oncogene*, 2021. **40(29)**: p. 4737-4745.
6. Cooper, M.D. and M.N. Alder, *The evolution of adaptive immune systems*. *Cell*, 2006. **124(4)**: p. 815-22.
7. Raff, M.C., *T and B lymphocytes and immune responses*. *Nature*, 1973. **242(5392)**: p. 19-23.
8. LeBien, T.W. and T.F. Tedder, *B lymphocytes: how they develop and function*. *Blood*, 2008. **112(5)**: p. 1570-80.
9. Schroeder, H.W., A. Radbruch, and C. Berek, *B-Cell Development and Differentiation, in Clinical Immunology*. 2019. p. 107-118.e1.
10. Crickx, E., et al., *Anti-CD20-mediated B-cell depletion in autoimmune diseases: successes, failures and future perspectives*. *Kidney Int*, 2020. **97(5)**: p. 885-893.
11. Noonan, K., *Introduction to B-Cell disorders*. *Clin J Oncol Nurs*, 2007. **11(1 Suppl)**: p. 3-12.
12. Jackson, T.R., R.E. Ling, and A. Roy, *The Origin of B-cells: Human Fetal B Cell Development and Implications for the Pathogenesis of Childhood Acute Lymphoblastic Leukemia*. *Front Immunol*, 2021. **12**: p. 637975.
13. Kupperts, R., *Mechanisms of B-cell lymphoma pathogenesis*. *Nat Rev Cancer*, 2005. **5(4)**: p. 251-62.
14. Shankland, K.R., J.O. Armitage, and B.W. Hancock, *Non-Hodgkin lymphoma*. *The Lancet*, 2012. **380(9844)**: p. 848-857.
15. Rickert, R.C., *New insights into pre-BCR and BCR signalling with relevance to B cell malignancies*. *Nat Rev Immunol*, 2013. **13(8)**: p. 578-91.
16. Muschen, M., *Autoimmunity checkpoints as therapeutic targets in B cell malignancies*. *Nat Rev Cancer*, 2018. **18(2)**: p. 103-116.

17. Shaffer, A.L., A. Rosenwald, and L.M. Staudt, *Lymphoid malignancies: the dark side of B-cell differentiation*. *Nat Rev Immunol*, 2002. **2**(12): p. 920-32.
18. Wu, H., et al., *Epigenetic regulation in B-cell maturation and its dysregulation in autoimmunity*. *Cell Mol Immunol*, 2018. **15**(7): p. 676-684.
19. McEachron, T.A. and L.J. Helman, *Recent Advances in Pediatric Cancer Research*. *Cancer Res*, 2021. **81**(23): p. 5783-5799.
20. Davies, K., et al., *Pediatric Aggressive Mature B-Cell Lymphomas, Version 2.2020, NCCN Clinical Practice Guidelines in Oncology*. *J Natl Compr Canc Netw*, 2020. **18**(8): p. 1105-1123.
21. Chang, J.H., et al., *Acute lymphoblastic leukemia*. *Pediatr Blood Cancer*, 2021. **68 Suppl 2**: p. e28371.
22. Lee, J.B., et al., *State-of-Art of Cellular Therapy for Acute Leukemia*. *Int J Mol Sci*, 2021. **22**(9).
23. de-The, G., *The Epstein-Barr virus (EBV): a Rosetta Stone for understanding the role of viruses in immunopathological disorders and in human carcinogenesis*. *Biomed Pharmacother*, 1985. **39**(2): p. 49-51.
24. Atallah-Yunes, S.A., D.J. Murphy, and A. Noy, *HIV-associated Burkitt lymphoma*. *The Lancet Haematology*, 2020. **7**(8): p. e594-e600.
25. Molyneux, E.M., et al., *Burkitt's lymphoma*. *The Lancet*, 2012. **379**(9822): p. 1234-1244.
26. Casulo, C. and J.W. Friedberg, *Burkitt lymphoma- a rare but challenging lymphoma*. *Best Pract Res Clin Haematol*, 2018. **31**(3): p. 279-284.
27. Klein, G., *Burkitt lymphoma--a stalking horse for cancer research?* *Semin Cancer Biol*, 2009. **19**(6): p. 347-50.
28. Inaba, H. and C.G. Mullighan, *Pediatric acute lymphoblastic leukemia*. *Haematologica*, 2020. **105**(11): p. 2524-2539.
29. Vale, A.M. and H.W. Schroeder, Jr., *Clinical consequences of defects in B-cell development*. *J Allergy Clin Immunol*, 2010. **125**(4): p. 778-87.
30. Herrera, A.F. and A. Molina, *Investigational Antibody-Drug Conjugates for Treatment of B-lineage Malignancies*. *Clin Lymphoma Myeloma Leuk*, 2018. **18**(7): p. 452-468 e4.
31. Inthagard, J., J. Edwards, and A.K. Roseweir, *Immunotherapy: enhancing the efficacy of this promising therapeutic in multiple cancers*. *Clin Sci (Lond)*, 2019. **133**(2): p. 181-193.

32. Yi, J.H., *Novel combination immunochemotherapy beyond CD20 for B-cell lymphomas*. *Blood Res*, 2021. **56**(S1): p. S1-S4.
33. Panuciak, K., et al., *Insights into Modern Therapeutic Approaches in Pediatric Acute Leukemias*. *Cells*, 2022. **11**(1).
34. Pablo, T.T.F.E., *CD20: a regulator of cell-cycle progression of Blymphocyte,s*. *Immunology Today*, 1994. **15**.
35. Krackhardt, A.M., et al., *Identification of tumor-associated antigens in chronic lymphocytic leukemia by SEREX*. *Blood*, 2002. **100**(6): p. 2123-31.
36. Muggen, A.F., et al., *Basal Ca(2+) signaling is particularly increased in mutated chronic lymphocytic leukemia*. *Leukemia*, 2015. **29**(2): p. 321-8.
37. Jeong, K., et al., *Development of highly efficient nanocarrier-mediated delivery approaches for cancer therapy*. *Cancer Lett*, 2016. **374**(1): p. 31-43.
38. Raufi, A., A.S. Ebrahim, and A. Al-Katib, *Targeting CD19 in B-cell lymphoma: emerging role of SAR3419*. *Cancer Manag Res*, 2013. **5**: p. 225-33.
39. Li, X., et al., *CD19, from bench to bedside*. *Immunol Lett*, 2017. **183**: p. 86-95.
40. Viardot, A. and E. Sala, *Investigational immunotherapy targeting CD19 for the treatment of acute lymphoblastic leukemia*. *Expert Opin Investig Drugs*, 2021. **30**(7): p. 773-784.
41. Watkins, M.P. and N.L. Bartlett, *CD19-targeted immunotherapies for treatment of patients with non-Hodgkin B-cell lymphomas*. *Expert Opin Investig Drugs*, 2018. **27**(7): p. 601-611.
42. Sadelain, M., R. Brentjens, and I. Riviere, *The basic principles of chimeric antigen receptor design*. *Cancer Discov*, 2013. **3**(4): p. 388-98.
43. Klein, C., et al., *Epitope interactions of monoclonal antibodies targeting CD20 and their relationship to functional properties*. *MAbs*, 2013. **5**(1): p. 22-33.
44. Capolla, S., et al., *A new approach for the treatment of CLL using chlorambucil/hydroxychloroquine-loaded anti-CD20 nanoparticles*. *Nano Research*, 2015. **9**(2): p. 537-548.
45. Abdelbaky, S.B., et al., *Cancer immunotherapy from biology to nanomedicine*. *J Control Release*, 2021. **336**: p. 410-432.
46. Gonzalez-Valdivieso, J., et al., *Advanced nanomedicine and cancer: Challenges and opportunities in clinical translation*. *Int J Pharm*, 2021. **599**: p. 120438.
47. Damasco, J.A., et al., *Understanding Nanoparticle Toxicity to Direct a Safe-by-Design Approach in Cancer Nanomedicine*. *Nanomaterials (Basel)*, 2020. **10**(11).

48. Bleeker, E.A., et al., *Considerations on the EU definition of a nanomaterial: science to support policy making*. Regul Toxicol Pharmacol, 2013. **65**(1): p. 119-25.
49. M., W.G., *The 'right' size in nanobiotechnology*. Nature Biotechnology, 2003. **21**.
50. Pene, F., et al., *Toward theragnostics*. Crit Care Med, 2009. **37**(1 Suppl): p. S50-8.
51. Rizzo, L.Y., et al., *Recent progress in nanomedicine: therapeutic, diagnostic and theranostic applications*. Curr Opin Biotechnol, 2013. **24**(6): p. 1159-66.
52. Robert, F.O.C.L., *Impact of Nanotechnology on Drug Delivery*. ACS nano, 2009. **3**.
53. Hicks, S.W., et al., *The novel CD19-targeting antibody-drug conjugate huB4-DGN462 shows improved anti-tumor activity compared to SAR3419 in CD19-positive lymphoma and leukemia models*. Haematologica, 2019. **104**(8): p. 1633-1639.
54. Ferrari, M., *Nanovector therapeutics*. Curr Opin Chem Biol, 2005. **9**(4): p. 343-6.
55. Kagan, V.E., H. Bayir, and A.A. Shvedova, *Nanomedicine and nanotoxicology: two sides of the same coin*. Nanomedicine, 2005. **1**(4): p. 313-6.
56. Shi, J., et al., *Cancer nanomedicine: progress, challenges and opportunities*. Nat Rev Cancer, 2017. **17**(1): p. 20-37.
57. Chen, H., et al., *Rethinking cancer nanotheranostics*. Nat Rev Mater, 2017. **2**.
58. Duncan, R. and R. Gaspar, *Nanomedicine(s) under the microscope*. Mol Pharm, 2011. **8**(6): p. 2101-41.
59. Xiao, Q., et al., *Biological drug and drug delivery-mediated immunotherapy*. Acta Pharm Sin B, 2021. **11**(4): p. 941-960.
60. Robert, P.D.K.M.H.S.F.O.C.M.R.L., *Nanocarriers as an emerging platform for cancer therapy*. Nature Nanotechnology, 2007. **2**.
61. von Roemeling, C., et al., *Breaking Down the Barriers to Precision Cancer Nanomedicine*. Trends Biotechnol, 2017. **35**(2): p. 159-171.
62. Thi, T.T.H., et al., *Lipid-Based Nanoparticles in the Clinic and Clinical Trials: From Cancer Nanomedicine to COVID-19 Vaccines*. Vaccines (Basel), 2021. **9**(4).
63. Gregoriadis, G., *Drug entrapment in liposomes*. FEBS Letters, 1973. **36**(3): p. 292-296.
64. Kim, E.M. and H.J. Jeong, *Liposomes: Biomedical Applications*. Chonnam Med J, 2021. **57**(1): p. 27-35.
65. Sanna, V., N. Pala, and M. Sechi, *Targeted therapy using nanotechnology: focus on cancer*. Int J Nanomedicine, 2014. **9**: p. 467-83.
66. Gregoriadis, G., *Drug entrapment in liposomes*. FEBS Lett, 1973. **36**(3): p. 292-6.

67. Eloy, J.O., et al., *Liposomes as carriers of hydrophilic small molecule drugs: strategies to enhance encapsulation and delivery*. *Colloids Surf B Biointerfaces*, 2014. **123**: p. 345-63.
68. Maximilien, J., et al., *Nanoparticles in Biomedical Applications*, in *Measuring Biological Impacts of Nanomaterials*. 2015. p. 177-210.
69. Ma, P. and R.J. Mumper, *Anthracycline Nano-Delivery Systems to Overcome Multiple Drug Resistance: A Comprehensive Review*. *Nano Today*, 2013. **8**(3): p. 313-331.
70. Ahmed, S.E., A.M. Martins, and G.A. Hussein, *The use of ultrasound to release chemotherapeutic drugs from micelles and liposomes*. *J Drug Target*, 2015. **23**(1): p. 16-42.
71. Peer, D., et al., *Nanocarriers as an emerging platform for cancer therapy*. *Nat Nanotechnol*, 2007. **2**(12): p. 751-60.
72. Kim, B.Y., J.T. Rutka, and W.C. Chan, *Nanomedicine*. *N Engl J Med*, 2010. **363**(25): p. 2434-43.
73. Bobo, D., et al., *Nanoparticle-Based Medicines: A Review of FDA-Approved Materials and Clinical Trials to Date*. *Pharm Res*, 2016. **33**(10): p. 2373-87.
74. Crecente-Campo, J., et al., *The size and composition of polymeric nanocapsules dictate their interaction with macrophages and biodistribution in zebrafish*. *J Control Release*, 2019. **308**: p. 98-108.
75. Bolhassani, A., et al., *Polymeric nanoparticles: potent vectors for vaccine delivery targeting cancer and infectious diseases*. *Hum Vaccin Immunother*, 2014. **10**(2): p. 321-32.
76. Banik, B.L., P. Fattahi, and J.L. Brown, *Polymeric nanoparticles: the future of nanomedicine*. *Wiley Interdiscip Rev Nanomed Nanobiotechnol*, 2016. **8**(2): p. 271-99.
77. Kamaly, N., et al., *Degradable Controlled-Release Polymers and Polymeric Nanoparticles: Mechanisms of Controlling Drug Release*. *Chem Rev*, 2016. **116**(4): p. 2602-63.
78. Mansoor, S., et al., *Polymer-Based Nanoparticle Strategies for Insulin Delivery*. *Polymers (Basel)*, 2019. **11**(9).
79. Sinha, R., et al., *Nanotechnology in cancer therapeutics: bioconjugated nanoparticles for drug delivery*. *Mol Cancer Ther*, 2006. **5**(8): p. 1909-17.

80. Gao, Y. and Y. Wu, *Recent advances of chitosan-based nanoparticles for biomedical and biotechnological applications*. *Int J Biol Macromol*, 2022. **203**: p. 379-388.
81. Cavalli, R., A. Bisazza, and D. Lembo, *Micro- and nanobubbles: a versatile non-viral platform for gene delivery*. *Int J Pharm*, 2013. **456**(2): p. 437-45.
82. Ali, A. and S. Ahmed, *A review on chitosan and its nanocomposites in drug delivery*. *Int J Biol Macromol*, 2018. **109**: p. 273-286.
83. Riehemann, K., et al., *Nanomedicine--challenge and perspectives*. *Angew Chem Int Ed Engl*, 2009. **48**(5): p. 872-97.
84. Sharma, A.K., L. Gupta, and U. Gupta, *Nanoparticles as nucleic acid delivery vectors*, in *Advances in Nanomedicine for the Delivery of Therapeutic Nucleic Acids*. 2017. p. 13-42.
85. Danhier, F., *To exploit the tumor microenvironment: Since the EPR effect fails in the clinic, what is the future of nanomedicine?* *J Control Release*, 2016. **244**(Pt A): p. 108-121.
86. Sadat Tabatabaei Mirakabad, F., et al., *PLGA-based nanoparticles as cancer drug delivery systems*. *Asian Pac J Cancer Prev*, 2014. **15**(2): p. 517-35.
87. Ben Halima, N., *Poly(vinyl alcohol): review of its promising applications and insights into biodegradation*. *RSC Advances*, 2016. **6**(46): p. 39823-39832.
88. Sahoo, S.K., et al., *Residual polyvinyl alcohol associated with poly (d,l-lactide-co-glycolide) nanoparticles affects their physical properties and cellular uptake*. *Journal of Controlled Release*, 2002. **82**(1): p. 105-114.
89. Guengerich, F.P., *Mechanisms of drug toxicity and relevance to pharmaceutical development*. *Drug Metab Pharmacokinet*, 2011. **26**(1): p. 3-14.
90. Houshmand, M., et al., *Nanocarriers as Magic Bullets in the Treatment of Leukemia*. *Nanomaterials (Basel)*, 2020. **10**(2).
91. Tran, S., et al., *Cancer nanomedicine: a review of recent success in drug delivery*. *Clin Transl Med*, 2017. **6**(1): p. 44.
92. Wang, T., et al., *Successful Treatment of Pediatric Refractory Burkitt Lymphoma PTLN after Liver Transplantation using Anti-CD19 Chimeric Antigen Receptor T-Cell Therapy*. *Cell Transplant*, 2021. **30**: p. 963689721996649.
93. Lorenzer, C., et al., *Going beyond the liver: progress and challenges of targeted delivery of siRNA therapeutics*. *J Control Release*, 2015. **203**: p. 1-15.

94. Baboci, L., et al., *The Dual Role of the Liver in Nanomedicine as an Actor in the Elimination of Nanostructures or a Therapeutic Target*. J Oncol, 2020. **2020**: p. 4638192.
95. Dawidczyk, C.M., et al., *State-of-the-art in design rules for drug delivery platforms: lessons learned from FDA-approved nanomedicines*. J Control Release, 2014. **187**: p. 133-44.
96. Wang, R., et al., *Strategies for the design of nanoparticles: starting with long-circulating nanoparticles, from lab to clinic*. Biomater Sci, 2021. **9**(10): p. 3621-3637.
97. Nie, S., *Understanding and overcoming major barriers in cancer nanomedicine*. Nanomedicine (Lond), 2010. **5**(4): p. 523-8.
98. Jokerst, J.V., et al., *Nanoparticle PEGylation for imaging and therapy*. Nanomedicine (Lond), 2011. **6**(4): p. 715-28.
99. Behzadi, S., et al., *Cellular uptake of nanoparticles: journey inside the cell*. Chem Soc Rev, 2017. **46**(14): p. 4218-4244.
100. Treuel, L. and G.U. Nienhaus, *Toward a molecular understanding of nanoparticle-protein interactions*. Biophys Rev, 2012. **4**(2): p. 137-147.
101. Zeng, L., et al., *Role of protein corona in the biological effect of nanomaterials: Investigating methods*. TrAC Trends in Analytical Chemistry, 2019. **118**: p. 303-314.
102. Nguyen, V.H. and B.J. Lee, *Protein corona: a new approach for nanomedicine design*. Int J Nanomedicine, 2017. **12**: p. 3137-3151.
103. Pederzoli F., G.M., Forni F., Vandelli M.A., Belletti D., Tosi G., Ruozi B., *How does "Protein Corona" Affect the In vivo Efficiency of Polymeric Nanoparticles? State of Art*. Frontiers in Nanomedicine, 2017. **2**: p. 199-238.
104. Berrecoso, G., J. Crecente-Campo, and M.J. Alonso, *Unveiling the pitfalls of the protein corona of polymeric drug nanocarriers*. Drug Deliv Transl Res, 2020. **10**(3): p. 730-750.
105. Li, Y. and J.S. Lee, *Insights into Characterization Methods and Biomedical Applications of Nanoparticle-Protein Corona*. Materials (Basel), 2020. **13**(14).
106. Lomis, N., et al., *Human Serum Albumin Nanoparticles for Use in Cancer Drug Delivery: Process Optimization and In Vitro Characterization*. Nanomaterials (Basel), 2016. **6**(6).
107. An, F.F. and X.H. Zhang, *Strategies for Preparing Albumin-based Nanoparticles for Multifunctional Bioimaging and Drug Delivery*. Theranostics, 2017. **7**(15): p. 3667-3689.

108. Hyun, H., et al., *Surface modification of polymer nanoparticles with native albumin for enhancing drug delivery to solid tumors*. *Biomaterials*, 2018. **180**: p. 206-224.
109. Wicki, A., et al., *Nanomedicine in cancer therapy: challenges, opportunities, and clinical applications*. *J Control Release*, 2015. **200**: p. 138-57.
110. Maeda, H., H. Nakamura, and J. Fang, *The EPR effect for macromolecular drug delivery to solid tumors: Improvement of tumor uptake, lowering of systemic toxicity, and distinct tumor imaging in vivo*. *Adv Drug Deliv Rev*, 2013. **65**(1): p. 71-9.
111. Bertrand, N., et al., *Cancer nanotechnology: the impact of passive and active targeting in the era of modern cancer biology*. *Adv Drug Deliv Rev*, 2014. **66**: p. 2-25.
112. Aghebati-Maleki, A., et al., *Nanoparticles and cancer therapy: Perspectives for application of nanoparticles in the treatment of cancers*. *J Cell Physiol*, 2020. **235**(3): p. 1962-1972.
113. Au, J.L., et al., *Determinants of drug delivery and transport to solid tumors*. *J Control Release*, 2001. **74**(1-3): p. 31-46.
114. Zhang, B., Y. Hu, and Z. Pang, *Modulating the Tumor Microenvironment to Enhance Tumor Nanomedicine Delivery*. *Front Pharmacol*, 2017. **8**: p. 952.
115. Steichen, S.D., M. Caldorera-Moore, and N.A. Peppas, *A review of current nanoparticle and targeting moieties for the delivery of cancer therapeutics*. *Eur J Pharm Sci*, 2013. **48**(3): p. 416-27.
116. Wilhelm Stefan, T.A.J., Dai Qin, Ohta Seiichi, Audet Julie, Dvorak Harold F., Chan Warren C. W., *Analysis of nanoparticle delivery to tumours*. *Nature Reviews Materials*, 2016. **1**.
117. Dai, W., et al., *Combination antitumor therapy with targeted dual-nanomedicines*. *Adv Drug Deliv Rev*, 2017. **115**: p. 23-45.
118. Blanco, E., H. Shen, and M. Ferrari, *Principles of nanoparticle design for overcoming biological barriers to drug delivery*. *Nat Biotechnol*, 2015. **33**(9): p. 941-51.
119. Docter, D., et al., *Quantitative profiling of the protein coronas that form around nanoparticles*. *Nat Protoc*, 2014. **9**(9): p. 2030-44.
120. Fleischer, C.C. and C.K. Payne, *Secondary structure of corona proteins determines the cell surface receptors used by nanoparticles*. *J Phys Chem B*, 2014. **118**(49): p. 14017-26.

121. Cuenca, M. and V. Peperzak, *Advances and Perspectives in the Treatment of B-Cell Malignancies*. *Cancers (Basel)*, 2021. **13**(9).
122. Hosseinkhani, N., et al., *Immune Checkpoints and CAR-T Cells: The Pioneers in Future Cancer Therapies?* *Int J Mol Sci*, 2020. **21**(21).
123. van der Horst, H.J., et al., *Fc-Engineered Antibodies with Enhanced Fc-Effector Function for the Treatment of B-Cell Malignancies*. *Cancers (Basel)*, 2020. **12**(10).
124. Sterner, R.C. and R.M. Sterner, *CAR-T cell therapy: current limitations and potential strategies*. *Blood Cancer J*, 2021. **11**(4): p. 69.
125. Vozella, F., et al., *Monoclonal antibodies in multiple myeloma*. *Panminerva Med*, 2021. **63**(1): p. 21-27.
126. Fang, L.L., et al., *Expression, regulation and mechanism of action of the miR-17-92 cluster in tumor cells (Review)*. *Int J Mol Med*, 2017. **40**(6): p. 1624-1630.
127. Florean, C., et al., *Epigenomics of leukemia: from mechanisms to therapeutic applications*. *Epigenomics*, 2011. **3**(5): p. 581-609.
128. Zanette, D.L., et al., *miRNA expression profiles in chronic lymphocytic and acute lymphocytic leukemia*. *Braz J Med Biol Res*, 2007. **40**(11): p. 1435-40.
129. Zhou, X.X. and X. Wang, *Role of microRNAs in chronic lymphocytic leukemia (Review)*. *Mol Med Rep*, 2013. **8**(3): p. 719-25.
130. He, L., et al., *A microRNA polycistron as a potential human oncogene*. *Nature*, 2005. **435**(7043): p. 828-33.
131. Olive, V., I. Jiang, and L. He, *mir-17-92, a cluster of miRNAs in the midst of the cancer network*. *Int J Biochem Cell Biol*, 2010. **42**(8): p. 1348-54.
132. Feng, S., et al., *Combinations of elevated tissue miRNA-17-92 cluster expression and serum prostate-specific antigen as potential diagnostic biomarkers for prostate cancer*. *Oncol Lett*, 2017. **14**(6): p. 6943-6949.
133. Sengupta, D., V. Govindaraj, and S. Kar, *Alteration in microRNA-17-92 dynamics accounts for differential nature of cellular proliferation*. *FEBS Lett*, 2018. **592**(3): p. 446-458.
134. Yang, J., et al., *Decreased miR-17-92 cluster expression level in serum and granulocytes preceding onset of antithyroid drug-induced agranulocytosis*. *Endocrine*, 2018. **59**(1): p. 218-225.
135. Liu, X.S., et al., *MicroRNA-17-92 cluster mediates the proliferation and survival of neural progenitor cells after stroke*. *J Biol Chem*, 2013. **288**(18): p. 12478-88.

136. Tagawa, H., S. Ikeda, and K. Sawada, *Role of microRNA in the pathogenesis of malignant lymphoma*. *Cancer Sci*, 2013. **104**(7): p. 801-9.
137. Michele Dal Bo, R.B., Luis Hernández, Valter Gattei, *The MYC/miR-17-92 axis in lymphoproliferative disorders: A common pathway with therapeutic potential*. *Oncotarget*, 2015. **6**.
138. Shaffer, A.L., 3rd, R.M. Young, and L.M. Staudt, *Pathogenesis of human B cell lymphomas*. *Annu Rev Immunol*, 2012. **30**: p. 565-610.
139. Su, J., et al., *Silencing microRNA by interfering nanoparticles in mice*. *Nucleic Acids Res*, 2011. **39**(6): p. e38.
140. Iorio, M.V. and C.M. Croce, *MicroRNA dysregulation in cancer: diagnostics, monitoring and therapeutics. A comprehensive review*. *EMBO Mol Med*, 2012. **4**(3): p. 143-59.
141. Balatti, V., et al., *Novel mechanisms of regulation of miRNAs in CLL*. *Trends Cancer*, 2016. **2**(3): p. 134-143.
142. Krutzfeldt, J., et al., *Silencing of microRNAs in vivo with 'antagomirs'*. *Nature*, 2005. **438**(7068): p. 685-9.
143. Bhagat, A. and E.S. Kleinerman, *Anthracycline-Induced Cardiotoxicity: Causes, Mechanisms, and Prevention*. *Adv Exp Med Biol*, 2020. **1257**: p. 181-192.
144. Cardinale, D., F. Iacopo, and C.M. Cipolla, *Cardiotoxicity of Anthracyclines*. *Front Cardiovasc Med*, 2020. **7**: p. 26.
145. Narezkina, A., H.K. Narayan, and A.E. Zemljic-Harpf, *Molecular mechanisms of anthracycline cardiovascular toxicity*. *Clin Sci (Lond)*, 2021. **135**(10): p. 1311-1332.
146. McGowan, J.V., et al., *Anthracycline Chemotherapy and Cardiotoxicity*. *Cardiovasc Drugs Ther*, 2017. **31**(1): p. 63-75.
147. Tripaydonis, A., R. Conyers, and D.A. Elliott, *Pediatric Anthracycline-Induced Cardiotoxicity: Mechanisms, Pharmacogenomics, and Pluripotent Stem-Cell Modeling*. *Clin Pharmacol Ther*, 2019. **105**(3): p. 614-624.
148. Martins-Teixeira, M.B. and I. Carvalho, *Antitumour Anthracyclines: Progress and Perspectives*. *ChemMedChem*, 2020. **15**(11): p. 933-948.
149. Vasir, J.K. and V. Labhasetwar, *Preparation of biodegradable nanoparticles and their use in transfection*. *CSH Protoc*, 2008. **2008**: p. pdb prot4888.
150. Atallah-Yunes, S.A., D.J. Murphy, and A. Noy, *HIV-associated Burkitt lymphoma*. *Lancet Haematol*, 2020. **7**(8): p. e594-e600.

151. Dereani, S., et al., *Potential therapeutic role of antagomiR17 for the treatment of chronic lymphocytic leukemia*. J Hematol Oncol, 2014. **7**: p. 79.
152. Vauthier, C., *A journey through the emergence of nanomedicines with poly(alkylcyanoacrylate) based nanoparticles*. J Drug Target, 2019. **27**(5-6): p. 502-524.
153. Alheshibri, M. and V.S.J. Craig, *Differentiating between Nanoparticles and Nanobubbles by Evaluation of the Compressibility and Density of Nanoparticles*. The Journal of Physical Chemistry C, 2018. **122**(38): p. 21998-22007.
154. Crimeen-Irwin, B., et al., *Failure of immune homeostasis -- the consequences of under and over reactivity*. Curr Drug Targets Immune Endocr Metabol Disord, 2005. **5**(4): p. 413-22.
155. Cruz, G.G.D.L., et al., *Interaction of Nanoparticles with Blood Components and Associated Pathophysiological Effects, in Unraveling the Safety Profile of Nanoscale Particles and Materials - From Biomedical to Environmental Applications*. 2018.
156. Talaei, F., et al., *Core shell methyl methacrylate chitosan nanoparticles: In vitro mucoadhesion and complement activation*. Daru, 2011. **19**(4): p. 257-65.
157. Oppermann, M. and R. Wurzner, *Modern determination of complement activation*. Semin Thromb Hemost, 2010. **36**(6): p. 611-9.
158. Mezzaroba, N., et al., *New potential therapeutic approach for the treatment of B-Cell malignancies using chlorambucil/hydroxychloroquine-loaded anti-CD20 nanoparticles*. PLoS One, 2013. **8**(9): p. e74216.
159. Tedder, T.F. and P. Engel, *CD20: a regulator of cell-cycle progression of B lymphocytes*. Immunology Today, 1994. **15**(9): p. 450-454.
160. Miner, J.H., *The glomerular basement membrane*. Exp Cell Res, 2012. **318**(9): p. 973-8.
161. Terwilliger, T. and M. Abdul-Hay, *Acute lymphoblastic leukemia: a comprehensive review and 2017 update*. Blood Cancer J, 2017. **7**(6): p. e577.
162. Saha, K., et al., *Regulation of Macrophage Recognition through the Interplay of Nanoparticle Surface Functionality and Protein Corona*. ACS Nano, 2016. **10**(4): p. 4421-30.
163. Boraschi, D., et al., *Nanoparticles and innate immunity: new perspectives on host defence*. Semin Immunol, 2017. **34**: p. 33-51.

164. Papini, E., R. Tavano, and F. Mancin, *Opsonins and Dysopsonins of Nanoparticles: Facts, Concepts, and Methodological Guidelines*. Front Immunol, 2020. **11**: p. 567365.
165. Merlot, A.M., D.S. Kalinowski, and D.R. Richardson, *Unraveling the mysteries of serum albumin-more than just a serum protein*. Front Physiol, 2014. **5**: p. 299.
166. Bern, M., et al., *The role of albumin receptors in regulation of albumin homeostasis: Implications for drug delivery*. J Control Release, 2015. **211**: p. 144-62.
167. Ellett, F., et al., *mpeg1 promoter transgenes direct macrophage-lineage expression in zebrafish*. Blood, 2011. **117**(4): p. e49-56.
168. Lee, L.M., et al., *The fate of human malignant melanoma cells transplanted into zebrafish embryos: assessment of migration and cell division in the absence of tumor formation*. Dev Dyn, 2005. **233**(4): p. 1560-70.
169. Hill, D., et al., *Embryonic zebrafish xenograft assay of human cancer metastasis*. F1000Res, 2018. **7**: p. 1682.
170. Bozzer, S., et al., *Nanoparticles-Based Oligonucleotides Delivery in Cancer: Role of Zebrafish as Animal Model*. Pharmaceutics, 2021. **13**(8).
171. Karlsson, J., J. von Hofsten, and P.E. Olsson, *Generating transparent zebrafish: a refined method to improve detection of gene expression during embryonic development*. Mar Biotechnol (NY), 2001. **3**(6): p. 522-7.
172. Warga, R.M., D.A. Kane, and R.K. Ho, *Fate mapping embryonic blood in zebrafish: multi- and unipotential lineages are segregated at gastrulation*. Dev Cell, 2009. **16**(5): p. 744-55.
173. Francis, G.L., *Albumin and mammalian cell culture: implications for biotechnology applications*. Cytotechnology, 2010. **62**(1): p. 1-16.
174. Mishra, V. and R.J. Heath, *Structural and Biochemical Features of Human Serum Albumin Essential for Eukaryotic Cell Culture*. Int J Mol Sci, 2021. **22**(16).
175. Platel, D., et al., *Comparative cardiotoxicity of idarubicin and doxorubicin using the isolated perfused rat heart model*. Anticancer Drugs, 1999. **10**(7): p. 671-6.

